國 立 中 央 大 學

大 氣 科 學 學 系

碩 士 論 文

使用局地系集轉換卡爾曼濾波器同化雙偏極化參數的全新方法：夏季真實個案中的分析場與預報場

A Novel Approach to Assimilate Polarimetric Parameters with an LETKF System: Analysis and Forecast in Real Summer Cases

研 究 生：莊秉學

指導教授：鍾高陞 博士

中 華 民 國 一一零 年 六 月

國立中央大學圖書館學位論文授權書

填單日期：2021 / 7 / 26　　　　2019.9 版

授權人姓名	莊秉學	學 號	108621007
系所名稱	大氣科學學系大氣物理碩士班	學位類別	■碩士　□博士
論文名稱	A Novel Approach to Assimilate Polarimetric Parameters with an LETKF System: Analysis and Forecast in Real Summer Cases	指導教授	鍾高陞

學位論文網路公開授權

授權本人撰寫之學位論文全文電子檔：

・在「**國立中央大學圖書館博碩士論文系統**」.

(√)同意立即網路公開

( )同意 於西元______年______月______日網路公開

( )不同意網路公開，原因是：________________________

・在國家圖書館「**臺灣博碩士論文知識加值系統**」

(√)同意立即網路公開

( )同意 於西元______年______月______日網路公開

( )不同意網路公開，原因是：________________________

依著作權法規定，非專屬、無償授權國立中央大學、台灣聯合大學系統與國家圖書館，不限地域、時間與次數，以文件、錄影帶、錄音帶、光碟、微縮、數位化或其他方式將上列授權標的基於非營利目的進行重製。

學位論文紙本延後公開申請 (紙本學位論文立即公開者此欄免填)

本人撰寫之學位論文紙本因以下原因將延後公開

・**延後原因**

( )已申請專利並檢附證明，專利申請案號：

( )準備以上列論文投稿期刊

( )涉國家機密

( )依法不得提供，請說明：________________

・**公開日期**：西元________年________月________日

※繳交教務處註冊組之紙本論文(送繳國家圖書館)若不立即公開，請加填「國家圖書館學位論文延後公開申請書」

研究生簽名：莊秉學　　　　指導教授簽名：鍾高陞

*本授權書請完整填寫並親筆簽名後，裝訂於論文封面之次頁。

國立中央大學碩士班研究生
論 文 指 導 教 授 推 薦 書

大氣科學學系大氣物理碩士班 學系/研究所 莊秉學 研究生

所提之論文 A Novel Approach to Assimilate Polarimetric Parameters with an LETKF System: Analysis and Forecast in Real Summer Cases

係由本人指導撰述，同意提付審查。

指導教授 鍾高陞 (簽章)

110 年 6 月 24 日

1100622

國立中央大學碩士班研究生

論 文 口 試 委 員 審 定 書

大氣科學學系大氣物理碩士班 學系/研究所 莊秉學 研究生

所提之論文 A Novel Approach to Assimilate Polarimetric Parameters with an LETKF System: Analysis and Forecast in Real Summer Cases

經由委員會審議，認定符合碩士資格標準。

學位考試委員會召集人 ______________________

委　　　　員 ______________________

____

____

____

中 華 民 國 110 年 7 月 6 日

1100629

國立中央大學碩士班研究生
論文口試委員審定書

大氣科學學系大氣物理碩士班 學系/研究所 莊秉學 研究生

所提之論文 A Novel Approach to Assimilate Polarimetric Parameters with an LETKF System: Analysis and Forecast in Real Summer Cases

經由委員會審議，認定符合碩士資格標準。

學位考試委員會召集人 ______________________

委　　　　　員 蔡直謙

中　華　民　國　110　年　7　月　6　日

1100629

國立中央大學碩士班研究生
論 文 口 試 委 員 審 定 書

大氣科學學系大氣物理碩士班 學系/研究所 莊秉學 研究生

所提之論文 A Novel Approach to Assimilate Polarimetric Parameters with an LETKF System: Analysis and Forecast in Real Summer Cases

經由委員會審議，認定符合碩士資格標準。

學位考試委員會召集人 ______________________

委　　　　員 ______________________

鍾高陞

楊舒芝

張偉裕

中　華　民　國　110 年 7 月 6 日

1100629

摘要

本研究使用 WRF-LETKF 雷達同化系統(WRF-LETKF Radar Assimilation System, WLRAS)進行資料同化實驗，除了同化已被廣泛使用在雷達資料同化的徑向風(V_r)與回波(Z_H)，進一步同化雙偏極化參數，如差異反射率(Z_{DR})與比差異相位差(K_{DP})。另外，本研究設計了一種新的同化方法，利用平均粒徑與 Z_{DR} 的高相關性從 Z_{DR} 的觀測增量取得更多微物理變數的修正，當觀測資料被同化時更新由混合比以及總數量濃度診斷得到的標準化截距參數(N_w)以及質量權重平均粒徑(D_m)。同化實驗選用了兩種不同的中尺度系統以及四種不同的雲微物理參數化方案。其中一個系統是由西南風驅使的颮線系統，另外一個系統是局地產生的午後對流。四種不同的雲微物理參數化方案分別為 GCE、WSM6、WDM6、MOR。本研究執行了一系列的實驗以評估同化雙偏極化參數對於分析場以及定量降水預報(Quantitative Precipitation Forecast, QPF)的影響。實驗結果顯示利用單矩量的雲微物理參數化方案同化額外的 Z_{DR} 後，Z_H 與 K_{DP} 的分析場反而會變得比較差。當使用雙矩量的雲微物理參數化方案同化 Z_{DR} 與 K_{DP} 時，兩者的誤差都能夠下降。此外，使用新方法同化雙偏極化參數可以明顯的改善 Z_{DR} 的分析場，使 Z_{DR} 的誤差下降更多。除了對雲微物理變數的修正之外，同化額外的雙偏極化參數亦能夠調整水氣分布以及加強對流區的垂直運動。在同化了雙偏極化參數之後，強降雨的表現有得到改善，即使在利用單矩量雲微物理參數化方案同化 Z_{DR} 的實驗中也可以發現強降雨的機率變高。總結來說，利用單矩量雲微物理參數化方案同化額外雙偏極化參數存在著限制，而雙矩量雲微物理參數化方案有更多的彈性來調適雙偏極化參數對雲微物理變數造成的修正。此研究中證實新的方法能夠更有效的利用 Z_{DR} 的觀測增量來降低 Z_{DR} 的誤差。雲微物理變數的彈性調整以及同化雙偏極化參數對於動力與熱力場的調整有助於改善短時定量降水預報的表現。

Abstract

This study applied WRF-LETKF Radar Assimilation System (WLRAS) to assimilate polarimetric parameters, i.e. differential reflectivity (Z_{DR}) and specific differential phase (K_{DP}), in addition to radial wind (V_r) and reflectivity (Z_H) which is commonly used in radar data assimilation. Besides, a new approach is developed to make use of the high correlation between mean diameter and Z_{DR} to extract more correction from Z_{DR} innovation. It updates normalized intercept parameter (N_w) and mass-weighted mean diameter (D_m) diagnosed from original model variables, mixing ratio and total number concentration. Two real cases, including squall lines forced by synoptic southwestern wind and a local afternoon thunderstorm, are selected to conduct the assimilation experiments with four different microphysics parameterization (MP) schemes, GCE, WSM6, WDM6 and MOR. A series of experiments are conducted to evaluate the performance of the analysis and the quantitative precipitation forecast (QPF). The results show that assimilating additional Z_{DR} with single moment schemes deteriorates the analysis field of Z_H and K_{DP}. Errors of Z_{DR} and K_{DP} can decrease simultaneously when all the polarimetric parameters are assimilated with double moment schemes. The new approach reduces more Z_{DR} errors through the high correlation between D_m and Z_{DR}. In addition to the correction in microphysical states, assimilating additional polarimetric parameters can adjust water vapor and enhance vertical velocity in the strong convective region. Heavy rainfall forecast performs better even in the experiments assimilating Z_{DR} with single moment schemes. In conclusion, there is limitation in assimilating additional polarimetric parameters with single moment schemes, and double moment schemes have more flexibility to adapt the adjustment in hydrometeor variables from assimilating additional polarimetric parameters. It is confirmed that the new approach can extract more correction from Z_{DR} innovation. The flexible correction in microphysical states and the adjustment in dynamical and thermodynamical fields help to improve the performance of short-term QPF.

Acknowledgment

不知不覺在中央大學已經待了六年，研究所的這兩年的心境跟大學時期差很多，收起玩樂的心沉浸在研究當中。雖然嘴上總是說唸大氣系將來沒工作，但是這兩年的研究生活其實是很充實的，讓我學習到更多新知以及認知到自己有哪些不足的地方。

整個碩班生涯最感謝的就是我的指導老師，鍾高陞老師。在我苦惱著該何去何從的時候建議我留下來，並且帶著我在茫茫學海中探索，在研究上也給了我非常高的自由度讓我可以盡情發揮，因為這樣才讓我能夠擁有現在的成果。感謝雷達氣象實驗室的其他老師們，謝謝廖宇慶老師在大 meeting 上總能提出許多犀利的問題以及給予精神喊話，謝謝張偉裕老師在雙偏極化參數的知識上給予指教，謝謝陳台琦老師偶爾撥空參與大 meeting 並且提供許多寶貴的意見。也要感謝洪景山博士、楊舒芝博士以及蔡直謙博士願意擔任口試委員，讓這篇論文能夠更加完整，其中特別感謝蔡直謙博士在我做研究的過程中分享了許多同化雙偏極化參數的經驗。

能夠加入雷達氣象實驗室這個大家庭真的很開心，謝謝大柯、立昕、承融、博安總是在我卡關的時候幫我解惑，謝謝同屆的夥伴們，子睿、玉婕、采蓉、詠荃、姵安，相互砥礪一起成長。還有實驗室的其他成員，小那、Allen、伯謙、熠程、Haidy、Nghi、修維、晨語、顯榮、鈞澤，謝謝你們總是讓實驗室充滿歡笑。

謝謝皓威、浩倫、武男，雖然只有一個禮拜一次在吉米熊吃飯聊天，但總是能讓研究生活變得沒有那麼苦悶。謝謝柏儒跟齊祐不時跑來我的租屋處串門子，讓我的獨居生活增添了一些歡樂。謝謝余嘉裕老師的推薦以及 Uncle Bob 的冠名讓我能夠領到中華扶輪教育基金會提供的豐厚獎學金。最後謝謝我的家人們在我的背後做最大的後盾，讓我能夠順利完成碩班的學位。兩年的碩班告一段落了，接下來又會是一段全新的旅程，我將帶著在中央大學這六年內的所見所聞繼續向前行。

Outline

List of Tables

List of Figures

Chapter 1 Introduction

Meteorology radars are very powerful instruments to observe severe weather systems because they can provide three-dimensional data with high spatial and temporal resolution. Doppler radars transmit electromagnetic wave with horizontal vibration to measure radial wind (V_r) and reflectivity (Z_H), which are related to dynamics and microphysics inside the precipitation system. Recently, most doppler radars are updated to the dual-polarization radar that transmits both horizontal and vertical electromagnetic wave. Comparing the difference between horizontal and vertical return echo, dual-polarization radar can measure polarimetric parameters in addition to V_r and Z_H, i.e. differential reflectivity (Z_{DR}), differential phase (Φ_{DP}), co-pol correlation (ρ_{hv}). Φ_{DP} can be further applied to calculate specific differential phase (K_{DP}). These additional variables provide extra information of hydrometeors. For example, Z_{DR} is related to the shape of hydrometeors, K_{DP} is related to the liquid water content, and ρ_{hv} can be used to classify non-meteorological signal and verify whether the hydrometeors are in uniform formation or mixture form. The information extracted from polarimetric parameters is useful to improve the quality of quantitative precipitation estimation (QPE) (Ryzhkov and Zrnić 1996; Brandes et al. 2002), and the characteristic of polarimetric parameters can be applied in particle identification (PID) to classify different types of hydrometeors (Park et al. 2009). Besides, there are more processes available for radar data quality control (QC) to remove non-meteorological signals with the measurement of polarimetric parameters. Some polarimetric signatures related to the interaction between microphysics and dynamics are also found through the observation of dual-polarization radars, like Z_{DR} column and K_{DP} column collocating with the strong updraft, ring shape ρ_{hv} surrounding the core of updraft near the melting layer and Z_{DR} arc resulted from size sorting (Kumjian and Ryzhkov 2008; Dawson et al. 2014).

For severe convective systems, microphysical processes not only affect the rainfall intensity but also indirectly impact the lifetime and intensity through the interaction with dynamical and thermodynamical processes. Microphysical processes in the high-resolution numerical model rely on the microphysics parameterization (MP) schemes (Lin et al. 1983; Rutledge and Hobbs 1983) since the scale of microphysics processes is much smaller than the model grid resolution. Assumptions given in MP schemes contain uncertainties which will lead to the forecast errors through model integration. As a result, obtaining accurate quantitative precipitation forecast (QPF) of severe convective storms is still very challenging even though high-resolution model can capture very detailed dynamical structure. Data assimilation combines all available information (observation and model) to get the accurate analysis field closer to the unknown truth. With the more accurate analysis fields obtained as initial condition, the performance of QPF is expected to be improved. Assimilating radar observation is the main trend in the researches related to convective system since the high spatial and temporal resolution data can help to capture the rapid evolution inside the convective storm. V_r and Z_H have been widely used in previous studies related to radar data assimilation either through variational method (Sun and Crook 1997; Xiao et al. 2005; Chung et al. 2009) or ensemble Kalman filter (EnKF) (Snyder and Zhang 2003; Zhang et al. 2004; Chang et al. 2014). Nowadays, there are more and more dual-polarization radars; therefore, some recent studies try to assimilate polarimetric parameters in addition to V_r and Z_H to make use of the extra information related to the microphysics processes. WRF-3DVAR has been applied to assimilate polarimetric parameters with a pure warm rain MP scheme (Li and Mecikalski 2010, 2012) while Wu et al. (2000) implemented 4DVAR with a simple ice MP scheme to assimilate polarimetric parameters. The results of the studies mentioned above shows that assimilating additional polarimetric parameters lead to better storm structure and location. Jung et al. (2008a) implemented T-matrix and power law fitting (Zhang et al. 2001) to develop a polarimetric observation operator that can be applied in numerical model validation and data assimilation. Jung et al. (2008b) then applied the operator to assimilate simulated dual-polarization radar observation data in an observation system simulation experiment (OSSE). They found that assimilating additional polarimetric parameters improves the convective scale analysis especially at the later cycles, and they expected there will be more positive improvement if a more complicated MP scheme is applied. Jung et al. (2010) further updated the operator with look-up table and applied it with MY scheme (Milbrandt and Yau 2005). Putnam et al. (2019) first tried to assimilated polarimetric parameters directly through EnKF with the polarimetric operator developed by Jung et al. (2010). In their research, only the Z_{DR} data under 2-km height is assimilated, yet they found that additional assimilation of Z_{DR} can affect grid points higher than 2-km height through the model dynamics and background error covariance. Besides, the mesocycle structure was illustrated in the analysis field after additional Z_{DR} is assimilated at lower levels, indicating the relationship between the polarimetric signature and the dynamical process in the convective storm. Therefore, assimilating additional polarimetric parameters provides not only correction in microphysical variables but also reasonable adjustment in dynamical variables. Zhu et al. (2020) used an OSSE to evaluate how assimilation of additional Z_{DR} affects the analysis field. Their results show that Z_{DR} is highly correlated with vertical velocity, water vapor and temperature perturbation, which indicates the ability of additional Z_{DR} to adjust those variables. They found the analysis is the best if Z_{DR} is able to update all the model variables. Tsai and Chung (2020) assimilated polarimetric parameters to investigate the improvement of QPF for Typhoon Soudelor. The root mean square error (RMSE), spatial correlation coefficient (SCC) and equitable threat score (ETS) of hourly rainfall is improved with the assimilation of Z_{DR} and K_{DP}. You et al. (2020) validated the analysis with the polarimetric parameters and found that assimilating V_r and Z_H might not be sufficient to obtain optimal meso-scale analysis fields, especially when complicated MP schemes are applied.

Although the application of polarimetric parameters in QPE has been operational, assimilation of polarimetric parameters is still in the early stage. Most of the previous studies assimilated polarimetric parameters through retrieved mixing ratio or simple polarimetric operators, and assimilated polarimetric parameters with sophisticated polarimetric operator in an OSSE. Therefore, two real cases with strong convective storms are selected to assimilate polarimetric parameters in addition to V_r and Z_H through the sophisticated polarimetric operator with different MP schemes. The purposes of this study are 1) investigating the improvement with assimilation of polarimetric parameters in different MP schemes; 2) testing a new approach updating normalized intercept parameter (N_w) and mass-weighted mean diameter (D_m) to extract more correction in microphysical variables from Z_{DR} innovation; 3) evaluating the impact on dynamics and thermodynamics with additional assimilation of polarimetric parameters; 4) verifying the improvement in QPF after assimilating additional polarimetric parameters. Chapter 2 introduces the two cases selected in this study. Chapter 3 includes the information about radar data, assimilation system, observation operator and assimilation strategy. Chapter 4 involves the description of verification methods. Chapter 5 provide results of all the experiments conducted in this study. Chapter 6 is devoted to the conclusion of this study and discussion of future works.

Chapter 2 Case Overview

Two different convective storm cases, including a squall line induced by strong southwestern wind and a local afternoon thunderstorm, are selected to conduct assimilation experiments. In addition to occurring under different types of synoptic environment, the microphysical characteristic in these two convective storm cases is also distinct.

2.1 2008/06/14 Squall Line

This case is squall lines occurring over Taiwan Straits during the 8th intense observation period (IOP#8) in the Southwest Monsoon Experiment (SoWMEX) in 2008. From NCEP analysis field (Figure 1 and Figure 2), it is found that South Asia and Southeast Asia was covered by a strong monsoon low. There was an obvious vapor transition band along the edge of the monsoon low at 850 hPa, which transported the warm and moist air from Indian Ocean to South China Sea and East China Sea. Moreover, the low-pressure center near Yangtze River Estuary enhanced the southwestern wind along Taiwan Straits. Above the low-pressure center was an intensive short-wave trough at 500 hPa, and the 5880-gpm contour at 500 hPa was far away from Taiwan, which means that Pacific Subtropical High was relatively weak. With all the factors mentioned above, the unstable synoptic environment induced the squall lines over Taiwan Straits and move toward southwestern Taiwan. At 1100 UTC 14th June 2008, two squall lines are identified: squall line A along the southwestern coast and squall line B over Taiwan Straits (Figure 3). Figure 4 shows that most of the observed Z_{DR} is lower than 1.0 dB even though the corresponding Z_H is higher than 30 dBZ, and the Z_{DR} maximum is lower than 3.0 dB. The large Z_H in the convective systems is caused by a large amount of small raindrops. The 24-hour rainfall accumulation from 0000 LST 14th June to 0000 LST 15th June is higher than 90 mm over southwestern Taiwan, and the maximum exceeded 200.0 mm (Figure 5).

2.2 2020/07/20 Afternoon Thunderstorm

In addition to the convective system induced by the synoptic environment, the second case is an afternoon thunderstorm case on 20th July 2020. The 5880-gpm contour of the 500-hPa geopotential height extended from the Pacific Ocean to Indochina Peninsula. Taiwan was covered by strong Pacific Subtropical High (Figure 6), which is a very typical synoptic environment in Taiwan during the summer time. Although covered by the subtropical high, the convective available potential energy (CAPE) measured in Banqiao station at 0000 UTC was quite a large value, 1198.6 m^2s^2 (Figure 7), which is suitable for convective systems to develop. As expected, with the heating effect in the daytime, several local convective cells occurred at 1300 LST, and those sporadic convective cells developed to strong afternoon thunderstorm. At 1500 LST, there several strong convective cells along Central Mountain Range (Figure 8). This study focuses on the thunderstorm locating in the northern Taiwan. The microphysical characteristic in this thunderstorm case is quite different from the squall line case (Figure 9). The maximum of Z_{DR} is higher than 4.0 dB, and the value of Z_{DR} corresponding to 10 dBZ can range from 0.0 dB to the value higher than 2.0 dB. When the value of Z_H is higher than 30 dBZ, most of the corresponding Z_{DR} is higher than 1.0 dB. This afternoon thunderstorm case shows the diversity of raindrops that the same Z_H might result from a large amount of small raindrops or few large raindrops. The maximum of 3-hour accumulated rainfall in the northern Taiwan from 1400 LST 20th July to 1700 LST 21st July was over 90 mm (Figure 10).

Chapter 3 Experiment Design

3.1 Model Configuration

Weather Research and Forecasting (WRF) version 3.9.1 is applied in this study. It is a three dimensional, non-hydrostatic and fully compressible model predicting three-dimension wind, perturbation potential temperature, perturbation geopotential, water vapor and hydrometeor variables on eta levels which allows model grids to follow the complex terrain. Besides, many physical parameterization schemes, i.e. long (short) wave radiation parameterization schemes, PBL parameterization schemes and MP schemes, are included to deal with the sub-grid physical processes. In this study, four MP schemes, including Goddard Cumulus Ensemble scheme (GCE) (Tao et al. 1989; Tao et al. 2003), Morrison scheme (MOR) (Morrison et al. 2005), WRF Single Moment 6-category scheme (WSM6) (Hong et al. 2006) and WRF Double Moment 6-category scheme (WDM6) (Lim and Hong 2010), are implemented. Three nested model domains are set (Figure 11), 180*150 grid points with 27-km horizontal resolution in the first domain (D01), 165*156 grid points with 9-km horizontal resolution in the second domain (D02) and 210*210 grid points with 3-km horizontal resolution in the third domain (D03). There are totally 52 eta levels with 10-hPa model top. Initial condition and boundary condition are generated from NCEP FNL operational model global tropospheric analyses with 1.0° resolution. Ensemble members are essential in order to conduct EnKF; therefore, horizontal wind field, perturbation potential temperature and water vapor in D01 initial condition and boundary condition are perturbed by WRFDA CV3 background error covariance to create ensemble members. The perturbed initial condition in D01 will be interpolated to D02 and D03, and there will be ensemble members in all three domains' initial conditions ready for ensemble spin-up and data assimilation.

3.2 Radar Data

RCWF, RCCG and RCKT belonging to Central Weather Bureau (CWB) and SPOL belonging to National Center for Atmospheric Research (NCAR) are used to assimilate radar data in this study (Figure 12). In the squall line case on 14th June 2008 during the 2008 SoWMEX, RCWF, RCCG and RCKT scanned with 9 elevation angles (0.5°, 1.4°, 2.4°, 3.4°, 4.3°, 6.0°, 9.9°, 14.6° and 19.5°) and observed reflectivity (Z_H) and radial wind (V_r). SPOL scanned with 9 elevation angles (0.5°, 1.1°, 1.8°, 2.6°, 3.6°, 4.7°, 6.5°, 9.1° and 12.8°) and measured polarimetric parameters, such as differential reflectivity (Z_{DR}), differential phase (Φ_{DP}) and specific differential phase (K_{DP}) in addition to V_r and Z_H. All these four radars provided a complete volume scan every 7.5 minutes. In the afternoon thunderstorm case on 20th July 2020, RCWF has been updated to dual-polarization radar and provided radar data every 6 minutes in 15 elevation angles (0.5°, 0.9°, 1.3°, 1.8°, 2.4°, 3.1°, 4.0°, 5.1°, 6.4°, 8.0°, 10.0°, 12.0°,14.0°, 16.7° and 19.5°).

Radar data quality control (QC) is applied to eliminate non-meteorological signals before using the radar data to any kind of application. RAKIT is a radar data QC package developed by Radar Meteorology Laboratory (RaMeLa) in National Central University (NCU) and is used in this study to get rid of the non-meteorological signal. For the single-polarization radar, the first step of the QC process is to omit the region blocked by terrain, and the second step is to unfold V_r. After these two steps, the final step is to remove the data at the grid point with Z_H greater than 30 dBZ and V_r smaller than 2 m/s. For the dual-polarization radar, the first step is also omitting the blocked region, and the second step is unfolding Φ_{DP}. After Φ_{DP} is unfolded, grid points with ρ_{hv} smaller than 0.85 (0.9 for RCWF in the afternoon thunderstorm case) and standard deviation of Φ_{DP} greater than 10.0 are recognized as non-meteorological signals. After that, Φ_{DP} will be smoothed along the radial direction to remove the noise and then be derived to K_{DP}. The final step is unfolding V_r.

Before applying the radar data in data assimilation, the spatial resolution needs to be reduced to match the model resolution. It will prevent overfitting and satisfy that observation data is uncorrelated in the observation space. There are two main methods to reduce the observation resolution, data thinning and superobbing. Data thinning randomly select one observation grid in a specific region to represent the observation and can properly maintain the strong convective feature. Superobbing averages all the observation data in a specific region to represent the observation and can make the observation more representative with lower observation errors. In this study, superobbing is implemented to average the observation data with Gaussian distance weighting every 5 km in radial direction and every 5° in azimuthal direction for RCWF, RCCG and RCKT; every 4.5 km in radial direction and every 4.5° in azimuthal direction for SPOL (Figure 13).

3.3 Assimilation System

The assimilation system used in this study is WRF-LETKF Radar Assimilation System (WLRAS) developed by Tsai et al. (2014). It couples radar data and model data through Local Ensemble Transform Kalman Filter (LETKF) (Ott et al. 2004; Hunt et al. 2007). LETKF is a kind of deterministic EnKF which is capable to ignore the sampling error resulting from perturbing the observation data. Ensemble mean and ensemble perturbation are updated respectively using the following formulas

$$\overline{\mathrm{X_a}} = \overline{\mathrm{X_b}} + \mathrm{X_b}\overline{\mathrm{W}} \tag{3-1}$$

$$\mathrm{X_a} = \mathrm{X_b}\mathrm{W} \tag{3-2}$$

$\overline{\mathrm{X}}$ is the mean state vector while X is the ensemble perturbation matrix. The subscript a and b represent analysis and background respectively. $\overline{\mathrm{W}}$ and W are the weighting vector and weighting matrix that can be written in the following equations.

$$\overline{\mathrm{W}} = \widetilde{\mathrm{P_a}}\mathrm{Y_b^T}\mathrm{R}^{-1}(\mathrm{y_o} - \overline{\mathrm{H(x_b)}}) \tag{3-3}$$

$$W = [(k-1)\widetilde{P_a}]^{\frac{1}{2}} \tag{3-4}$$

$\widetilde{P_a}$ is the analysis error covariance matrix in the ensemble space, and is defined as

$$\widetilde{P_a} = [(k-1)I/\rho + Y_b^T R^{-1} Y_b]^{-1} \tag{3-5}$$

I is the identical matrix. k is the number of ensemble members. ρ is the inflation factor used to enhance the ensemble spread. Y_b is background ensemble perturbation matrix in observation space and observation states. R is diagonal observation error covariance matrix because observation is assumed to be independent in observation space. There are several advantages using LETKF comparing with variational method. First, with the flow-dependent background error covariance obtained from the ensemble members rather than calculated from climatology, LETKF can generate the increment based on current flow feature instead of the homogeneous increment in 3DVAR. LETKF does not need adjoint model and adjoint operator which are complicated issues in 4DVAR. Therefore, it is much more flexible for LETKF to combine different model and observation. Moreover, localization not only avoid the issue of teleconnection but also make it able to execute parallel calculation, which reduces the computational time efficiently.

Figure 14 shows the assimilation flow charts in the two cases. 50 ensemble members are generated to conduct the assimilation experiments in this study. Before assimilation cycles start, spin-up of ensemble members is essential to generate the meso-scale background field. The spin-up time for the squall line case is 10 hours while the spin-up time for the afternoon thunderstorm case is 13 hours. After the spin-up, radar data will be assimilated every 15 minutes for the squall line case and every 12 minutes for the afternoon thunderstorm case. When the assimilation cycles are done, the analysis will be applied to run short-term deterministic forecasts and ensemble forecasts. Table 1 lists model variables updated by the observation data, localization radii and the inflation factors. In this study, the assimilated variables (V_r, Z_H, Z_{DR} and K_{DP}) are allowed to update all the model variables in Table 1. The observation errors set in the experiments are 3 m/s for V_r, 5 dBZ for Z_H, 0.2 dB for Z_{DR} and 0.5°/km for K_{DP} (Jung et al. 2008b; Tsai and Chung 2020). There are some thresholds for assimilating polarimetric parameters. Z_{DR} and K_{DP} above the 4-km height, mean melting layer height in Taiwan according to Lee et al. (2019), will not be assimilated. Furthermore, negative Z_{DR} and K_{DP} values are eliminated because they are against the theorem that larger raindrops are more oblate. Table 2 shows all the conducted experiments in this study. Scheme_VrZ is the reference to investigate whether there is extra impact in other experiments with the assimilation of polarimetric parameters in addition to V_r and Z_H.

3.4 Observation Operator

Observation operators are the bridge which link model and observation, because model variables and observation variables are seldom the same or at the same location. As a result, there two parts in the observation operator: interpolating model grids to observation grids and converting model variables to observation variables. The interpolation method used in this study is 8-point average which selects 8 model grids surrounding the observation grids and averages them with inverse distance weighting. The variable transformation of V_r is based on Sun and Crook (1997)Sun and Crook (1997)

$$\mathrm{V_r} = \frac{\mathrm{x}}{\mathrm{r}}\mathrm{u} + \frac{\mathrm{y}}{\mathrm{r}}\mathrm{v} + \frac{\mathrm{z}}{\mathrm{r}}(\mathrm{w} - \mathrm{V_t}) \tag{3-6}$$

$$\mathrm{r} = \sqrt{\mathrm{x}^2 + \mathrm{y}^2 + \mathrm{z}^2} \tag{3-7}$$

$$\mathrm{V_t} = 0.54(p_{sfc}/\bar{p})^{0.4}(\rho_a q_r)^{0.125} \tag{3-8}$$

U, V, W are the model three-dimensional wind field while x, y, z are the Cartesian coordinates with origin at the radar site. $\mathrm{V_t}$ is the terminal velocity derived based on Marshall-Palmer raindrop size distribution (Marshall and Palmer 1948). $\mathrm{p_{sfc}}$ and $\bar{\mathrm{p}}$ are surface pressure and base-state pressure respectively. ρ_a is the air density, and q_r is the rain mixing ratio.

For the polarimetric parameters, the polarimetric operator developed by Jung et al. (2008a) is applied to convert model variables to Z_H, Z_{DR} and K_{DP}. The polarimetric operator is based on the bulk microphysics scheme and T-matrix scattering amplitude simulation. In addition, the canting angle of hydrometeors and the hydrometeor mixture form are considered. The equations below are the polarimetric operator in the integration form.

$$Z_{h,x} = \frac{4\lambda^4}{\pi^4|K_w|^2} \int N_x(D)\left(A\left|f_{a,x}(\pi)\right|^2 + B\left|f_{b,x}(\pi)\right|^2 + 2C|f_{a,x}(\pi)||f_{b,x}(\pi)|\right) dD \tag{3-9}$$

$$Z_{v,x} = \frac{4\lambda^4}{\pi^4|K_w|^2} \int N_x(D)\left(B\left|f_{a,x}(\pi)\right|^2 + A\left|f_{b,x}(\pi)\right|^2 + 2C|f_{a,x}(\pi)||f_{b,x}(\pi)|\right) dD \tag{3-10}$$

$$K_{DP,x} = \frac{180\lambda}{\pi} \int N_x(D) C_k \mathrm{Re}\left(f_{a,x}(0) - f_{b,x}(0)\right) dD \tag{3-11}$$

The symbols outside the integration are radar wave length (λ) and dielectric factor (K_w) while others inside the integration are drop size distribution (DSD) of hydrometeors ($N_x(D)$), major axis and minor axis scattering amplitude simulated by T-matrix ($f_{a,x}$ and $f_{b,x}$) and coefficients related to the canting angle of hydrometeors (A, B, C, C_k). Subscript x can be r, s, g and h that represent rain, snow, graupel and hail respectively. The following is the more detailed introduction to each symbol inside the integration.

First, $N_x(D)$ is the hydrometeor DSD that indicates the number of the hydrometeor with specific size. Bin MP schemes and bulk MP schemes are two main method describing the distribution of hydrometeors in the numerical model parameterization. Even though bin MP schemes are theoretically much closer to the reality than bulk MP schemes, bulk MP schemes are still the main trend because of the limitation of computational resources. The hydrometeor DSD is fitted with a function in the bulk MP scheme, and the widely used function is the negative exponential DSD (Marshall and Palmer 1948) and the three-parameter gamma DSD (Ulbrich 1983).

$$N_x(D) = N_{0,x}\exp(-\Lambda_x D) \tag{3-12}$$

$$N_x(D) = N_{0,x}D^{\mu_x}\exp(-\Lambda_x D) \tag{3-13}$$

$N_{0,x}$, μ_x and Λ_x are intercept parameter, shape parameter and slope parameter respectively. The bulk MP schemes applying gamma DSD can be classified to three different type, single moment, double moment and triple moment depending on which parameters are fixed. Single moment schemes, i.e. GCE and WSM6, diagnose Λ_x with the prognostic mixing ratio (q_x) and fix a specific value of $N_{0,x}$ and μ_x (usually equals to 0). Double moment schemes, i.e. MOR and WDM6 diagnose $N_{0,x}$ and Λ_x with the prognostic mixing ratio (q_x) and total number concentration (N_{Tx}), and the value of μ_x is fixed (usually equals to 0). The following formulas show how mixing q_x and N_{Tx} are diagnosed to $N_{0,x}$ and Λ_x in single moment and double moment schemes.

$$\text{Single Moment } \Lambda_x = [\frac{\pi \rho_r N_{0x} \Gamma(\mu_x+4)}{6\rho_a q_x}]^{\frac{1}{\mu_x+4}} \tag{3-14}$$

$$\text{Double Moment } \Lambda_x = [\frac{\pi \rho_r N_{Tx} \Gamma(\mu_x+4)}{6\rho_a q_x \Gamma(\mu_x+1)}]^{\frac{1}{3}} \tag{3-15}$$

$$\text{Double Moment } N_{0x} = \frac{N_{Tx} \Lambda_x^{\mu_x+1}}{\Gamma(\mu_x+1)} \tag{3-16}$$

Usually, bulk microphysics schemes classify hydrometeors to different types, i.e. rain, snow, graupel and hail, but the mixture form of rain water and solid water (snow, graupel and hail), which greatly affects the radar observation, is not considered in MP schemes. Therefore, a mixture model is needed when rain water and solid water (snow, graupel and hail) coexist. The following equation applied in Jung et al. (2008a) represents the fraction of rain water and solid water (snow, graupel and hail) existing in the mixture form.

$$F = F_{max}\left[\min\left(\frac{q_{s,g,h}}{q_r}, \frac{q_r}{q_{s,g,h}}\right)\right]^{0.3} \tag{3-17}$$

F_{max} is the maximum fraction of rain water and solid water (snow, graupel and hail) in the mixture form, and it is set as 0.5 for snow and 0.4 for graupel (hail). Then the mixing ratio of mixture form can be written in the following equation.

$$q_{rs,rg,rh} = F(q_r + q_{s,g,h}) \tag{3-18}$$

Next, $f_{a,x}$ and $f_{b,x}$ are the scattering amplitude calculated by T-matrix, a simulation method which uses environment temperature, particle axis ratio and radar wave length to simulate the electromagnetic wave scattering when the electromagnetic wave hits a nonspherical particle. The scattering amplitude is calculated with the S-band radar wave length (10.7 cm) and the axis ratio of raindrops below.

$$r = 1.0148 - 2.0465 * 10^{-2}D - 2.0048 * 10^{-2}D^2$$
$$+3.095 * 10^{-3}D^3 - 1.45310^{-4}D^4 \tag{3-19}$$

The raindrop is more oblate when the diameter increases. A fixed value of 0.75 is used to represent the axis ratio of ice phase hydrometeors. When the T-matrix simulation is done, the power low fitting is applied to fit the magnitude of f_a and f_b.

$$\left|f_{a,x}(\pi)\right| = \alpha_{a,x}D^{\beta_{a,x}} \tag{3-20}$$

$$\left|f_{b,x}(\pi)\right| = \alpha_{a,x}D^{\beta_{b,x}} \tag{3-21}$$

$$\mathrm{Re}(f_{a,x}(0) - f_{b,x}(0)) = \alpha_{k,x}D^{\beta_{k,x}} \tag{3-22}$$

In addition to considering the hydrometeor DSD, mixture form and the scattering amplitude, falling behavior is also important in order to convert model variables to the reasonable observation radar data. When hydrometeors fall downward to the surfaces, they might tumble and wobble, especially hail. As a result, A, B, C and C_k related to the hydrometeor canting angle are applied in the operator.

$$A = \frac{1}{8}(3 + 4\cos 2\bar{\phi}e^{-2\sigma^2} + \cos 4\bar{\phi}e^{-8\sigma^2}) \tag{3-23}$$

$$B = \frac{1}{8}(3 - 4\cos 2\bar{\phi}e^{-2\sigma^2} + \cos 4\bar{\phi}e^{-8\sigma^2}) \tag{3-24}$$

$$C = \frac{1}{8}(1 - \cos 4\bar{\phi}e^{-8\sigma^2}) \tag{3-25}$$

$$C_k = \cos 2\bar{\phi}e^{-2\sigma^2} \tag{3-26}$$

$\bar{\phi}$ is the mean canting angle while σ represents the standard deviation of the canting angle. The $\bar{\phi}$ of all the hydrometeors is set as 0° and σ is set as 0°, 20° and 60° for rain, snow and dry graupel (hail) respectively. The graupel (hail) will be stabilized if it is covered by the melting water; as a result, the σ of wet graupel (hail) is modified as the formula below.

$$\sigma = 60°(1 - cf_w) \tag{3-27}$$

f_w represents the fraction of rain water within the mixture form. When the water fraction of the wet graupel (hail) is higher, σ will be smaller than 60°, which means the wet graupel (hail) is more stable than the dry graupel (hail). The coefficient c equals to 0.8 when the wet graupel (hail) mixing ratio ($q_{rg,rh}$) is higher than 0.2 g/kg; otherwise, it equals to $4*q_{rg,rh}$

With the three-parameter gamma DSD (3-13), scattering amplitude simulation fit by power low and integration domain set from 0 to infinity, the operator in the integration form, (3-9) to (3-11), can be modified to the following formulas.

$$Z_{h,x} = \frac{4\lambda^4 N_{0,x}}{\pi^4 |K_w|^2}\left(A\alpha_{a,x}^2 \frac{\Gamma(\mu_x+2\beta_{a,x}+1)}{\Lambda_x^{\mu_x+2\beta_{a,x}+1}} + B\alpha_{b,x}^2 \frac{\Gamma(\mu_x+2\beta_{b,x}+1)}{\Lambda_x^{\mu_x+2\beta_{b,x}+1}} + 2C\alpha_{a,x}\alpha_{b,x} \frac{\Gamma(\mu_x+\beta_{a,x}+\beta_{b,x}+1)}{\Lambda_x^{\mu_x+\beta_{a,x}+\beta_{b,x}+1}}\right) \quad (3\text{-}28)$$

$$Z_{v,x} = \frac{4\lambda^4 N_{0,x}}{\pi^4 |K_w|^2}\left(B\alpha_{a,x}^2 \frac{\Gamma(\mu_x+2\beta_{a,x}+1)}{\Lambda_x^{\mu_x+2\beta_{a,x}+1}} + A\alpha_{b,x}^2 \frac{\Gamma(\mu_x+2\beta_{b,x}+1)}{\Lambda_x^{\mu_x+2\beta_{b,x}+1}} + 2C\alpha_{a,x}\alpha_{b,x} \frac{\Gamma(\mu_x+\beta_{a,x}+\beta_{b,x}+1)}{\Lambda_x^{\mu_x+\beta_{a,x}+\beta_{b,x}+1}}\right) \quad (3\text{-}29)$$

$$K_{DP,x} = \frac{180\lambda N_{0,x}}{\pi}\left(\alpha_{k,x} C_k \frac{\Gamma(\mu_x+\beta_{k,x}+1)}{\Lambda_x^{\mu_x+\beta_{k,x}+1}}\right) \quad (3\text{-}30)$$

Each hydrometeor variable including mixture form variable is converted to polarimetric parameters through (3-28) – (3-30), and the linear combination of each category can represent the simulated radar observation.

$$Z_H = \log_{10}(Z_{h,r} + Z_{h,s} + Z_{h,g} + Z_{h,h} + Z_{h,rs} + Z_{h,rg} + Z_{h,rh}) \quad (3\text{-}31)$$

$$Z_V = \log_{10}(Z_{v,r} + Z_{v,s} + Z_{v,g} + Z_{v,h} + Z_{v,rs} + Z_{v,rg} + Z_{v,rh}) \quad (3\text{-}32)$$

$$Z_{DR} = \log_{10}\left(\frac{Z_{h,r}+Z_{h,s}+Z_{h,g}+Z_{h,h}+Z_{h,rs}+Z_{h,rg}+Z_{h,rh}}{Z_{v,r}+Z_{v,s}+Z_{v,g}+Z_{v,h}+Z_{v,rs}+Z_{v,rg}+Z_{v,rh}}\right) \quad (3\text{-}33)$$

$$K_{DP} = K_{DP,r} + K_{DP,s} + K_{DP,g} + K_{DP,h} + K_{DP,rs} + K_{DP,rg} + K_{DP,rh} \quad (3\text{-}34)$$

There are two issues that should be noticed. The first issue is the limitation of ice-phase polarimetric parameters because the axis ratio of ice particle is fixed as 0.75, which makes the power law fitting coefficient $\beta_{a,x}$ and $\beta_{b,x}$ equal to 3.0. With the same power, there is no obvious difference between the major axis scattering amplitude and the minor axis scattering amplitude, so the Z_{DR} and K_{DP} of ice-phase hydrometeors is very close to 0.0, which is not consistent with the real polarimetric observation. The second one is the mixture model. Although the simple mixture model (3-17) is able to consider the existence of hydrometeor in mixture form, it still contains certain level of uncertainty which might result in significant bias when calculating polarimetric parameters at melting layer with certain MP schemes. These two issues indicate why the altitude threshold mentioned in the previous subsection is necessary. When only the polarimetric parameters below the melting layer are assimilated, innovation of Z_{DR} and K_{DP} calculated by ice-phase particle and hydrometeors in mixture form will be eliminated, which prevents unreliable innovation deteriorating the analysis.

3.5 New Approach to Assimilate Polarimetric Parameters

The new approach developed in this study aims for extracting more correction from Z_{DR} innovation to adjust microphysical states. The following equation is the general formula of Kalman Filter.

$$X_a = X_b + BH^T(HBH^T + R)^{-1}(y - H[X_b]) \quad (3\text{-}35)$$

X_a and X_b are the analysis field and background field respectively. y is the assimilated observation. B represents the background error covariance while R represents the observation error covariance. H is the observation operator. Kalman Filter relies on the background error covariance (BH^T) to propagate innovation from observation grids to model grids. The correlation structure can represent the structure of background error covariance. Low correlation means that the background error covariance might not be able to propagate the innovation to correct model variables properly. In order to evaluate the capability of EnKF, it is quite common to select a reference point and calculate the background correlation between model variables and observation variables at that point. In this study, a grid point with max vertical velocity in the convective storm below 4-km height is selected as the reference point. When the reference point is determined, the background correlation between simulated polarimetric parameters at that grid point and model variables can be calculated. Figure 15 shows the vertical cross section of background correlation between hydrometeor variables and Z_{DR} at the grid point with max vertical velocity (black cross) at the 4th cycle (1045 UTC June 14th 2008) in the assimilation period of the squall line case. Although there is a column of high correlation between q_r and Z_{DR} with the maximum higher than 0.7, the correlation coefficient between N_{Tr} and Z_{DR} is lower than 0.4 near the black cross. As a result, there might be less Z_{DR} innovation propagated to the model grids near the black cross to correct N_{Tr}. However, when q_r and N_{Tr} are diagnosed to mean diameter of raindrops, the maximum of correlation coefficient near the black cross is higher than 0.9. It is even higher than the correlation between q_r and Z_{DR}. Small raindrops are spherical with Z_{DR} closer to 0.0 while large raindrops are oblate with larger value of Z_{DR}. Therefore, the extremely high correlation between mean diameter and Z_{DR} is not only a mathematic trick but also satisfying the physical meaning. The new approach makes use of the high correlation between mean diameter and Z_{DR}, so it diagnoses q_r and N_{Tr} to normalized intercept parameter (N_w) and mass-weighted mean diameter (D_m) through the following equations. Nw and Dm will equal to 0.0 if N_{Tr} is less than 100 #/m^3

$$D_m = \frac{4+\mu_r}{\Lambda_r} \tag{3-36}$$

$$N_w = \frac{4^4 \rho_a q_r}{\rho_w \pi {D_m}^4} \tag{3-37}$$

In the Original WLRAS, X_b in (3-35) are the prognostic variables in WRF, i.e. q_r and N_{Tr}. The innovation ($y - H[X_b]$) of V_r, Z_H, Z_{DR} and K_{DP} will be propagated through the background error covariance (BH^T) to correct q_r and N_{Tr}. With the implementation of the new approach, the assimilation observation is the same as the original WLRAS, but X_b in (3-35) will be N_w and D_m instead of qr and N_{Tr}. Therefore, Kalman Filter will calculate the background error covariance (BH^T) between D_m and Z_{DR} and use it to propagate the Z_{DR} innovation to correct D_m. After N_w and D_m are both updated, they will be diagnosed to a new pair of q_r and N_{Tr} with the following equations derived from (3-15), (3-36) and (3-37).

$$q_r = \frac{N_w \rho_w \pi {D_m}^4}{\rho_a 4^4} \tag{3-38}$$

$$N_{Tr} = [\frac{1000(4+\mu)}{D_m}]^3 \frac{6 q_r \Gamma(\mu+1)}{\pi \rho_w \Gamma(\mu+4)} \tag{3-39}$$

With the use of the high correlation between D_m and Z_{DR}, the new approach is expected to extract more correction from Z_{DR} innovation to adjust microphysical states and reduce more Z_{DR} errors.

Chapter 4 Verification Methods

Some methods are used in this study to validate the results quantitatively. Normalized root mean square error (NRMSE) can be used to verify whether the analysis error further decreases or not when polarimetric parameters are assimilated. Contour frequency by altitude diagram (CFAD) is useful to represent vertical structure of observed radar data and simulated polarimetric parameters in the analysis field. In addition to the verification in analysis, forecast skill scores which are commonly used in model validation are applied to evaluate the performance of the short-term QPF after assimilation.

4.1 Normalized Root Mean Square Error (NRMSE)

Root mean square error (RMSE) is usually applied to calculate the difference between analysis and observation during the assimilation period. It is available to check whether the analysis is closer to the assimilated observation. Model variables in model grids are interpolated to observation grids and converted to observation variables through the observation operators and then the difference will be calculated using the following formula.

$$\mathrm{RMSE} = \sqrt{\frac{\sum_{i=1}^{i=N}(X_i - O_i)^2}{N}} \tag{4-1}$$

X_i is the background or analysis in observation space and O_i represents the observation. One of the purposes in this study is to investigate the impact of assimilating polarimetric parameters in addition to V_r and Z_H, so the RMSE of the experiment assimilating additional polarimetric parameters will be divided by the experiment only assimilating V_r and Z_H to calculate normalized RMSE (NRMSE). If NRMSE is smaller than 1.0, the additional assimilation of polarimetric parameters provides extra benefit to improve the analysis; on the other hand, NRMSE larger than 1.0 means that the additional assimilation of polarimetric parameters deteriorates the analysis filed.

4.2 Contoured Frequency by Altitude Diagram (CFAD)

CFAD (Yueter and Houze 1995) is a statistic diagram indicating the data structure along altitude in the specific region. For example, the observed Z_H at plane position indicator (PPI) is interpolated to constant altitude plane position indicator (CAPPI), and the value of Z_H ranging from 0 dBZ to 70 dBZ will be classified to different intervals (Table 6). After the classification is done, the number in each interval will be divided by the total number of the data at the same altitude and then multiply 100% to calculate the frequency (probability) in each interval at each altitude. Besides, the accumulated frequency (probability) can be calculated at each altitude and represents quartiles which indicates the spread of data distribution at each altitude. The signal of K_{DP} is more obvious in the convective region than in the stratiform region; as a result, the data selected to plot CFADs is further separated to convective region and stratiform region with the following definition based on Steiner et al. (1995). If the Z_H at 3-km height is larger than 10 dBZ and smaller than 30 dBZ, the region within the radius of 10 km is recognized as stratiform region. If the Z_H at 3-km height is larger than 40 dBZ, the region within the radius of 5 km is recognized as convective region. The region with Z_H at 3-km height larger than 30 dBZ and smaller than 40 dBZ is defined as the transition region between convective region and stratiform region. Figure 16 shows the selected region for plotting CFADs in the squall line case and the afternoon thunderstorm case.

4.3 Forecast Skill Scores

CWB hourly rainfall observation data is used to verify short-term QPFs with threat score (TS), false alarm ratio (FAR), success ratio and probability of detection (POD) and bias. The model accumulated rainfall is interpolated to observation grids with the model grids near the observation grid, and a certain threshold is set to define whether the precipitation event is observed or predicted. The precipitation events will be classified to four different scenarios, hit, miss, false alarm and correct negative based on the contingency table (Table 7). Hit means the event occurs in both observation and model. Miss means only observation capture the event while false alarm means the event is predicted but is not observed. Correct negative means the event does not happen in both observation and model. After the observation and forecast are classified to these four scenarios, the forecast skill scores can be calculated with the following formulas.

$$\mathrm{POD} = \frac{\mathrm{Hit}}{\mathrm{Hit+Miss}} \tag{4-2}$$

$$\mathrm{FAR} = \frac{\mathrm{False\ Alarm}}{\mathrm{Hit+False\ Alarm}} \tag{4-3}$$

$$\mathrm{SR} = \frac{\mathrm{False\ Alarm}}{\mathrm{Hit+False\ Alarm}} = 1 - \mathrm{FAR} \tag{4-4}$$

$$\mathrm{Bias} = \frac{\mathrm{Hit+False\ Alarm}}{\mathrm{Hit+Miss}} \tag{4-5}$$

$$\mathrm{TS} = \frac{\mathrm{Hit}}{\mathrm{Hit+Miss+False\ Alarm}} \tag{4-6}$$

POD represents how many observed events are exactly forecasted, and the value is from 0 to 1. If every observed event is forecasted, the value of POD equals to 1. FAR indicates how many forecasted events are not observed, and the value is from 0 to 1. If all the forecasted events are not observed, the value of FAR equals to 1. SR is opposite to FAR, which shows how many forecasted events are correctly observed. Bias is the ratio between forecasted events and observed events, and the value of bias is from 0 to infinity. Bias larger than 1 means the model overforecasts while bias less than 1 means the model underforecasts. TS states that how many observed or forecasted events are observed and forecasted simultaneously, and the value of TS is from 0 to 1. If the value of TS equals to 1, the model successfully forecasts all the observed events. The information of POD, SR, bias and TS can be presented in the performance diagram with SR as the horizontal axis and POD as the vertical axis (Roebber 2009). The straight line represents the bias and the curve illustrate the TS. Being closer to the upper right corner means that the forecast performance is better, i.e. Figure 72. In addition, spatial correlation coefficient

(SCC) can verify whether the pattern of rainfall distribution consistent with the observation. The following formula is used to calculate Pearson correlation coefficient.

$$r = \frac{\sum_{i=1}^{i=N}(F_i - \bar{F})(O_i - \bar{O})}{\sqrt{\sum_{i=1}^{i=N}(F_i - \bar{F})^2}\sqrt{\sum_{i=1}^{i=N}(O_i - \bar{O})^2}} \tag{4-7}$$

F_i and O_i represent forecast and observation in the observation grids respectively while $\bar{F}$ and $\bar{O}$ represent spatial mean of forecast and observation. The value of r is between -1.0 and 1.0, and 1.0 means that the spatial pattern of the forecast consistent with observation.

Chapter 5 Results

In this section, performance of both analysis and short-term forecast are investigated and examined. The first four subsections focus on evaluating the impact on analysis with additional assimilation of polarimetric parameters, and the final subsection is to assess the performance of short-term QPF after data assimilation.

5.1 Performance of Single Moment Schemes

5.1.1 Squall Line Case

The NRMSE of Z_H and K_{DP} (Figure 17a, c and Figure 18a, c) in the final cycle is higher than 1.0 while the NRMSE of Z_{DR} (Figure 17b and Figure 18b) is lower than 1.0 in GCE_VrZZdr and WSM6_VrZZdr. It shows that assimilating additional Z_{DR} with single moment schemes deteriorates the analysis field of Z_H and K_{DP}. Assimilating additional K_{DP} decreases the error of K_{DP} (Figure 17f and Figure 18f) and does not increase the error of Z_H and Z_{DR} (Figure 17d,e and Figure 18d,e) in GCE_VrZKdp and WSM6_VrZKdp, which indicates assimilating additional K_{DP} with single moment schemes improves the analysis of K_{DP} and does not deteriorate the analysis of Z_H and Z_{DR}. In GCE_VrZZK and WSM6_VrZZK, the NRMSE of Z_{DR} (Figure 17h and Figure 18h) is lower than 1.0 while the NRMSE of Z_H and K_{DP} (Figure 17g,i and Figure 18g,i) is still higher than 1.0 but lower than GCE_VrZZdr and WSM6_VrZZdr, which indicates the negative impact caused by assimilating additional Z_{DR} is suppressed.

Figure 19 and Figure 20 list all the CFADs of polarimetric parameters in the experiments with single moment schemes. The frequency of Z_H between 25 dBZ and 35 dBZ at lower levels is smaller, and the 2nd quartile of Z_H at lower levels is less than GCE_VrZ, WSM6_VrZ and SPOL observation in GCE_VrZZdr and WSM6_VrZZdr (Figure 19g and Figure 20g). The difference in Z_H CFADs indicates that the precipitation system becomes weaker when additional Z_{DR} is assimilated with single moment schemes. The frequency of small Z_{DR} increases in

GCE_VrZZdr and WSM6_VrZZdr, which makes the Z_{DR} quartiles smaller and closer to the SPOL observation (Figure 19h and Figure 20h). The overall mean diameter of raindrops in the precipitation system becomes smaller and closer to the observed Z_{DR}. Same as the Z_H CFAD, assimilating additional Z_{DR} increases the frequency of small K_{DP} and decreases the 3rd quartile of K_{DP} (Figure 19i and Figure 20i), which means the intensity of strong convection is weakened when additional Z_{DR} is assimilated. With additional assimilation of K_{DP}, the frequency of Z_H and Z_{DR} in GCE_VrZKdp and WSM6_VrZKdp (Figure 19j,k and Figure 20j,k) is similar to GCE_VrZ and WSM6_VrZ (Figure 19d,e and Figure 20d,e). The quartiles of K_{DP} (Figure 19l and Figure 20l) are larger than GCE_VrZ and WSM6_VrZ (Figure 19f and Figure 20f), which means that the intensity of the strong convection is enhanced when additional K_{DP} is assimilated. When all the additional polarimetric parameters are assimilated, the CFADs of Z_H and Z_{DR} in GCE_VrZZK and WSM6_VrZZK (Figure 19m,n and Figure 20m,n) does not show obvious difference comparing with GCE_VrZZdr and WSM6_VrZZdr (Figure 19g,h and Figure 20g,h), but the 2nd and 3rd quartiles of K_{DP} in GCE_VrZZK and WSM6_VrZZK (Figure 19o and Figure 20o) are larger than GCE_VrZZdr and WSM6_VrZZdr (Figure 19i and Figure 20i) but smaller than GCE_VrZKdp and WSM6_VrZKdp (Figure 19l and Figure 20l). One should notice that assimilating additional K_{DP} is able to enhance the strong convection, yet the improvement of K_{DP} is limited when Z_{DR} and K_{DP} are both assimilated.

After the overall comparison in CFADs, spatial distribution at constant altitudes can further check and confirm the difference in the squall lines resulting from assimilating additional polarimetric parameters. Figure 21 and Figure 22 display the spatial distribution of Z_H, Z_{DR} and K_{DP} at 3-km height. The intensity of the two squall lines is weaker from the view of Z_H with the additional assimilation of Z_{DR} in GCE_VrZZdr and WSM6_VrZZdr (Figure 21g and Figure 22g) but is stronger with the additional assimilation of K_{DP} in GCE_VrZKdp and WSM6_VrZKdp (Figure 21j and Figure 22j). Z_{DR} in both squall line A and B is overestimated in GCE_VrZ in WSM6_VrZ (Figure 21e and Figure 22e), and it is corrected in GCE_VrZZdr and WSM6_VrZZdr (Figure 21h and Figure 22h) with additional assimilation of Z_{DR} yet is still overestimated. K_{DP} in both squall line A and B is underestimated in GCE_VrZ and WSM6_VrZ (Figure 21f and Figure 22f), especially squall line B. Assimilating additional K_{DP} corrects the underestimated K_{DP} in squall line A (Figure 21l and Figure 22l) but makes more overestimation of Z_{DR} in squall line A (Figure 21k and Figure 22k). It is obvious in the spatial distribution that the pattern of Z_H, Z_{DR} and K_{DP} is exactly the same. When Z_{DR} is corrected to a smaller value, Z_H and K_{DP} also become smaller; on the contrary, when K_{DP} is corrected to a larger value, the value of Z_H and Z_{DR} also become larger. The result of CFADs and spatial distribution of polarimetric parameters at 3-km height corresponds to the result of NRMSE that assimilating additional Z_{DR} with single moment scheme decreases the error of Z_{DR} yet slightly increases the error of Z_H and K_{DP}.

5.1.2 Afternoon Thunderstorm Case

The result of NRMSE in the afternoon thunderstorm case also shows that the error of Z_H and K_{DP} increases in GCE_VrZZdr and WSM6_VrZZdr (Figure 23a,c and Figure 24a,c). Differ from the squall line case, GCE_VrZKdp and WSM6_VrZKdp decrease the error of both Z_H and Z_{DR} (Figure 23d,e and Figure 24d,e) in the early cycles. This result indicates that assimilating additional K_{DP} with single moment schemes helps to construct the afternoon thunderstorm more efficiently. With additional Z_{DR} and K_{DP} assimilated, the negative impact on Z_H analysis and K_{DP} analysis in the later cycles resulting from Z_{DR} is suppressed (Figure 23g and Figure 24g). The positive impact of assimilating additional K_{DP} seems to be more obvious in the experiments with WSM6 scheme since the NRMSE of K_{DP} in WSM6_VrZKdp (Figure 23f) is smaller than GCE_VrZKdp (Figure 24f).

Figure 25 and Figure 26 display CFADs in all the experiments with single moment schemes. Assimilating additional Z_{DR} (Figure 25g and Figure 26g) corrects the overestimation of 1st and 2nd Z_H quartiles in GCE_VrZ and WSM6_VrZ (Figure 25d and Figure 26d), yet the 3rd quartile is lower than RCWF observation, which means the intensity of strong convection is weakened when additional Z_{DR} is assimilated. The frequency maximum of Z_{DR} moves to smaller Z_{DR}, and quartiles of Z_{DR} are smaller in GCE_VrZZdr and WSM6_VrZZdr (Figure 25h and Figure 26h) The 3rd quartile is even underestimated in WSM6_VrZZdr comparing with the observation. The overall mean size of raindrops tends to be smaller when additional Z_{DR} is assimilated. After assimilating additional Z_{DR}, quartiles of K_{DP} (Figure 25i and Figure 26i) are seriously underestimated and the distribution of frequency is very narrow comparing with the observation CFAD, which is consistent with the result in Z_H CFADs that the strong convection becomes weaker when additional Z_{DR} is assimilated. With additional assimilation of K_{DP}, the afternoon thunderstorm is enhanced with the 3rd quartile of Z_H closer to observation in GCE_VrZKdp and WSM6_VrZKdp; however, the 1st and 2nd quartiles of Z_H are overestimated (Figure 25j and Figure 26j). The quartiles of Z_{DR} slightly increase in GCE_VrZKdp (Figure 25k) and obviously increase in WSM6_VrZKdp (Figure 26k), which means the mean raindrop size becomes larger. The CFAD of K_{DP} also changes slightly in GCE_VrZKdp (Figure 25l), but it is significantly improved and is very close to observation in WSM6_VrZKdp (Figure 26l). It echoes the result in the NRMSE of K_{DP} that the NRMSE of K_{DP} in WSM6_VrZKdp is smaller than GCE_VrZKdp. With additional assimilation of both Z_{DR} and K_{DP}, CFADs of GCE_VrZZK and GCE_VrZZK (Figure 25m,n,o and Figure 26m,n,o) are closer to those of GCE_VrZZdr and WSM6_VrZZdr (Figure 25g,h,i and Figure 26g,h,i), which indicates the weighting of assimilated Z_{DR} might be higher than assimilated K_{DP}.

From the spatial distribution at 3-km height (Figure 27 and Figure 28), Z_H in the thunderstorm becomes weaker with additional assimilation of Z_{DR} in GCE_VrZZdr and WSM6_VrZZdr (Figure 27g and Figure 28g), especially in WSM6_VrZZdr; on the other hand, the thunderstorm becomes stronger from the view of Z_H with additional assimilation of K_{DP} in GCE_VrZKdp and WSM6_VrZKdp (Figure 27j and Figure 28j). When the value of Z_H is higher, the value of Z_{DR} and K_{DP} is higher simultaneously, and vice versa, which is consistent with the results in the squall line case.

5.1.3 Preliminary Summary

The identical results in these two cases illustrate the limitation of assimilating additional polarimetric parameters with single moment schemes. Although different polarimetric parameters can be calculated through the polarimetric operator, all of them are only determined by mixing ratio if a single moment scheme is applied. When mixing ratio is higher, the value of all the polarimetric parameters is higher, vice versa; therefore, it is impossible to find high Z_H collocating with low Z_{DR} with the implementation of single moment schemes. Comparing with observation in these two cases, K_{DP} is underestimated while Z_{DR} is overestimated when polarimetric parameters are not assimilated. Assimilating additional Z_{DR} make the analysis Z_{DR} smaller, and it also means that other polarimetric parameters should be smaller. As a result, assimilating additional polarimetric parameters with single moment schemes in certain case without all the polarimetric parameters underestimated or overestimated comparing with observation will limit the positive impact and might even deteriorate the analysis obtained through assimilating V_r and Z_H.

5.2 Performance of Double Moment Schemes

Unlike single moment schemes, double moment schemes predict both mixing ratio and total number concentration, and they might have more flexibility to adapt the adjustment resulting from assimilating additional polarimetric parameters.

5.2.1 Squall Line Case

The NRMSE of Z_H and K_{DP} (Figure 29a,c and Figure 30a,c) in the final cycle is not higher than 1.0, and the NRMSE of Z_{DR} (Figure 29b and Figure 30b) is lower than 1.0 in WDM6_VrZZdr and MOR_VrZZdr. Differ from single moment schemes, the analysis fields of Z_H and K_{DP} are not deteriorated when additional Z_{DR} is assimilated with double moment schemes. When both Z_{DR} and K_{DP} are assimilated, the error of all the polarimetric parameters can further reduce simultaneously in WDM6_VrZZK and MOR_VrZZK (Figure 29g,h,i and

Figure 30g,h,i), which is very different from the experiments with single moment schemes.

Figure 31 and Figure 32 list the CFADs of polarimetric parameters. The quartiles of Z_H in WDM6_VrZZdr (Figure 31g) is smaller than WDM6_VrZ (Figure 31d), and the frequency of Z_H between 25 dBZ and 30 dBZ is higher. The intensity of the squall lines is slightly weaker when additional Z_{DR} is assimilated with WDM6. The quartiles of Z_{DR} in WDM6_VrZZdr (Figure 31h) is also smaller, and the frequency of Z_{DR} lower than 1 dB is higher with additional assimilation of Z_{DR}; in the meantime, the 3rd quartile of K_{DP} in WDM6_VrZZdr (Figure 31i) is larger than WDM6_VrZ (Figure 31f). Assimilating Z_{DR} corrects the overestimation of simulated Z_{DR} and maintains the intensity of the strong convection. Same as WDM6_VrZZdr, quartiles of Z_H is smaller in MOR_VrZZdr (Figure 32g), but the reduction of Z_H is not as much as WDM6_VrZZdr (Figure 31g). Quartiles of Z_{DR} is smaller but still overestimated (Figure 32h), and the 2nd and 3rd quartiles of K_{DP} (Figure 32i) is slightly larger. Double moment schemes are able to correct the overestimated mean size of raindrops without deteriorating the intensity of the precipitation system. With additional assimilation of K_{DP}, there is no significant difference in the CFADs of Z_H and Z_{DR} (Figure 31j,k and Figure 32j,k), but the 3rd quartile of K_{DP} increases in WDM6_VrZKdp and MOR_VrZKdp (Figure 31l and Figure 32l). The strong convection is more intense when additional K_{DP} is assimilated. When both additional Z_{DR} and K_{DP} are assimilated, the CFADs of Z_H and Z_{DR} in WDM6_VrZZK and MOR_VrZZK (Figure 31m,n and Figure 32m,n) are very close to WDM6_VrZZdr and MOR_VrZZdr (Figure 31g,h and Figure 32g,h). The 3rd quartile of K_{DP} in WDM6_VrZZK and MOR_VrZZK (Figure 31o and Figure 32o) is larger than WDM6_VrZZdr, WDM6_VrZKdp, MOR_VrZZdr and WDM6_VrZKdp (Figure 31i,l and Figure 32i,l). Assimilating both Z_{DR} and K_{DP} enhances the intensity of strong convection more than only assimilating either Z_{DR} or K_{DP}.

Spatial distribution of polarimetric parameters at 3-km height is displayed in Figure 33 and Figure 34. With the additional assimilation of Z_{DR}, the value of Z_H in squall line A is slightly smaller in WDM6_VrZZdr and MOR_VrZZdr, but the reduction of Z_H is not very significant

(Figure 33g and Figure 34g). The overestimation of Z_{DR} is corrected in squall line A in WDM6_VrZZdr (Figure 33h) while the exaggerated overestimation of Z_{DR} is corrected yet still overestimated in both squall line A and B in MOR_VrZZdr (Figure 34h). The value of K_{DP} in squall line A is larger in MOR_VrZZdr (Figure 34i), so is the value of K_{DP} in the southern part of squall line B in WDM6_VrZZdr (Figure 33i). With the additional assimilation of K_{DP}, the value of Z_H in squall line A becomes larger in WDM6_VrZKdp and MOR_VrZKdp (Figure 33j and Figure 34j), so does the value of K_{DP} in the squall line A (Figure 33l and Figure 34l). The value of Z_{DR} in squall line A is overestimated more in WDM6_VrZKdp and MOR_VrZKdp (Figure 33k and Figure 34k). With assimilation of both additional Z_{DR} and K_{DP}, the spatial distribution of polarimetric parameters of WDM6_VrZZK is similar to WDM6_VrZZdr, and the overestimation of Z_{DR} in squall line A is corrected more in MOR_VrZZK than in MOR_VrZZdr.

5.2.1 Afternoon Thunderstorm Case

The NRMSE of Z_H and K_{DP} is higher than 1.0 in WDM6_VrZZdr, which indicates the analysis of Z_H and K_{DP} is degraded when assimilating Z_{DR}. The result is similar to single moment schemes (Figure 35a,c). On the contrary, the NRMSE of Z_{DR} is lower than 1.0 in the 2nd cycle in MOR_VrZZdr, and the NRMSE of all the polarimetric parameters is lower than 1.0 in the 3rd cycle (Figure 36a,b,c). MOR scheme still has the capability to modify the mean size of raindrops without deteriorating the analysis of Z_H and K_{DP} in this case. With the additional assimilation of K_{DP}, the NRMSE of all polarimetric parameters is smaller than 1.0 in WDM6_VrZKdp (Figure 35d,e,f), so is the NRMSE in MOR_VrZKdp in the intermediate cycles (Figure 36d,e,f). With both additional Z_{DR} and K_{DP} assimilated, the NRMSE of all polarimetric parameters can be lower than 1.0 at the same time in WDM6_VrZZK and MOR_VrZZK (Figure 35g,h,i and Figure 36g,h,i), which is consistent with the result in the squall line case.

Figure 37 and Figure 38 are the CFADs of polarimetric parameters. Quartiles of Z_H, Z_{DR}

and K_{DP} are smaller in WDM6_VrZZdr (Figure 37d,e,f), which means the thunderstorm is weaker with smaller raindrops after assimilating additional Z_{DR}. In WDM6_VrZKdp, the 3rd quartile of Z_H (Figure 37j) is larger and closer to observation, and the quartiles of Z_{DR} is also closer to observation (Figure 37k). It shows that assimilating additional K_{DP} makes the thunderstorm more intense with larger raindrops. When both additional Z_{DR} and K_{DP} are assimilated, the quartiles of Z_H, Z_{DR} and K_{DP} in WDM6_VrZZK are larger than WDM6_VrZZdr and smaller than WDM6_VrZKdp. MOR_VrZZdr corrects the overestimation of 1st and 2nd Z_H quartiles and Z_{DR} quartiles but underestimates the 3rd Z_H quartile (Figure 38g,h). Although the K_{DP} quartiles also decrease in MOR_VrZZdr, the frequency distribution is wider (Figure 38i). The overall intensity of strong convection becomes slightly weaker when additional Z_{DR} data is assimilated. When the both additional Z_{DR} and K_{DP} are assimilated, the 1st Z_{DR} quartile is even smaller in MOR_VrZZK (Figure 38n) comparing with MOR_VrZZdr (Figure 38h); moreover, the frequency distribution of K_{DP} in MOR_VrZZK (Figure 38o) is wider than MOR_VrZKdp (Figure 38l), but the K_{DP} quartiles are smaller.

The spatial distribution of the experiments with WDM6 scheme (Figure 39) shows the similar phenomenon in the experiment with single moment schemes that the pattern of Z_H, Z_{DR} and K_{DP} is the same, larger Z_H collocating with larger Z_{DR} (K_{DP}). The afternoon thunderstorm case has strong and deep convection, so the cold rain process above melting layer plays an important role. In WDM6, only liquid-phase hydrometeors (cloud and rain) are double moment while all the ice-phase hydrometeors (ice, snow and graupel) are single moment, which might make the performance of assimilating polarimetric parameters similar to single moment schemes in this case study. Moreover, it is found that smaller Z_H can collocate with larger Z_{DR} in the experiments with MOR scheme (Figure 40), which seems to further indicate that MOR scheme is more flexible than WDM6 scheme. However, the experiments with MOR scheme still fail to capture the detailed structure of observed Z_{DR} because of the model resolution. The spatial distribution of the thunderstorm is narrower in MOR_VrZZdr (Figure 40g), yet the spatial distribution of Z_H larger than 40 dBZ is wider than MOR_VrZ (Figure 40d). The extreme value of K_{DP} in MOR_VrZZdr (Figure 40i) is higher than MOR_VrZ (Figure 40c) and even higher than MOR_VrZKdp (Figure 40l). The exaggerated overestimation of Z_{DR} along the northwestern coast is not corrected, even if all the polarimetric parameters are assimilated.

5.2.3 Preliminary Summary

With two different prognostic hydrometeor variables, q_x and N_{Tx}, double moment schemes should be more flexible to adjust the microphysical states with additional assimilation of polarimetric parameters. In the experiments with double moment schemes, it is found that assimilating additional polarimetric parameters not only reduce the error of assimilated polarimetric parameters but also does not deteriorate the analysis obtained through assimilating V_r and Z_H. When all the polarimetric parameters are assimilated, the dilemma in the experiments with single moment schemes does not occur. Moreover, the spatial distribution of polarimetric parameters indicates that larger Z_H is no longer essential to collocate with larger Z_{DR} when a double moment scheme is applied. However, the performance of the experiment with WDM6 scheme is similar to the experiments with single moment schemes in the afternoon thunderstorm case. This result indicates that there will be more flexibility to adapt the adjustment from polarimetric parameters in the deep convection if every hydrometeor is in double moment.

5.3 Performance of the New Approach

Since the N_0 is changeable in double moment schemes, the number of small particles might be less, which means the mean diameter can be larger than single moment scheme. The overestimation of Z_{DR} might be more serious than single moment schemes. The results in the previous subsection shows that Z_{DR} in double moment schemes is still seriously overestimated after assimilating additional Z_{DR}, especially in MOR scheme. As a result, the new approach making use of the high correction between Z_{DR} and D_m to update N_w and D_m is expected to reduce more value of the overestimated Z_{DR} in double moment schemes.

5.3.1 Squall Line Case

With the implementation of the new approach, the increment of q_r in WDM6_VrZZdr and MOR_VrZZdr (Figure 41a,b) is less than WDM6_VrZZdr_NwDm and MOR_VrZZdr_NwDm (Figure 41c,d). However, there is obvious negative increment of D_m in WDM6_VrZZdr_NwDm and MOR_VrZZdr_NwDm (Figure 42c,d). The NRMSE of Z_{DR} significantly reduces in the first cycle (Figure 43b,e,h,k) and is even less than 0.6 at the 2nd cycle in MOR_VrZZdr_NwDm and MOR_VrZZK_NwDm (Figure 43h,k). The analysis field of Z_{DR} is improved significantly through assimilating Z_{DR} with the new approach. When the error of Z_{DR} significantly decreases, the NRMSE of Z_H and K_{DP} is higher than 1.0 (even higher than 1.4), but the error is suppressed to near 1.0 through the short-term forecast between cycles (Figure 43a,c,g,i). The large NRMSE of Z_H and K_{DP} corresponds to the less increment of q_r while the much smaller NRMSE of Z_{DR} is related to the significant negative increment of D_m. When K_{DP} is also assimilated, the NRMSE of Z_H and K_{DP} will increase less (Figure 43d,f,j,l). The deterioration of Z_H and K_{DP} is slightly suppressed with additional assimilation of K_{DP}.

Figure 44 displays the CFADs of polarimetric parameters. The frequency of Z_{DR} from 0.0 to 1.0 dB is higher in WDM6_VrZZdr_NwDm and WDM6_VrZZK_NwDm (Figure 44e,h), which is quite close to observation. The Z_{DR} quartiles of MOR_VrZZdr_NwDm and MOR_VrZZdr_NwDm (Figure 44k,n) is almost 0.5 dB smaller than MOR_VrZZdr and MOR_VrZZK (Figure 32h,n). With the implementation of the new approach, the overestimated mean size of raindrops is corrected significantly. However, the Z_H quartiles are underestimated and are 5 dBZ smaller than observation in all the experiments assimilating additional Z_{DR} with the new approach (Figure 44d,j). It indicates that the intensity of squall lines is underestimated evidently. With additional assimilation of both Z_{DR} and K_{DP}, the intensity of the precipitation system is a little stronger with underestimation of Z_H slightly corrected (Figure 44g,m), which corresponds to the result of NRMSE that assimilating both Z_{DR} and K_{DP} can slightly decrease the NRMSE of Z_H and K_{DP}. Although the value of Z_H quartiles is seriously underestimated, the value of K_{DP} quartiles are larger and closer to observation in WDM6_VrZZdr_NwDm and WDM6_VrZZK_NwDm (Figure 44f,i), corresponding to that the frequency of Z_H between 50 dBZ and 55 dBZ increases. The signal of extremely strong convection is enhanced when the new approach is applied with WDM6.

Figure 45 shows the spatial distribution of polarimetric parameters at 3-km height. It is obvious in the spatial distribution of Z_{DR} that the noisy Z_{DR} is eliminated, especially in the experiments with MOR; however, the value of Z_{DR} in the squall line A is still overestimated in WDM6 scheme (Figure 45e,h), so is the value of Z_{DR} in both squall line A and B in MOR scheme (Figure 45k,n). The extreme value of K_{DP} in squall line A is overestimated in both WDM6 scheme (Figure 45f,i) and MOR scheme (Figure 45l,o), but pattern of K_{DP} in WDM6 scheme is closer to observation.

5.3.2 Afternoon Thunderstorm Case

Differ from the squall line case, the increment of q_r is higher when the new approach is applied (Figure 46). The increment of D_m is not manifest when the new approach is applied with WDM6; on the contrary, there is a large area with negative D_m increment when the new approach is used with MOR, which is consistent with the result in the squall line case. The NRMSE (Figure 48) indicates that the improvement of Z_{DR} analysis is not as ideal as the squall line case (Figure 43b,h), yet assimilating K_{DP} suppressing the deterioration of analysis Z_H and analysis K_{DP} is still found at the final cycle of WDM6_VrZZK_NwDm (Figure 48d,f) and the 3rd cycle of MOR_VrZZK_NwDm (Figure 48j,l).

Figure 49 are the CFADs of polarimetric parameters in the experiments with the new approach. With additional assimilation of Z_{DR}, quartiles of Z_{DR} is even smaller in WDM6_VrZZdr_NwDm and MOR_VrZZdr_NwDm (Figure 49e,k) than WDM6_VrZZdr and MOR_VrZZdr (Figure 37h and Figure 38h); meanwhile, the 1st Z_H quartile in WDM6_VrZZdr_NwDm and MOR_VrZZdr_NwDm (Figure 49d,j) are also much smaller than observation, WDM6_VrZZdr and MOR_VrZZdr (Figure 37g and Figure 38g). The mean size of raindrops is closer to observation in MOR scheme and underestimated in WDM6 scheme, and the intensity of the afternoon thunderstorm becomes weaker in both WDM6 scheme and MOR scheme. It is also found that the signal of strong convection is enhanced through the new approach with WDM6. The frequency of Z_H between 45 dBZ and 50 dBZ in WDM6_VrZZdr_NwDm and WDM6_VrZZK_NwDm (Figure 49d,g) is higher than WDM6_VrZZdr and WDM6_VrZZK (Figure 37g,m), which corresponds to the wider distribution of K_{DP} frequency (Figure 49f,i). When K_{DP} is also assimilated with the new approach, the afternoon thunderstorm is enhanced with the underestimated Z_H quartiles corrected in WDM6_VrZZK_NwDm and MOR_VrZZK_NwDm (Figure 49g,m).

Figure 50 is the spatial distribution of polarimetric parameters at 3-km height. Similar to the results in the experiments using original WLRAS with WDM6 scheme in the afternoon thunderstorm case, assimilating additional Z_{DR} makes the value of Z_H in the thunderstorm smaller in WDM6_VrZZdr_NwDm (Figure 50d), yet the value of K_{DP} is higher and closer to observation (Figure 50f) comparing with WDM6_VrZZdr (Figure 39i). It is found that the exaggerated overestimation of Z_{DR} outside the northwestern coast is eliminated in MOR_VrZZdr_NwDm and MOR_VrZZK_NwDm (Figure 50k,n). It might result from the threshold of total number concentration set up in the new approach to prevent unrealistic mean diameter. If N_{Tr} is less than 100 #/m^{-3}, N_w and D_m at that grid point will be set to 0.0; therefore, the overestimated Z_{DR} with few raindrops will be eliminated. Same as the results in the squall line case, the Z_{DR} in the region with strong convection is still overestimated but the Z_{DR} outside the strong convection region is significantly corrected. When Z_{DR} and K_{DP} are both assimilated, the value of Z_{DR} in the thunderstorm is even smaller in MOR_VrZZK_NwDm (Figure 50n).

5.3.3 Preliminary Summary

The new approach successfully corrects the overestimation of Z_{DR}, especially the exaggerated overestimation in MOR, yet the value of Z_H is seriously underestimated. It seems that the flexibility of double moment schemes is gone with the implementation of the new approach. Z_{DR} is the function of D_m while Z_H is the function of both N_w and D_m, and the new approach is based on the high correlation between Z_{DR} and D_m; as a result, the correction of D_m might be much more significant than N_w if only additional Z_{DR} is assimilated. In the Gamma DSD, D_m represents the slope parameter while N_w represents the interception parameter. If only D_m is adjusted with N_w nearly fixed, it is the behavior of single moment schemes with fixed N_0 and changeable Λ. Consequently, Z_H is seriously underestimated with the overestimated Z_{DR} being corrected significantly. When additional K_{DP} is also assimilated, there might be more adjustment in N_w, and it is able to slightly correct the underestimation of Z_H. Therefore, when applying the new approach, additional Z_{DR} and K_{DP} had better to be assimilated together to keep the flexibility of double moment schemes and avoid the underestimation of Z_H.

5.4 Impact on Dynamics and Thermodynamics

The feature of EnKF is propagating the observation information through the background error covariance (correlation). In this study, WLRAS allows the assimilated observation to update all the model variables, which means observation related to dynamics (V_r) can update hydrometeor variables while observation related to microphysics (Z_H and other polarimetric parameters) can update dynamical and thermodynamical variables. Therefore, assimilating additional polarimetric parameters not only adjusts hydrometeor variables but also change the dynamical and thermodynamical fields.

5.4.1 Squall Line Case

There is no precipitation system in the background field at the 1st cycle, so Z_H, Z_{DR} and K_{DP} are not capable to update model variables, which corresponds to the NRMSE in all the experiments equals to 1.0 in the beginning. As a result, the increment of vertical velocity and water vapor is calculated at the 2nd cycle in order to evaluate the impact of assimilating polarimetric parameters on dynamics and thermodynamics. The increment of vertical velocity does not show obvious difference at the 2nd cycle, so Figure 51 to Figure 54 display the increment of water vapor. When additional Z_{DR} is assimilated with GCE scheme and WSM6 scheme, the positive water vapor increment in GCE_VrZZdr and WSM6_VRZZdr is less than GCE_VrZ and WSM6_VrZZdr (Figure 51a,b and Figure 52a,b). Water vapor increment reduces obviously in WDM6_VrZZdr comparing with WDM6_VrZ, and it increases significantly in MOR_VrZZdr comparing with MOR_VrZ. It might result from that MOR scheme tends to simulate raindrops with large mean diameter while WDM6 scheme tends to simulate smaller mean raindrop size. Therefore, Z_{DR} innovation in the experiments with MOR scheme is much higher than the experiments with WDM6 scheme. The pattern of increment in the experiments with additional assimilation of K_{DP} (Figure 51c, Figure 52c, Figure 53c, Figure 54c) is similar to the experiments which assimilate V_r and Z_H (Figure 51a, Figure 52a, Figure 53a, Figure 54a) with the increment slightly higher, and this result might indicate that Z_H and K_{DP} provide similar information. When both additional Z_{DR} and K_{DP} are assimilated, the impact of assimilated K_{DP} is overwhelmed by assimilated Z_{DR}.

Figure 55 to Figure 58 are the difference of analysis mean between experiments with additional assimilation of polarimetric parameters and experiments without it at the final cycle. Although the positive water vapor increment reduces at the early cycle when additional Z_{DR} is assimilated with single moment schemes, there is positive water vapor difference in the final analysis in GCE_VrZZdr and WSM6_VrZZdr (Figure 55a and Figure 56a) when all the assimilating cycles are completed. Furthermore, 700-hPa vertical velocity in the squall line A in GCE_VrZZdr and WSM6_VrZZdr (Figure 55b and Figure 56b) is also stronger through the assimilation cycles with additional assimilation of Z_{DR}, especially in GCE_VrZZdr. Differ from the other three MP schemes, 850-hPa water vapor in the final cycle of WDM6_VrZZdr is less than WDM6_VrZZdr (Figure 57a), yet WDM6_VrZZdr still increases the vertical velocity in the squall line A (Figure 57b). MOR_VrZZdr significantly increases 850-hPa water vapor in the southwestern part of Taiwan (Figure 58a), corresponding to the obviously positive water vapor increment (Figure 54b). Unlike the difference caused by assimilating additional Z_{DR}, the difference caused by assimilating additional K_{DP} concentrates in the region with strong convection (Figure 55d,e,f, Figure 56d,e,f, Figure 57d,e,f, Figure 58d,e,f). When both additional Z_{DR} and K_{DP} are assimilated, the difference pattern is almost the same as the experiments with additional assimilation of Z_{DR}, which is consistent with that the increment caused by assimilated K_{DP} is overwhelmed by assimilated Z_{DR} when they are assimilated at the same time. It echoes the result in single moment that the weighting of assimilated Z_{DR} is higher than the weighting of assimilated K_{DP}. With the positive difference of 850-hPa water vapor and 700-hPa vertical velocity collating with the negative difference of 850-hPa divergence, it is very suitable to generate strong convection.

5.4.2 Afternoon Thunderstorm Case

Same as the squall line case, water vapor increment at the 2^{nd} cycle will be calculated in this case. There is no obvious difference in water vapor increment in the experiments that additional polarimetric parameters are assimilated with GCE scheme and WSM6 scheme (Figure 59 and Figure 60) comparing with GCE_VrZ and WSM6_VrZ. When extra K_{DP} is assimilated with WDM6, there is more positive water vapor increment in WDM6_VrZKdp than WDM6_VrZKdp; on the other hand, there is no difference in the water vapor increment between WDM6_VrZ and WDM6_VrZZdr. When both additional Z_{DR} and K_{DP} are assimilated, the water vapor increment is almost the same as WDM6_VrZKdp. It is exactly the same that assimilating additional Z_{DR} with MOR scheme generates much more positive water vapor increment. It is also found in the experiments with MOR scheme that the impact of assimilated K_{DP} is overwhelmed by the impact of assimilated Z_{DR}.

Figure 63 to Figure 66 are the difference of analysis mean between experiments with additional assimilation of polarimetric parameters and experiments without it at the final cycle in the afternoon thunderstorm case. Although there is no obvious difference in the increment at the early cycles in GCE_VrZZdr and WSM6_VrZZdr, water vapor at 850 hPa in GCE_VrZZdr and WSM6_VrZZdr is higher than GCE_VrZ and WSM6_VrZ after the complete assimilation cycles with additional Z_{DR} (Figure 63a, Figure 64a); however, there are negative 500-hPa vertical velocity difference (Figure 63b, Figure 64b) and positive 850-hPa divergence difference (Figure 63c, Figure 64c). It is confirmed again that the weighting of assimilated Z_{DR} is larger because the positive 500-hPa vertical velocity difference in GCE_VrZKdp (Figure 63e) becomes negative difference in GCE_VrZZK (Figure 63h). Same as result in the squall line case, 850-hPa water vapor in WDM6_VrZZdr is lower than WDM6_VrZ (Figure 65a); moreover, there are negative 500-hPa vertical velocity difference and positive 850-hPa divergence difference (Figure 65b,c). 850-hPa water vapor in WDM6_VrZKdp is also lower than WDM6_VrZ (Figure 65d), but there is positive difference in 500-hPa vertical velocity (Figure 65e). The performance of MOR scheme is consistent with the squall line case that assimilating additional Z_{DR} significantly increases water vapor (Figure 66a,j).

5.4.3 Preliminary Summary

From the results of dynamical and thermodynamical fields, it is found that the difference pattern in the experiments with both additional Z_{DR} and K_{DP} assimilated is close to the experiments with only additional Z_{DR} assimilated. This phenomenon might be related to the observation error design in WLRAS. The observation error of Z_{DR} is set as 0.2 dB, which is quite accurate comparing with the model uncertainty. With the results in the difference pattern and the results in the limitation of single moment scheme, it can be confirmed that the weighting of assimilated Z_{DR} is larger than assimilated K_{DP}. When additional Z_{DR} is assimilated with MOR, the water vapor adjustment is much more significant that other schemes because MOR scheme overestimate the value of Z_{DR} more than other MP schemes. The larger innovation of Z_{DR} leads to larger adjustment of water vapor. Even though the precipitation system is weaker from the view of Z_H after assimilating additional Z_{DR} with single moment schemes, water vapor and vertical velocity can still increase since WLRAS updates model variables separately. The increment of water vapor and enhancement of vertical velocity and convergence might be able to reconstruct the strong convection through the dynamical and thermodynamical processes.

5.5 Performance of Short-Term QPF

5.5.1 Squall Line Case

Figure 67 to Figure 71 show the observation rainfall and the analysis mean forecast of each experiment in the squall line case. Although the intensity of squall lines is weaker from the view of Z_H in GCE_VrZZdr and WSM6_VrZZdr, the extreme value in southwestern Taiwan is larger (Figure 67g,h,i, Figure 68g,h,i); on the contrary, the rainfall maximum decreases in WDM6_VrZZdr (Figure 69g,h,i), corresponding to the negative water vapor difference in the final analysis (Figure 57a). Different from WDM6 scheme, assimilating additional Z_{DR} with MOR scheme not only increases the accumulated rainfall but also extends the area of heavy rainfall significantly (Figure 70g,h,i). K_{DP} represents the signal of strong convection, so experiments that assimilate K_{DP} enhance the rainfall intensity (Figure 67j,k,l, Figure 68j,k,l, Figure 69j,k,l and Figure 70j,k,l). When both Z_{DR} and K_{DP} are assimilated, the pattern of 6-hour accumulated rainfall spatial distribution is closer to the experiments only assimilating additional Z_{DR} (Figure 67i,o, Figure 68i,o, Figure 69i,o and Figure 70i,o). The 6-hour accumulated rainfall in WDM6_VrZZdr_NwDm and WDM6_VrZZK_NwDm (Figure 71f,i) is more than WDM6_VrZZdr and WDM6_VrZZK (Figure 69i,o), corresponding to the larger K_{DP} quartiles in WDM6_VrZZdr_NwDm and WDM6_VrZZK_NwDm (Figure 44f,i). On the other hand, The 6-hour accumulated rainfall in MOR_VrZZdr_NwDm and MOR_VrZZK_NwDm (Figure 71l,o) is less comparing with MOR_VrZZdr and MOR_VrZZK (Figure 68i,o), which might be related to the underestimated Z_H caused by the new approach.

Figure 72 lists the performance diagram with 20-mm threshold. For the experiment with GCE scheme (Figure 72a), the performance of the 1-hour rainfall accumulation is better with additional assimilation of either Z_{DR} or K_{DP}. POD and SR are lower at the 1st hour in WSM6_VrZKdp, yet they significantly increase and become higher than WSM6_VrZZdr and

WSM6_VrZZK in the end of the 6-hour forecast (Figure 72b). The performance of the experiment with WDM6 scheme (Figure 72c) shows that WDM6_VrZZK_NwDm makes TS higher; however, the performance of 3-hour rainfall and 6-hour rainfall is similar to each other among all the experiments with WDM6 scheme. For the performance of experiments with MOR scheme (Figure 72d), it is similar to the result of the experiments with GCE scheme that the performance of the 1-hour rainfall accumulation is better when additional Z_{DR} or K_{DP} are assimilated with MOR scheme; furthermore, SR of 6-hour rainfall is closer to 1.0 in all the experiments with MOR scheme, and POD in MOR_VrZZK is the highest. The bias of all the experiments is still less than 1.0 even if additional polarimetric parameters are assimilated, which means the rainfall events captured by the forecast is less than observation. Figure 73 displays the time series of Pearson correlation coefficient. For the experiments with GCE scheme (Figure 73a), the correlation of the 1-hour accumulated rainfall is lower in GCE_VrZZdr and GCE_VrZZK, yet it is higher than GCE_VrZ after 1300 UTC with additional assimilation of Z_{DR} or K_{DP}. The results in the experiments with WSM6 scheme (Figure 73b) is different that the spatial correlation coefficient is lower from 1200 UTC to 1700 UTC in the experiments with additional assimilation of Z_{DR}. The experiments with WDM6 scheme and MOR scheme (Figure 73c,d) indicates that the pattern of accumulated rainfall is closer to the observation with higher correlation coefficient when additional Z_{DR} or K_{DP} are assimilated. With the implementation of the new approach, the correlation is higher in WDM6_VRZZdr_NwDm and lower in MOR_VrZZdr_NwDm.

Figure 74 to Figure 77 are the probability of 6-hour rainfall exceeding 30 mm in all the experiments. Although assimilating extra Z_{DR} data with GCE scheme and WSM6 scheme makes Z_H weaker, the probability of heavy rainfall is still higher than the experiments that only assimilate V_r and Z_H (Figure 74a,b Figure 75a,b). This result echoes to the positive water vapor difference and positive vertical velocity difference (Figure 55a,b, Figure 56a,b). The probability maximum in WDM6_VrZZdr (Figure 76b) is higher than WDM6_VrZ (Figure 76a) even though the rainfall maximum is lower. The probability is much higher when additional Z_{DR} is assimilated with MOR scheme (Figure 77b), and the region with higher probability exactly collocates with the region with observed heavy rainfall. When the new approach is applied, the probability in WDM6_VrZZdr_NwDm and WDM6_VrZZK_NwDm is higher than WDM6_VrZZdr and WDM6_VrZZK; on the contrary, the probability in MOR_VrZZdr_NwDm and MOR_VrZZK_NwDm is lower than MOR_VrZZdr and MOR_VrZZK.

5.5.2 Afternoon Thunderstorm Case

Figure 78 to Figure 82 are the observation rainfall and ensemble mean rainfall forecast of each experiment in the afternoon thunderstorm case. The variability among ensemble members in the afternoon thunderstorm case is very high that the location of the afternoon thunderstorm might be totally different among all the ensemble members. Using the mean of the analysis at the final cycle to run the deterministic forecast might seriously underestimate the rainfall; Therefore, the ensemble members at the final analysis are used to run the ensemble forecasts, and probability matched ensemble mean (PMEM) based on Ebert (2001) is applied to prevent the smooth resulting from averaging directly and emphasize the extreme value. Assimilating additional Z_{DR} with GCE scheme, WSM6 scheme and WDM6 scheme (Figure 78c, Figure 79c and Figure 80c) makes the accumulated rainfall less, especially WSM6_VrZZdr; on the contrary, MOR_VrZZdr generates two regions with obvious rainfall (Figure 81c). Assimilating additional K_{DP} with all four MP schemes can make the spatial distribution of rainfall wider (Figure 78d, Figure 79d, Figure 80d and Figure 81d). When both additional Z_{DR} and K_{DP} are assimilated, the wider distribution caused by assimilating additional K_{DP} still maintains, but the rainfall accumulation is less (Figure 78e, Figure 79e, Figure 80e and Figure 81e). The result of the new approach is consistent with the squall line case that WDM6_VrZZdr_NwDm and WDM6_VrZZK_NwDm (Figure 82b,c) generate more rainfall due to the wider distribution of K_{DP} frequency related to strong convection (Figure 49f,i) while MOR_VrZZdr_NwDm and

MOR_VrZZK_NwDm (Figure 82d,e) generate less rainfall due to the underestimated Z_H.

Figure 83 to Figure 86 are the probability of 1-hour rainfall exceeding 5 mm in all the experiments. Differ from the squall line case, assimilating additional Z_{DR} with GCE scheme, WSM6 scheme and WDM6 scheme no longer increases the probability (Figure 83b, Figure 84b and Figure 85b) because the adjustment in dynamical and thermodynamical fields do not provide positive support to reconstruct the strong convective system. As for MOR, assimilating additional Z_{DR} does increase the probability of exceeding higher threshold, yet the maximum of probability does not collocate with the region with rainfall maximum, which indicates the issue of system shifting. When the new approach is applied in the afternoon thunderstorm case, the result is similar to the squall line case. The probability in WDM6_VrZZdr_NwDm and WDM6_VrZZK_NwDm (Figure 85e,f) is larger than WDM6_VrZZdr and WDM6_VrZZK (Figure 85b,d) while the probability in MOR_VrZZdr_NwDm and MOR_VrZZK_NwDm (Figure 86e,f) is lower than MOR_VrZZdr and MOR_VrZZK (Figure 86b,d).

5.5.3 Preliminary Summary

Assimilating additional polarimetric parameters is able to improve the performance of short-term QPF. The intensity of the precipitation system is weaker in the final analysis of the experiments that assimilates additional Z_{DR} with GCE scheme and WSM6 scheme, yet more accumulated rainfall is predicted due to the adjustment of water vapor and vertical velocity. The adjustment in dynamics and thermodynamics significantly affects the results of QPF. When additional Z_{DR} is assimilated with WDM6 scheme, the accumulated rainfall maximum is reduced due to the reduction of water vapor; on the contrary, assimilating additional Z_{DR} with MOR scheme maintain the intensity of the precipitation system and increase the water vapor, so the accumulated rainfall significantly increases. The rainfall distribution in the experiments that assimilate both additional Z_{DR} and K_{DP} is similar to the experiments that only assimilates additional Z_{DR}. Therefore, it is confirmed again that the weighting of assimilated Z_{DR} is higher than assimilated K_{DP}. In addition to the improvement in rainfall accumulation, the probability of heavy rainfall is higher with assimilation of additional polarimetric parameters, which means assimilating additional polarimetric parameters is capable to improve the performance of heavy rainfall. As for the result with the new approach, both accumulated rainfall and rainfall probability are higher (lower) when the new approach is applied with WDM6 scheme (MOR scheme).

Chapter 6 Summary and Future Works

The purposes of this study are 1) evaluating the impact on analysis with assimilation of polarimetric parameters; 2) testing a new approach which updates N_w and D_m instead of original model variables in double moment schemes; 3) evaluating the impact on dynamics and thermodynamics; 4) verifying the performance of short-term QPF with additional assimilation of polarimetric parameters. WLRAS is implemented to assimilate additional polarimetric parameters with four different MP schemes, GCE, WSM6, WDM6 and MOR. A new approach updating N_w and D_m is applied in WLRAS in order to extract more correction from Z_{DR} innovation. The assimilation experiments are conducted in two real cases, a squall line case and an afternoon thunderstorm case, with distinct microphysical characteristic. The experiments which only assimilate V_r and Z_H are set as the control run to evaluate the impact on analysis and forecast with additional assimilation of polarimetric parameters. With the validation in dynamics, thermodynamics and microphysics and short-term QPF in two real summer cases, this study is summarized as the following points:

1. There is limitation of assimilating additional polarimetric parameters with single moment schemes. Simulated polarimetric parameters are only determined by q_x in single moment schemes, so they are proportional to each other. If the value of Z_H is higher, the value of Z_{DR} is also higher, vice versa. It means that large Z_H can only result from large raindrops, so it is difficult for single moment schemes to decrease the value of Z_{DR} and increase the value of Z_H and K_{DP} simultaneously. When all the polarimetric parameters are assimilated, the adjustment of mixing ratio depends on the weighting of each polarimetric parameter. The observation error of Z_{DR} in this study is much lower than the ensemble spread of simulated Z_{DR}, so the weighting of assimilated Z_{DR} is higher than assimilated Z_H and K_{DP}. With the assimilation of the observed Z_{DR} which is smaller than simulated Z_{DR}, the value of Z_H and K_{DP} will also reduce, which makes the precipitation system weaker from the view

of Z_H.

2. Differ from single moment schemes, double moment schemes are more flexible to adapt the adjustment obtained from assimilating additional polarimetric parameters because the simulated polarimetric parameters are determined by both q_x and N_{Tx}. Theoretically, the intense Z_H in the precipitation system can result from either a large amount of small raindrops or few large raindrops with double moment schemes. Therefore, assimilating both additional Z_{DR} and K_{DP} corrects the underestimation of K_{DP} and reduce the overestimation of Z_{DR}, which makes the analysis errors of Z_{DR} and K_{DP} decrease simultaneously. With the results above, it is confirmed that double moment schemes are more suitable than single moment schemes to be applied in assimilating additional polarimetric parameters. When the warm rain process dominates in the precipitation system (the squall line case), both MOR scheme and WDM6 scheme shows more flexibility comparing with single moment schemes. However, the performance of WDM6 scheme is similar to single moment schemes in the deep convection (the thunderstorm case) in which the cold rain process matters. As a result, applying a MP scheme with all the hydrometeors in double moment, i.e. MOR scheme, is better when assimilating additional polarimetric parameters.
3. Instead of updating mixing ratio and total number concentration, the new approach updates N_w and D_m and is feasible to decrease the error of Z_{DR} significantly. Meanwhile, the threshold of N_{Tr} set up in the conversion of D_m can eliminate the exaggerated overestimation of Z_{DR} resulting from small value of N_{Tr}. However, there is a disadvantage of the new approach that Z_H will be underestimated. The new approach makes use of the high correlation between Z_{DR} and D_m, but Z_H is the function of both N_w and D_m. If there is no obvious adjustment in N_w corresponding to the significant correction in D_m, the impact of the new approach will be similar to the performance of single moment schemes. Fortunately, when both additional Z_{DR} and K_{DP} are assimilated with the new approach, the underestimation of Z_H can be alleviated.

4. Through the cross correlation, assimilating additional polarimetric parameters can affect not only hydrometeor variables but also dynamical and thermodynamical fields. Although assimilating additional Z_{DR} make the precipitation system weaker from the view of Z_H intensity, it might enhance vertical velocity and increase water vapor, especially in the region with strong convection. Assimilating additional Z_{DR} with MOR scheme generates the most significant water vapor adjustment among the four MP schemes. EnKF generates the increment through three components, background correlation, background variance and innovation. The exaggerated overestimation of simulated Z_{DR} in MOR scheme provides more innovation than the other three MP schemes, so it leads to the most significant water vapor adjustment among all the MP schemes.
5. The adjustment of dynamical and thermodynamical fields significantly affects the result of short-term QPF. The accumulated rainfall might still become higher in GCE_VrZZdr and WSM6_VrZZdr if there are positive water vapor difference and positive vertical velocity difference helping to reconstruct the strong convection. On the other hand, the accumulated rainfall might become lower if the adjustment of dynamics and thermodynamics does not have positive support to the convective systems, i.e. WDM6_VrZZdr keep the intensity of the convection but reduces water vapor. Assimilating additional polarimetric parameters not only increases the value of accumulated rainfall but also makes the probability of heavy rainfall higher, which means the performance of heavy rainfall is improved when additional Z_{DR} or K_{DP} are assimilated.

Overall, this study investigates the impact of assimilating additional polarimetric parameters on analysis and short-term QPF through assimilating polarimetric parameters in addition to V_r and Z_H with four MP schemes in two summer cases. Moreover, a new approach is developed and is feasible to enhance the impact of assimilating additional Z_{DR}. There are some works that can be done in the future:

1. The polarimetric operator used in this study could be updated with numerical integration

through look-up table based on (Jung et al. 2010). Moreover, the axis ratio of graupel and hail according to Ryzhkov et al. (2011) can be considered in the operator to deal with polarimetric parameters of ice-phase particles.

2. It is found that assimilating polarimetric parameters with double moment scheme is more suitable than single moment schemes, so a more complicated double moment scheme, i.e. MY scheme, which considers hail and graupel separately, might be a better option of MP schemes to be applied when assimilating polarimetric parameters.
3. Although the overestimated Z_{DR} is corrected significantly with the implementation of the new approach, the value of Z_H is seriously underestimated. Assimilating polarimetric parameters sequentially might be a better strategy when the new approach is applied. For instance, Z_{DR} is assimilated first with the new approach to deal with the overestimated Z_{DR} and then assimilating Z_H and K_{DP} afterward to update q_r and N_{Tr}. This strategy can keep the benefit of updating q_r with assimilated Z_H and K_{DP} and might be capable to correct the underestimated Z_H resulting from the new approach.
4. Increasing the model resolution to 1 km or even higher resolution is essential when dealing with cloud microphysics processes. Besides, it is more capable to assimilate high-dense radar observations.
5. The value of K_{DP} in the non-precipitation region should be 0.0 instead of missing value. K_{DP} is often associated with strong convection or heavy rainfall, yet it should also provide the information of non-precipitation region. Since K_{DP} is the derivation of Φ_{DP}, the value of 0.0 should be meaningful that Φ_{DP} does not change in the non-precipitation region. Assimilation of zero K_{DP} might be very useful to get rid of the fake precipitation signal in the background field.

References

Brandes, E. A., G. Zhang, and J. Vivekanandan, 2002: Experiments in Rainfall Estimation with a Polarimetric Radar in a Subtropical Environment. *Journal of Applied Meteorology*, **41,** 674-685.

Chang, S.-F., Y.-C. Liou, J. Sun, and S.-L. Tai, 2016: The Implementation of the Ice-Phase Microphysical Process into a Four-Dimensional Variational Doppler Radar Analysis System (VDRAS) and Its Impact on Parameter Retrieval and Quantitative Precipitation Nowcasting. *Journal of the Atmospheric Sciences*, **73,** 1015-1038.

Chang, W., K.-S. Chung, L. Fillion, and S.-J. Baek, 2014: Radar Data Assimilation in the Canadian High-Resolution Ensemble Kalman Filter System: Performance and Verification with Real Summer Cases. *Monthly Weather Review*, **142,** 2118-2138.

Chung, K.-S., I. Zawadzki, M. K. Yau, and L. Fillion, 2009: Short-Term Forecasting of a Midlatitude Convective Storm by the Assimilation of Single–Doppler Radar Observations. *Monthly Weather Review*, **137,** 4115-4135.

Dawson, D. T., E. R. Mansell, Y. Jung, L. J. Wicker, M. R. Kumjian, and M. Xue, 2014: Low-Level ZDR Signatures in Supercell Forward Flanks: The Role of Size Sorting and Melting of Hail. *Journal of the Atmospheric Sciences*, **71,** 276-299.

Dolan, B., B. Fuchs, S. A. Rutledge, E. A. Barnes, and E. J. Thompson, 2018: Primary Modes of Global Drop Size Distributions. *Journal of the Atmospheric Sciences*, **75,** 1453-1476.

Ebert, E. E., 2001: Ability of a Poor Man's Ensemble to Predict the Probability and Distribution of Precipitation. *Monthly Weather Review*, **129,** 2461-2480.

Harlim, J., and B. R. Hunt, 2005: Local ensemble transform kalman filter: An efficient scheme for assimilating atmospheric data. *Preprint*.

Hong, S.-Y., J.-H. Kim, J.-o. Lim, and J. Dudhia, 2006: The WRF single moment microphysics scheme (WSM). *Journal of the Korean Meteorological Society*, **42,** 129-151.

Hunt, B. R., E. J. Kostelich, and I. Szunyogh, 2007: Efficient data assimilation for spatiotemporal chaos: A local ensemble transform Kalman filter. *Physica D: Nonlinear Phenomena*, **230,** 112-126.

Jung, Y., G. Zhang, and M. Xue, 2008a: Assimilation of Simulated Polarimetric Radar Data for a Convective Storm Using the Ensemble Kalman Filter. Part I: Observation Operators for Reflectivity and Polarimetric Variables. *Monthly Weather Review*, **136,** 2228-2245.

Jung, Y., M. Xue, G. Zhang, and J. M. Straka, 2008b: Assimilation of Simulated Polarimetric Radar Data for a Convective Storm Using the Ensemble Kalman Filter. Part II: Impact of Polarimetric Data on Storm Analysis. *Monthly Weather Review*, **136,** 2246-2260.

Jung, Y., M. Xue, and G. Zhang, 2010: Simulations of Polarimetric Radar Signatures of a Supercell Storm Using a Two-Moment Bulk Microphysics Scheme. *Journal of Applied Meteorology and Climatology*, **49,** 146-163.

Kawabata, T., H.-S. Bauer, T. Schwitalla, V. Wulfmeyer, and A. Adachi, 2018: Evaluation of Forward Operators for Polarimetric Radars Aiming for Data Assimilation. *Journal of the Meteorological Society of Japan*, **96A,** 157-174.

Kumjian, M. R., and A. V. Ryzhkov, 2008: Polarimetric Signatures in Supercell Thunderstorms. *Journal of Applied Meteorology and Climatology*, **47,** 1940-1961.

Lee, M.-T., P.-L. Lin, W.-Y. Chang, B. K. Seela, and J. Janapati, 2019: Microphysical Characteristics and Types of Precipitation for Different Seasons over North Taiwan. *Journal of the Meteorological Society of Japan*, **97,** 841-865.

Lei, H., J. Guo, D. Chen, and J. Yang, 2020: Systematic Bias in the Prediction of Warm-Rain Hydrometeors in the WDM6 Microphysics Scheme and Modifications. *JGR Atmospherics*, **125,** e2019JD030756.

Li, X., and J. R. Mecikalski, 2010: Assimilation of the dual-polarization Doppler radar data for a convective storm with a warm-rain radar forward operator. *JGR Atmospherics*, **115**.

Li, X., and J. R. Mecikalski, 2012: Impact of the Dual-Polarization Doppler Radar Data on Two Convective Storms with a Warm-Rain Radar Forward Operator. *Monthly Weather Review*, **140,** 2147-2167.

Lim, K.-S. S., and S.-Y. Hong, 2010: Development of an Effective Double-Moment Cloud Microphysics Scheme with Prognostic Cloud Condensation Nuclei (CCN) for Weather and Climate Models. *Monthly Weather Review*, **138,** 1587-1612.

Lin, Y.-L., R. D. Farley, and H. D. Orville, 1983: Bulk Parameterization of the Snow Field in a Cloud Model. *Journal of Applied Meteorology and Climatology*, **22,** 1065-1092.

Marshall, J. S., and W. M. K. Palmer, 1948: The Distribution of Raindrops with Size. *Journal of Atmospheric Sciences*, **5,** 165-166.

Milbrandt, J. A., and M. K. Yau, 2005: A Multimoment Bulk Microphysics Parameterization.

Part I: Analysis of the Role of the Spectral Shape Parameter. *Journal of the Atmospheric Sciences*, **62,** 3051-3064.

Morrison, H., J. A. Curry, and V. I. Khvorostyanov, 2005: A New Double-Moment Microphysics Parameterization for Application in Cloud and Climate Models. Part I: Description. *Journal of the Atmospheric Sciences*, **62,** 1665-1677.

Ott, E., and Coauthors, 2004: A local ensemble Kalman filter for atmospheric data assimilation. *Tellus A*, **56,** 415-428.

Park, H. S., A. V. Ryzhkov, D. S. Zrnić, and K.-E. Kim, 2009: The Hydrometeor Classification Algorithm for the Polarimetric WSR-88D: Description and Application to an MCS. *Weather and Forecasting*, **24,** 730-748.

Parker, M. D., and R. H. Johnson, 2000: Organizational Modes of Midlatitude Mesoscale Convective Systems. *Monthly Weather Review*, **128,** 3413-3436.

Putnam, B., M. Xue, Y. Jung, N. Snook, and G. Zhang, 2019: Ensemble Kalman Filter Assimilation of Polarimetric Radar Observations for the 20 May 2013 Oklahoma Tornadic Supercell Case. *Monthly Weather Review*, **147,** 2511-2533.

Roebber, P. J., 2009: Visualizing Multiple Measures of Forecast Quality. *Weather and Forecasting*, **24,** 601-608.

Rutledge, S. A., and P. Hobbs, 1983: The Mesoscale and Microscale Structure and Organization of Clouds and Precipitation in Midlatitude Cyclones. VIII: A Model for the "Seeder-Feeder" Process in Warm-Frontal Rainbands. *Journal of Atmospheric Sciences*, **40,** 1185-1206.

Ryzhkov, A., and D. Zrnić, 1996: Assessment of Rainfall Measurement That Uses Specific Differential Phase. *Journal of Applied Meteorology and Climatology*, **35,** 2080-2090.

Ryzhkov, A., M. Pinsky, A. Pokrovsky, and A. Khain, 2011: Polarimetric Radar Observation Operator for a Cloud Model with Spectral Microphysics. *Journal of Applied Meteorology and Climatology*, **50,** 873-894.

Snyder, C., and F. Zhang, 2003: Assimilation of Simulated Doppler Radar Observations with an Ensemble Kalman Filter. *Monthly Weather Review*, **131,** 1663-1677.

Steiner, M., R. A. Houze, and S. E. Yuter, 1995: Climatological Characterization of Three-Dimensional Storm Structure from Operational Radar and Rain Gauge Data. *Journal of Applied Meteorology and Climatology*, **34,** 1978-2007.

Sun, J., and N. A. Crook, 1997: Dynamical and Microphysical Retrieval from Doppler Radar Observations Using a Cloud Model and Its Adjoint. Part I: Model Development and Simulated Data Experiments. *Journal of the Atmospheric Sciences*, **54,** 1642-1661.

Tao, W.-K., J. Simpson, and M. McCumber, 1989: An Ice-Water Saturation Adjustment. *Monthly Weather Review*, **117,** 231-235.

Tao, W. K., and Coauthors, 2003: Microphysics, radiation and surface processes in the Goddard Cumulus Ensemble (GCE) model. *Meteorol Atmos Phys*, **82,** 97-137.

Tsai, C.-C., S.-C. Yang, and Y.-C. Liou, 2014: Improving quantitative precipitation nowcasting with a local ensemble transform Kalman filter radar data assimilation system: observing system simulation experiments. *Tellus A*, **66,** 21804.

Tsai, C.-C., and K.-S. Chung, 2020: Sensitivities of Quantitative Precipitation Forecasts for Typhoon Soudelor (2015) near Landfall to Polarimetric Radar Data Assimilation. *Remote Sensing*, **12,** 3711.

Ulbrich, C. W., 1983: Natural Variations in the Analytical Form of the Raindrop Size Distribution. *Journal of Applied Meteorology and Climatology*, **22,** 1764-1775.

Wu, B., J. Verlinde, and J. Sun, 2000: Dynamical and Microphysical Retrievals from Doppler Radar Observations of a Deep Convective Cloud. *Journal of the Atmospheric Sciences*, **57,** 262-283.

Xiao, Q., Y.-H. Kuo, J. Sun, W.-C. Lee, E. Lim, Y.-R. Guo, and D. M. Barker, 2005: Assimilation of Doppler Radar Observations with a Regional 3DVAR System: Impact of Doppler Velocities on Forecasts of a Heavy Rainfall Case. *Journal of Applied Meteorology and Climatology*, **44,** 768-788.

You, C.-R., K.-S. Chung, and C.-C. Tsai, 2020: Evaluating the Performance of a Convection-Permitting Model by Using Dual-Polarimetric Radar Parameters: Case Study of SoWMEX IOP8. *Remote Sensing*, **12,** 3004.

Zhang, F., C. Snyder, and J. Sun, 2004: Impacts of Initial Estimate and Observation Availability on Convective-Scale Data Assimilation with an Ensemble Kalman Filter. *Monthly Weather Review*, **132,** 1238-1253.

Zhang, G., J. Vivekanandan, and E. Brandes, 2001: A method for estimating rain rate and drop size distribution from polarimetric radar measurements. *IEEE Transactions on Geoscience and Remote Sensing*, **39,** 830-841.

Zhu, K., M. Xue, K. Ouyang, and Y. Jung, 2020: Assimilating polarimetric radar data with an ensemble Kalman filter: OSSEs with a tornadic supercell storm simulated with a two-moment microphysics scheme. *Royal Metorological Society*, **146,** 1880-1900.

邵彥銘，2015：利用局地系集轉換卡爾曼濾波器雷達資料同化系統改善短期定量降雨預報：SoWMEX IOP8 個案分析，碩士論文，國立中央大學大氣物理研究所，95 頁

梁晏彰，2019：分析不同微物理參數化之系集預報誤差: SoWMEX-IOP8 對流個案，碩士論文，國立中央大學大氣物理研究所，110 頁

游承融，2019：利用雙偏極化雷達觀測資料進行極短期天氣預報評估─2008 年西南氣流實驗 IOP8 期間颮線系統個案，碩士論文，國立中央大學大物理研究所，105 頁

盧可昕，2018：利用雙偏極化雷達及雨滴譜儀觀測資料分析 2008 年西南氣流實驗期間強降雨事件的雲物理過程，碩士論文，國立中央大學大物理研究所，105 頁

Tables

Table 1 Localization radius and inflation factor set in the WLRAS

	U、V	W	PH、T	Qv、Qc、Qi、Nc、Ni	Qr、Qs、Qg、Nr、Ns、Ng
Horizontal localization radius (km)	36	12	12	24	12
Vertical localization radius (km)	4				
Inflation	1.08				

Table 2 All the experiments conducted in this study

Original WLRAS (scheme: GCE, WSM6, WDM6, MOR)						
	V_r	Z_H	Z_{DR}	K_{DP}		
Scheme_VrZ	V	V				
Scheme_VrZZdr	V	V	V			
Scheme_VrZKdp	V	V		V		
Scheme_VrZZK	V	V	V	V		
New Approach (scheme: WDM6, MOR)						
	V_r	Z_H	Z_{DR}	K_{DP}	Update N_w	Update D_m
Shceme_VrZZdr_NwDm	V	V	V		V	V
Scheme_VrZZK_NwDm	V	V	V	V	V	V

Table 3 Setting for rain, snow graupel in four MP schemes.

	Prognostic mixing ratio	Prognostic total nmber concentration	Intercept parameter (m^{-4})	Shape parameter	Hydrometeor density (kg/m^{-3})
GCE	q_r, q_s,q_g		N_{0r} = 8E6 N_{0s} = 1.6E7 N_{0g} = 4E6	$\mu_r = 0$ $\mu_s = 0$ $\mu_g = 0$	$\rho_r = 1000$ $\rho_s = 100$ $\rho_g = 400$
WSM6			N_{0r} = 8E6 N_{0s} = 2E6 N_{0g} = 4E6	$\mu_r = 0$ $\mu_s = 0$ $\mu_g = 0$	$\rho_r = 1000$ $\rho_s = 100$ $\rho_g = 500$
WDM6		N_{Tr}	N_{0s} = 2E6 N_{0g} = 4E6	$\mu_r = 1$ $\mu_s = 0$ $\mu_g = 0$	$\rho_r = 1000$ $\rho_s = 100$ $\rho_g = 500$
MOR		N_{Tr}, N_{Ts}, N_{Tg},		$\mu_r = 0$ $\mu_s = 0$ $\mu_g = 0$	$\rho_r = 997$ $\rho_s = 100$ $\rho_g = 400$

Table 4 Power law fitting coefficient of scattering amplitude.

	$\alpha_{a,x}$	$\alpha_{b,x}$	$\alpha_{k,x}$	$\beta_{a,x}$	$\beta_{b,x}$	$\beta_{k,x}$
Rain	4.28E-4	4.28E-4	1.3E-5	3.04	2.77	4.63
Snow	0.194E-4	0.191E-4	0.3E-6	3.0	3.0	3.0
Graupel	8.1E-5	7.6 E-5	0.5E-5	3.0	3.0	3.0
Wet snow	(1)	(2)	$\alpha_{a,rs} - \alpha_{b,rs}$	3.0	3.0	3.0
Wet graupel	(3)	(4)	$\alpha_{a,rg} - \alpha_{b,rg}$	3.0	3.0	3.0

(1) $\alpha_{a,rs} = (0.194 + 7.094f_w + 2.135f_w^2 - 5.225f_w^3) \times 10^{-4}$

(2) $\alpha_{b,rs} = (0.191 + 6.916f_w + 2.841f_w^2 - 1.160f_w^3) \times 10^{-4}$

(3) $\alpha_{a,rg} = (0.191 + 2.39f_w - 12.57f_w^2 + 38.71f_w^3 - 65.53f_w^4 + 56.16f_w^5 - 18.98f_w^6) \times 10^{-3}$

(4) $\alpha_{b,rg} = (0.165 + 1.72f_w - 9.92f_w^2 + 32.15f_w^3 - 56.0f_w^4 + 48.83f_w^5 - 16.69f_w^6) \times 10^{-3}$

f_w is the water fraction in the mixture form.

Table 5 Setting of hydrometeor canting angle.

	Mean canting angle	Standard deviation of canting angle
Rain	0°	0°
Snow / Wet snow	0°	20°
Graupel	0°	60°
Wet graupel	0°	60°(1-cf_w) c = 0.8 if $q_{rg} \geq 0.2$ g/kg; c = 4q_{rg} if q_{rg} <0.2 g/kg

Table 6 Range and interval for CFADs

	Range	Interval
Z_H	From 0.0 dBZ to 70.0 dBZ	2.5 dBZ
Z_{DR}	Form 0.0 dB to 5.5 dB	0.25 dB
K_{DP}	From 0.0 deg/km to 4.0 deg/km	0.04 deg/km

Table 7 contingency table

	Observation yes	Observation no
Forecast yes	Hit	False Alarm
Forecast no	Miss	Correct Negative

Figures

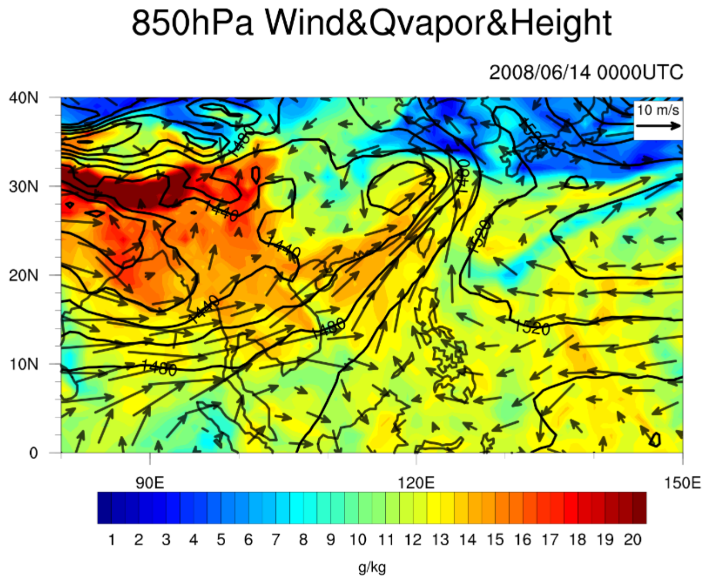

Figure 1 Wind field, water vapor mixing ratio (shaded) and geopotential height (contour) of NCEP analysis at 850 hPa at 0000 UTC 14th June 2008.

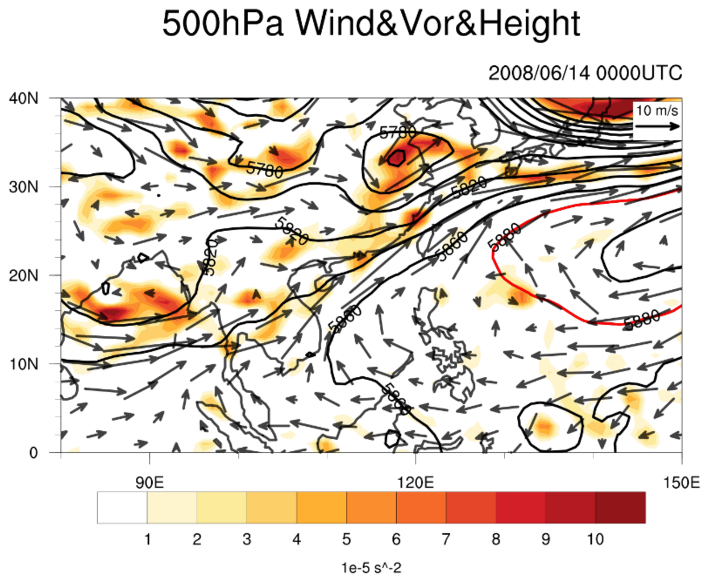

Figure 2 Wind field, relative vorticity (shaded) and geopotential height (contour) of NCEP analysis at 500 hPa at 0000 UTC 14th June 2008. Red contour is 5880-meter geopotential height.

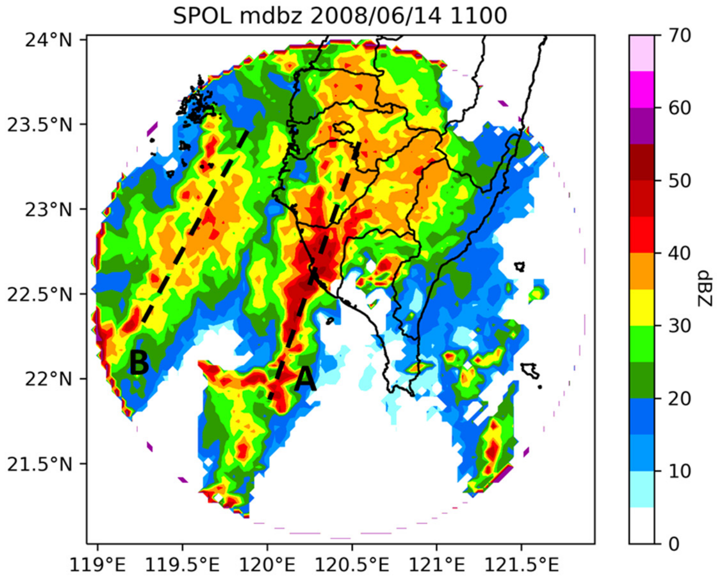

Figure 3 Max Z_H composite observed by SPOL at 1100 UTC 14th June 2008.

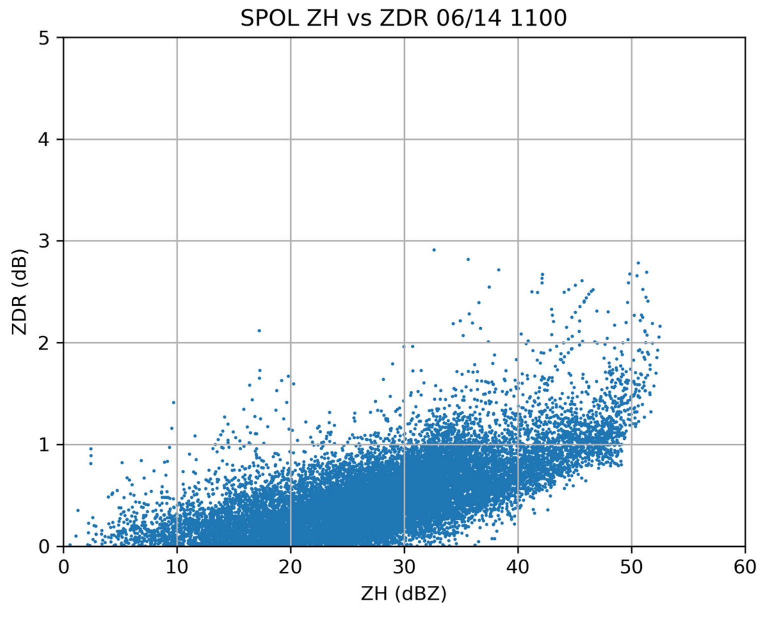

Figure 4 Scatter plot of Z_H and Z_{DR} observed by SPOL below 4-km height at 1100 UTC 14th June 2008.

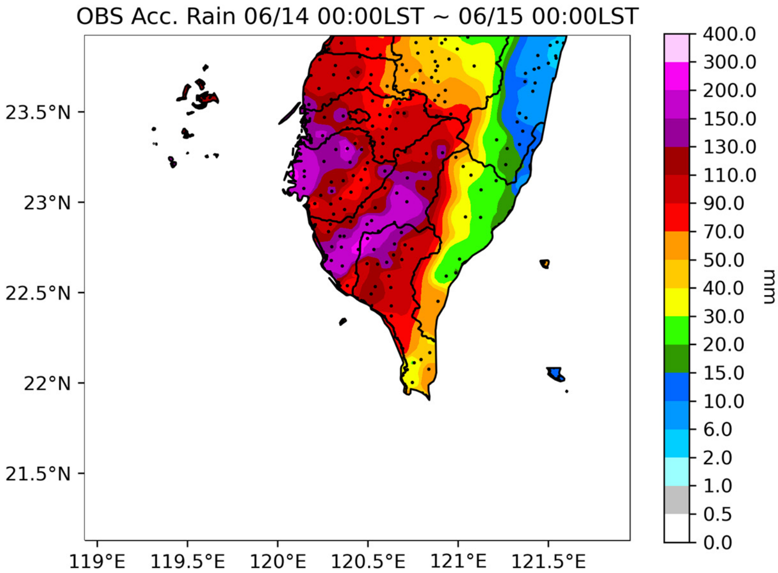

Figure 5 Accumulated rainfall from 0000LST 14th June 2008 to 0000LST 15th June 2008. Black dots show the location of CWB observation sites.

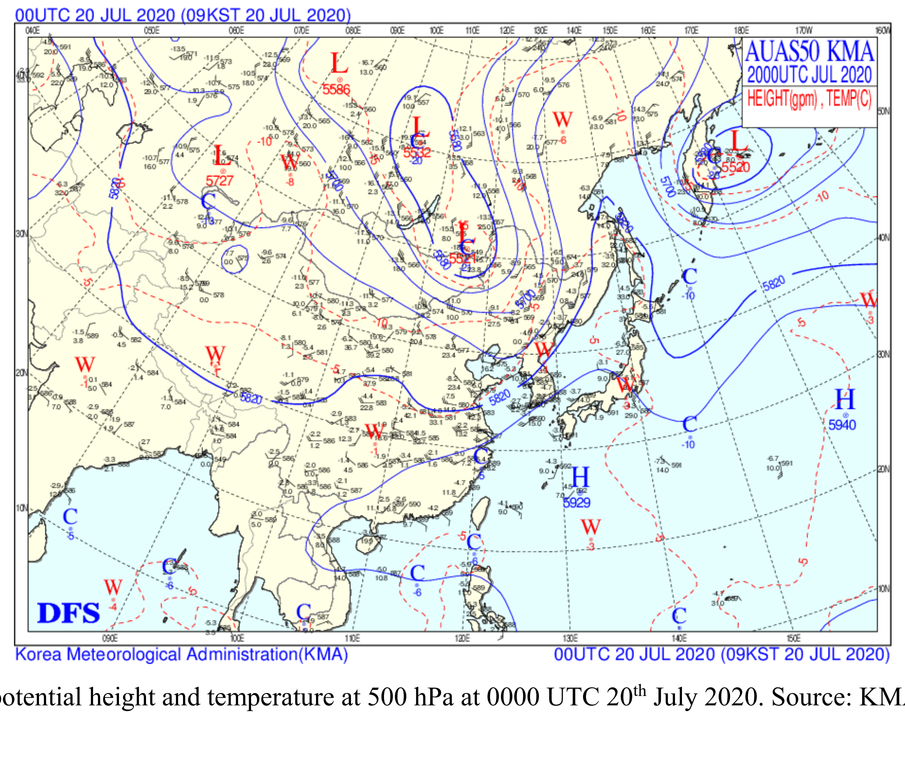

Figure 6 Geopotential height and temperature at 500 hPa at 0000 UTC 20th July 2020. Source: KMA.

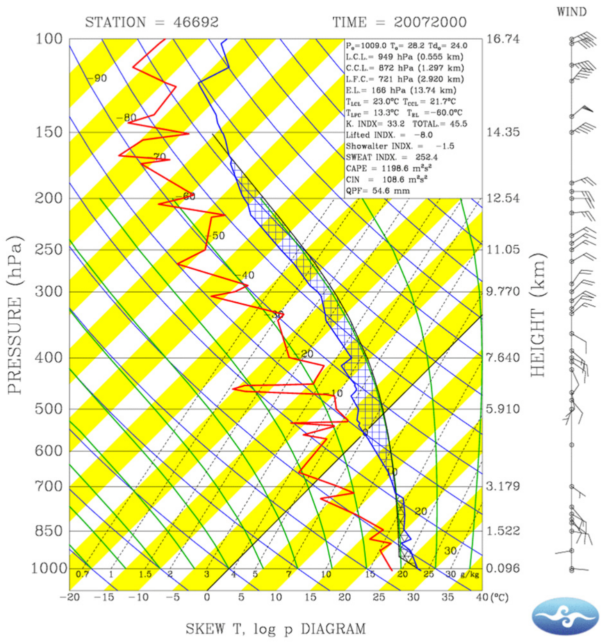

Figure 7 Sounding data at Banqiao station at 0000 UTC 20th July 2020. Source: CWB.

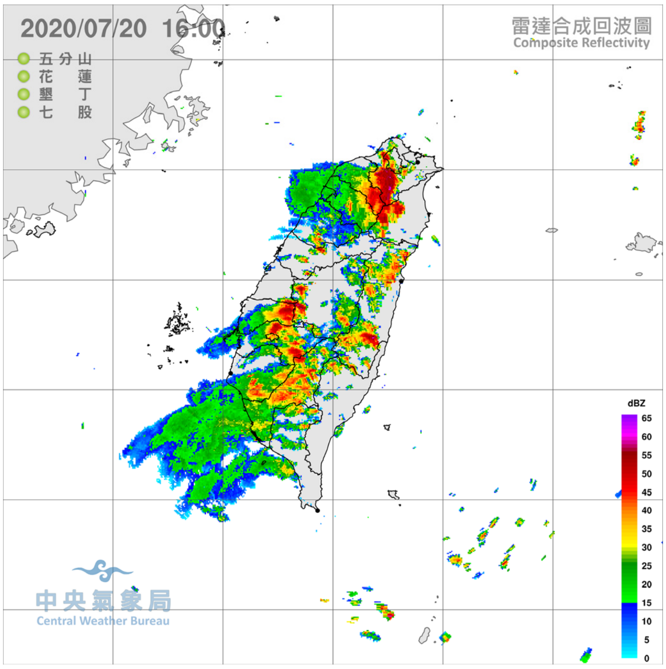

Figure 8 Max Z_H composite from CWB at 1600 LST 20th July 2020. Source: CWB.

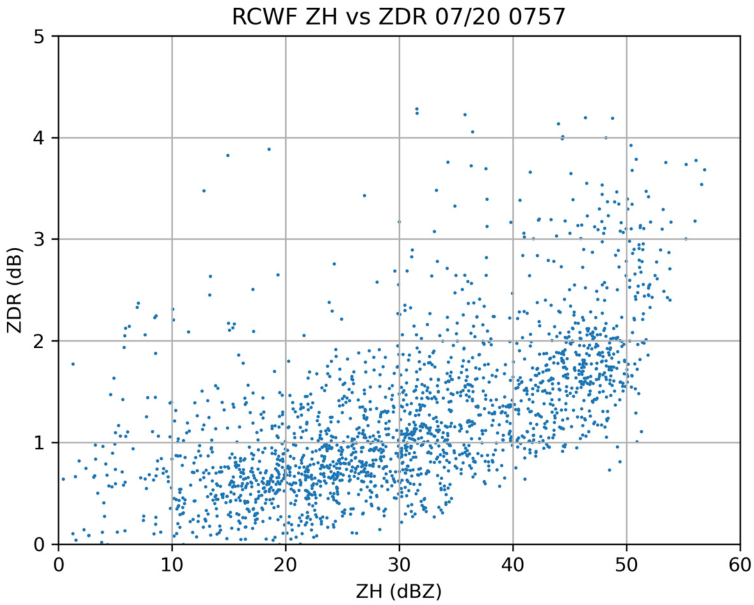

Figure 9 Scatter plot of Z_H and Z_{DR} observed by RCWF below 4-km height at 0757 UTC 20th July 2020.

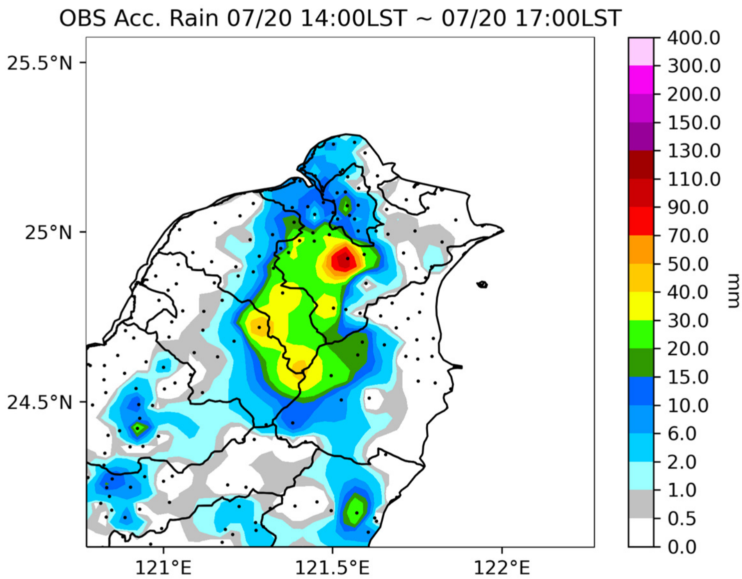

Figure 10 Accumulated rainfall from 1400 LST to 1700 LST on 20th July 2020. Black dots show the location of CWB observation sites.

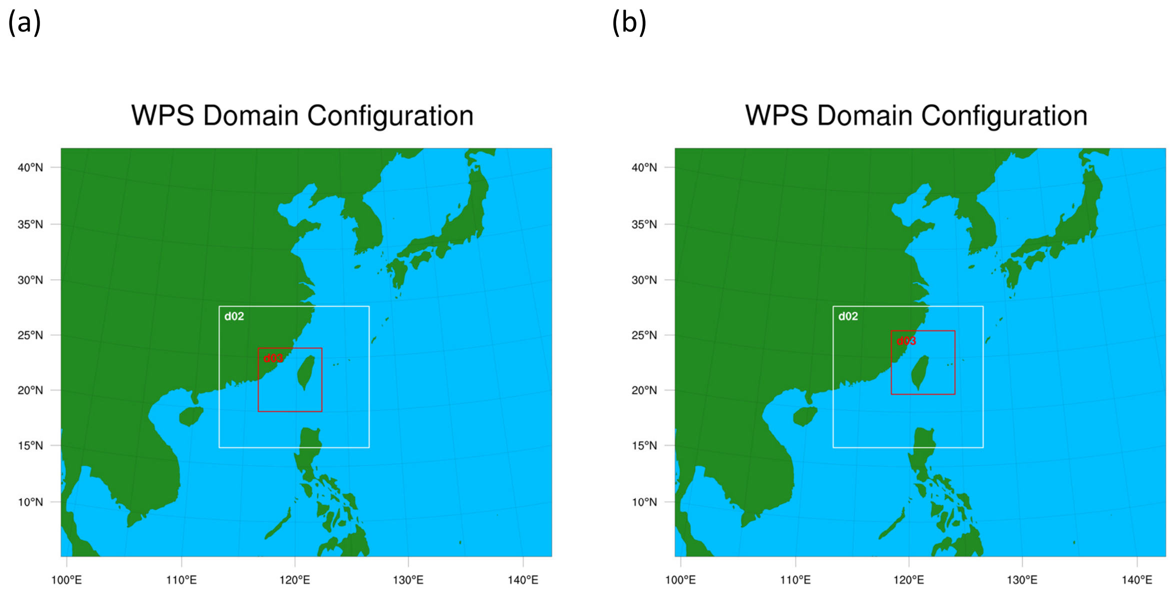

Figure 11 Setting of nested domain. (a)The squall line case (b) The afternoon thunderstorm case.

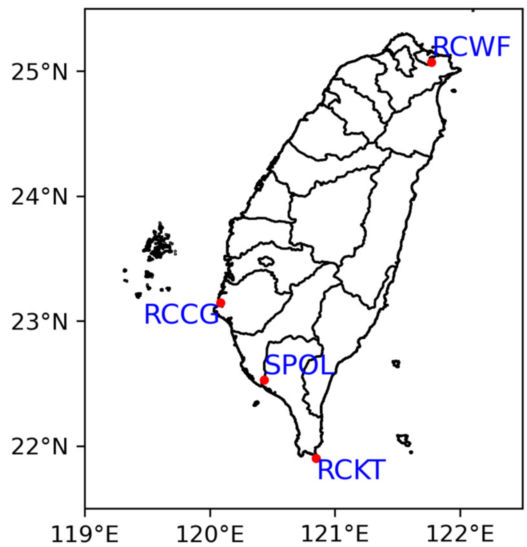

Figure 12 Location of RCWF, RCCG, RCKT and SPOL.

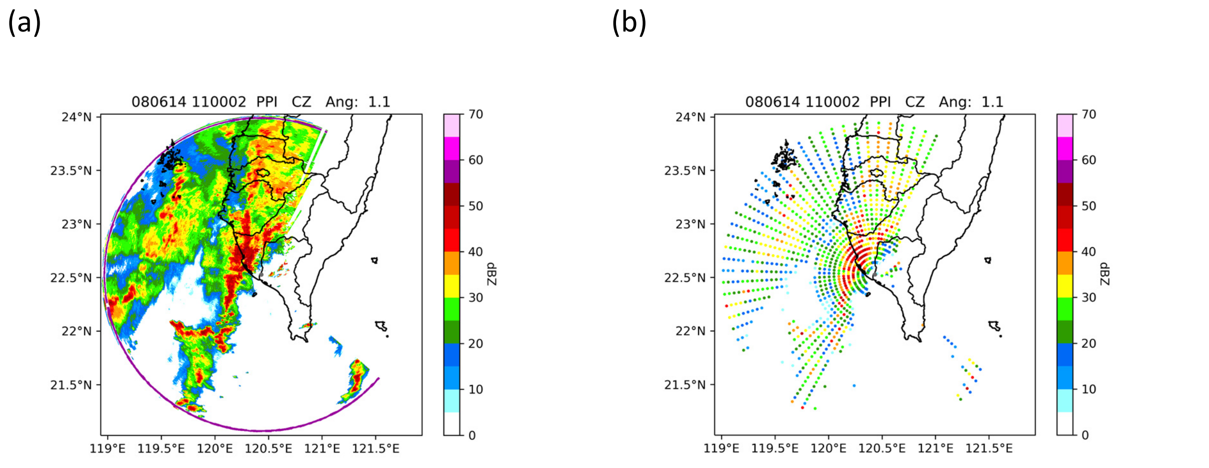

Figure 13 SPOL observation at 1.1° elevation angle at 1100 UTC 14th June 2008. (a) Before superobbing. (b) After superobbing.

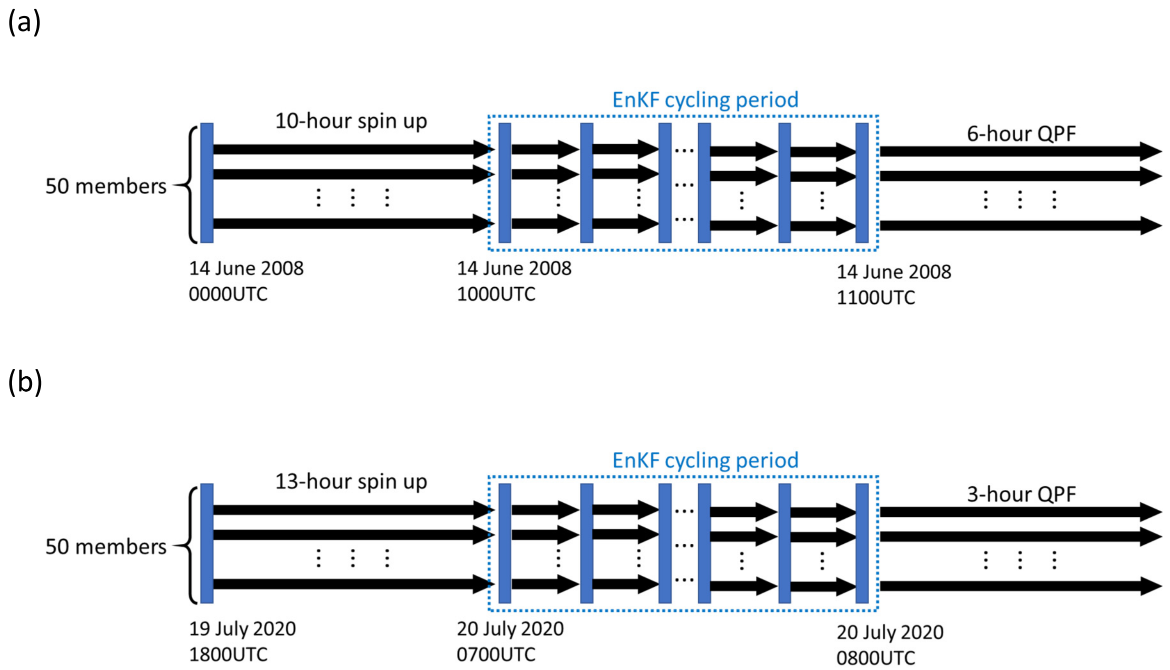

Figure 14 Assimilation flow chart. (a) The squall line case. (b) The afternoon thunderstorm case.

(a)

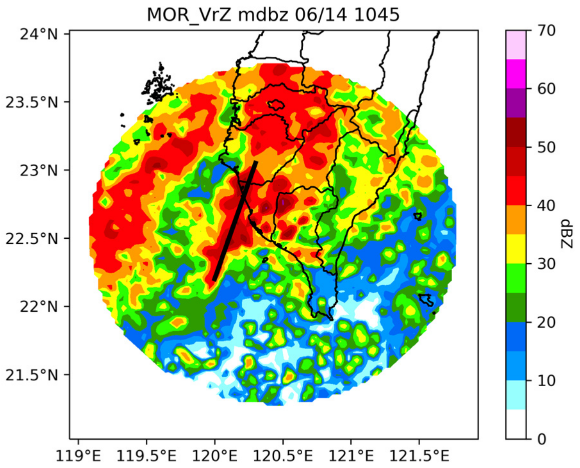

(b)

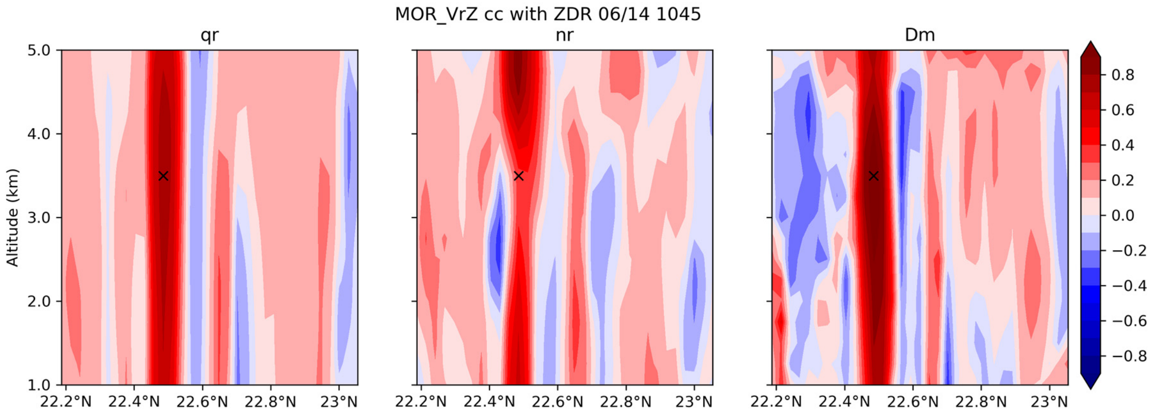

Figure 15 (a) Max Z_H composite with the black line indicating the location of the cross section. (b) Vertical cross section of the correlation coefficient between hydrometeor variables and Z_{DR} at the black cross in MOR_VrZ at 1045 UTC 14th June 2008.

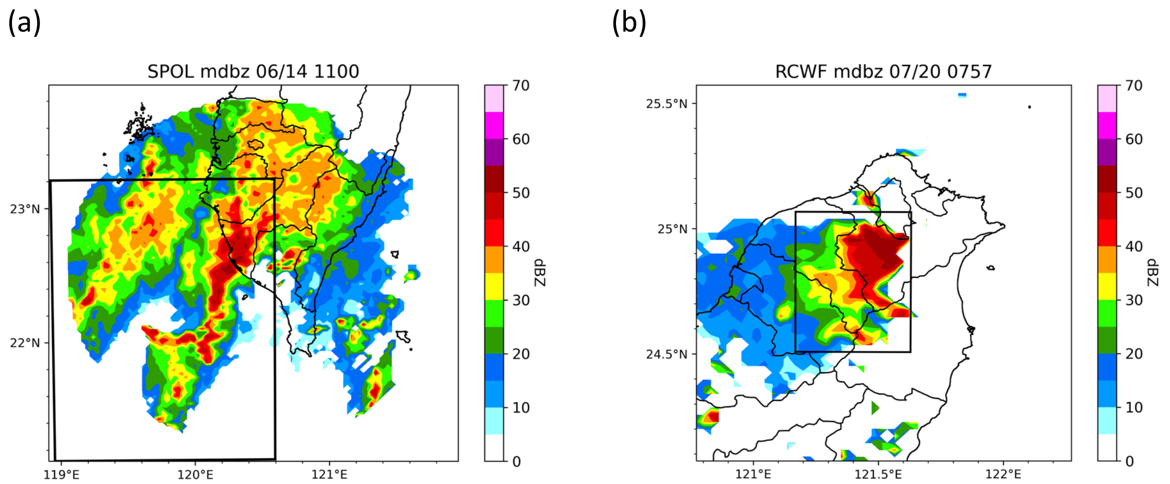

Figure 16 The data in the black rectangle is used to plot CFADs (a) The squall line case (b) The afternoon thunderstorm case.

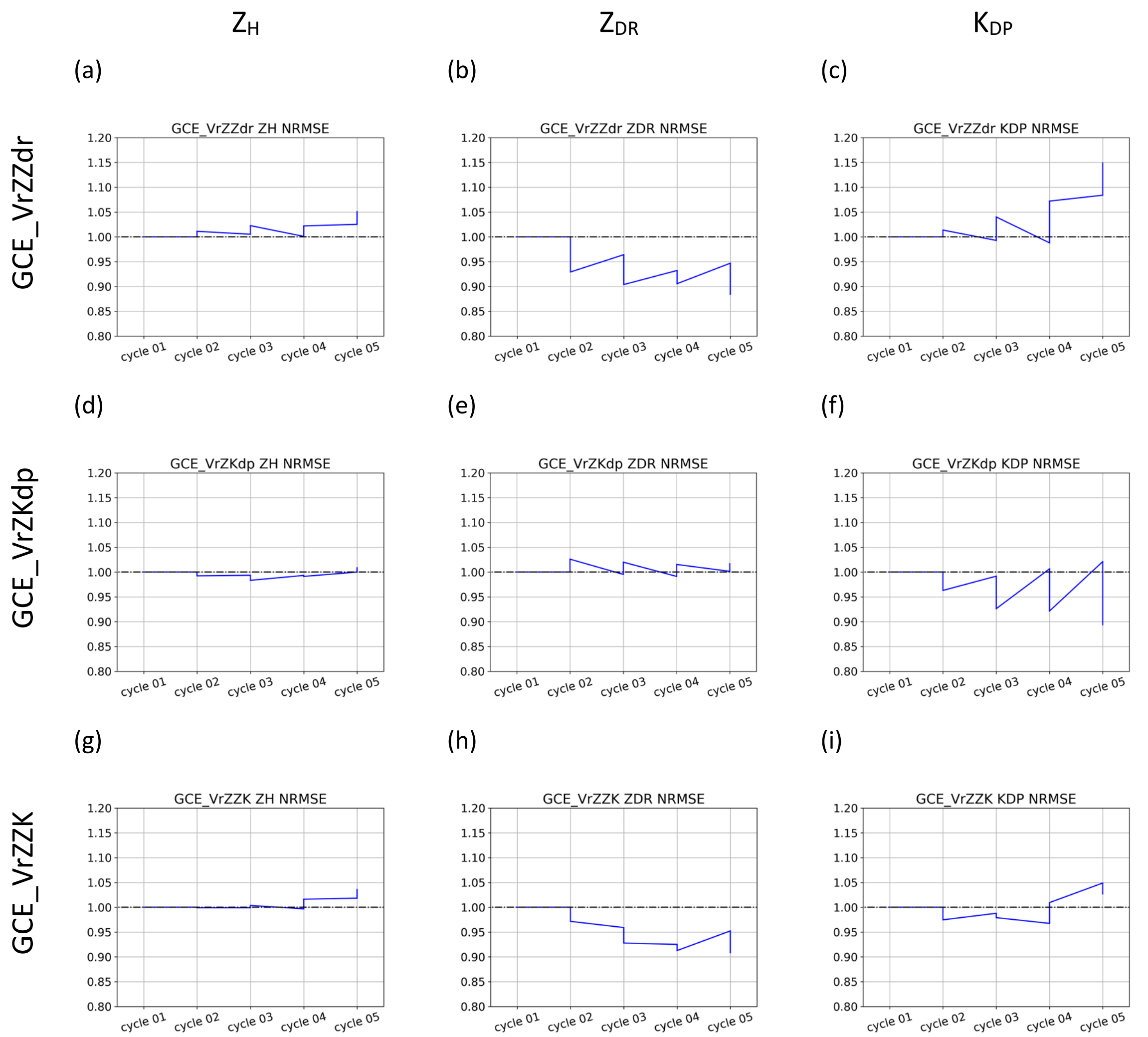

Figure 17 NRMSE of polarimetric parameters in the experiments with GCE scheme in the squall line case from 1000 UTC to 1100 UTC on 14th June 2008.

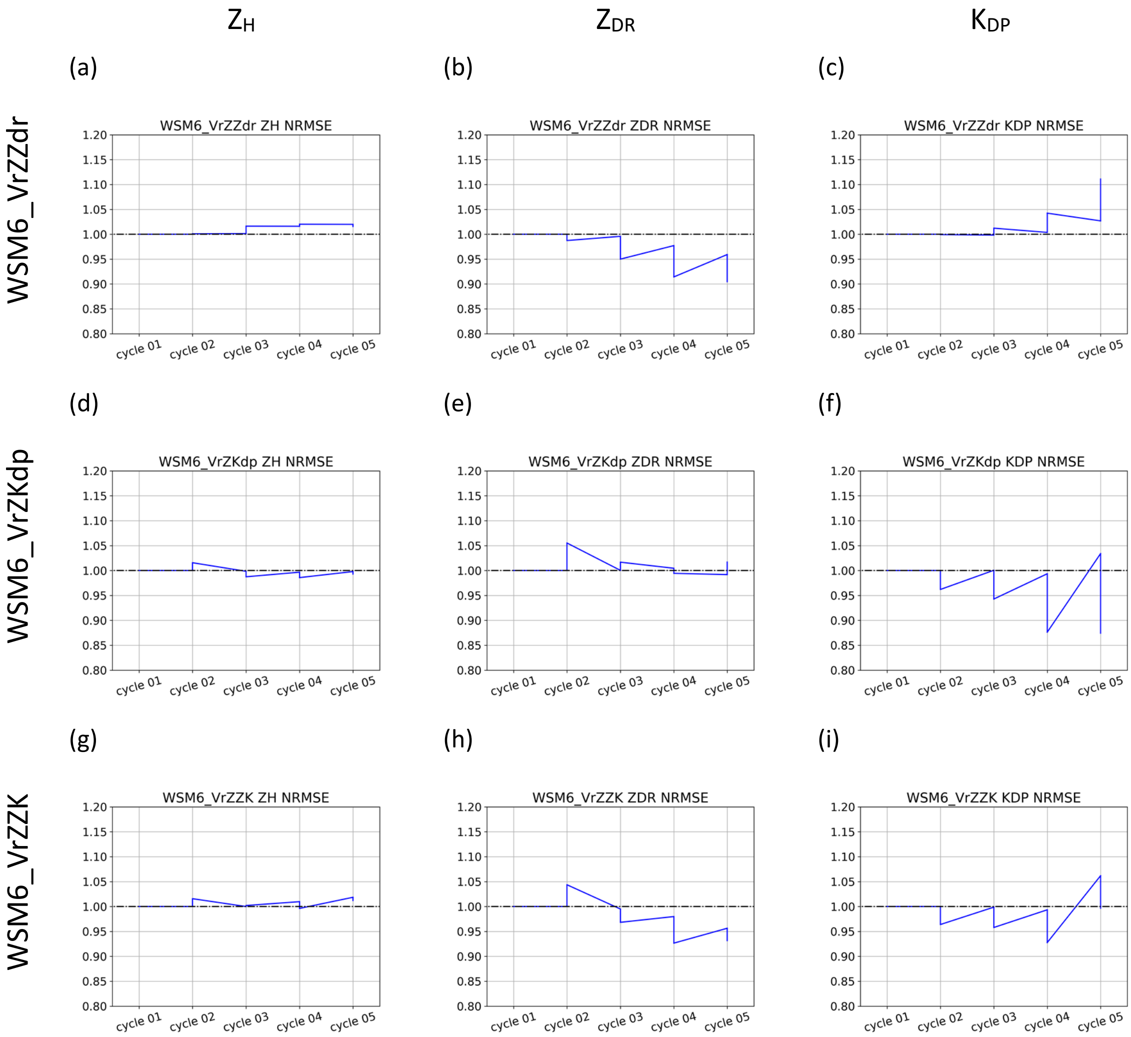

Figure 18 NRMSE of polarimetric parameters in the experiments with WSM6 scheme in the squall line case from 1000 UTC to 1100 UTC on 14th June 2008.

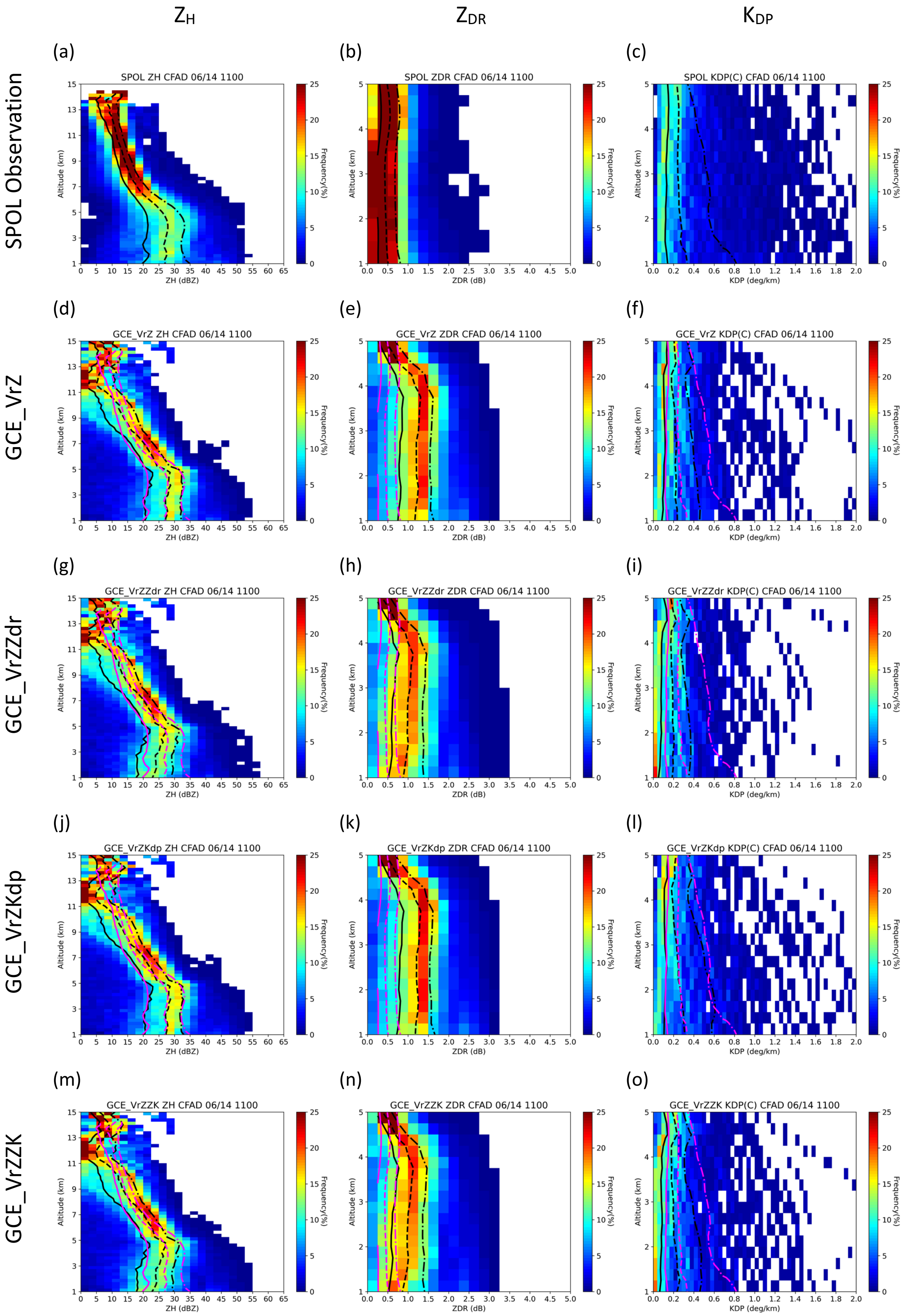

Figure 19 Polarimetric parameter CFADs of SPOL observation and the experiments with GCE scheme in the squall line case at 1100 UTC 14th June 2008. The pink lines are the accumulated 25%, 50% and 75% of SPOL observation.

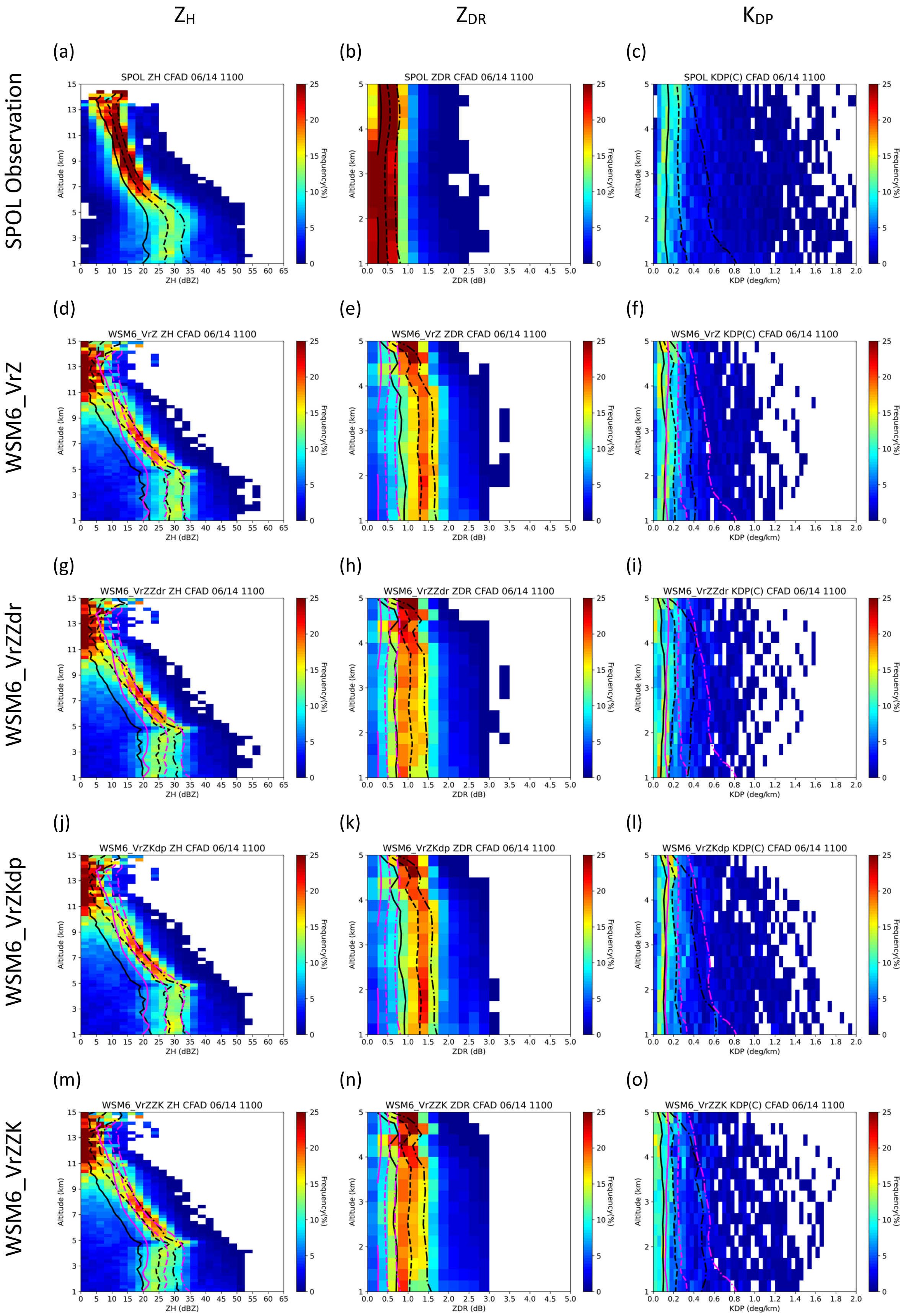

Figure 20 Polarimetric parameter CFADs of SPOL observation and the experiments withWSM6 scheme in the squall line case at 1100 UTC 14th June 2008. The pink lines are the accumulated 25%, 50% and 75% of SPOL observation.

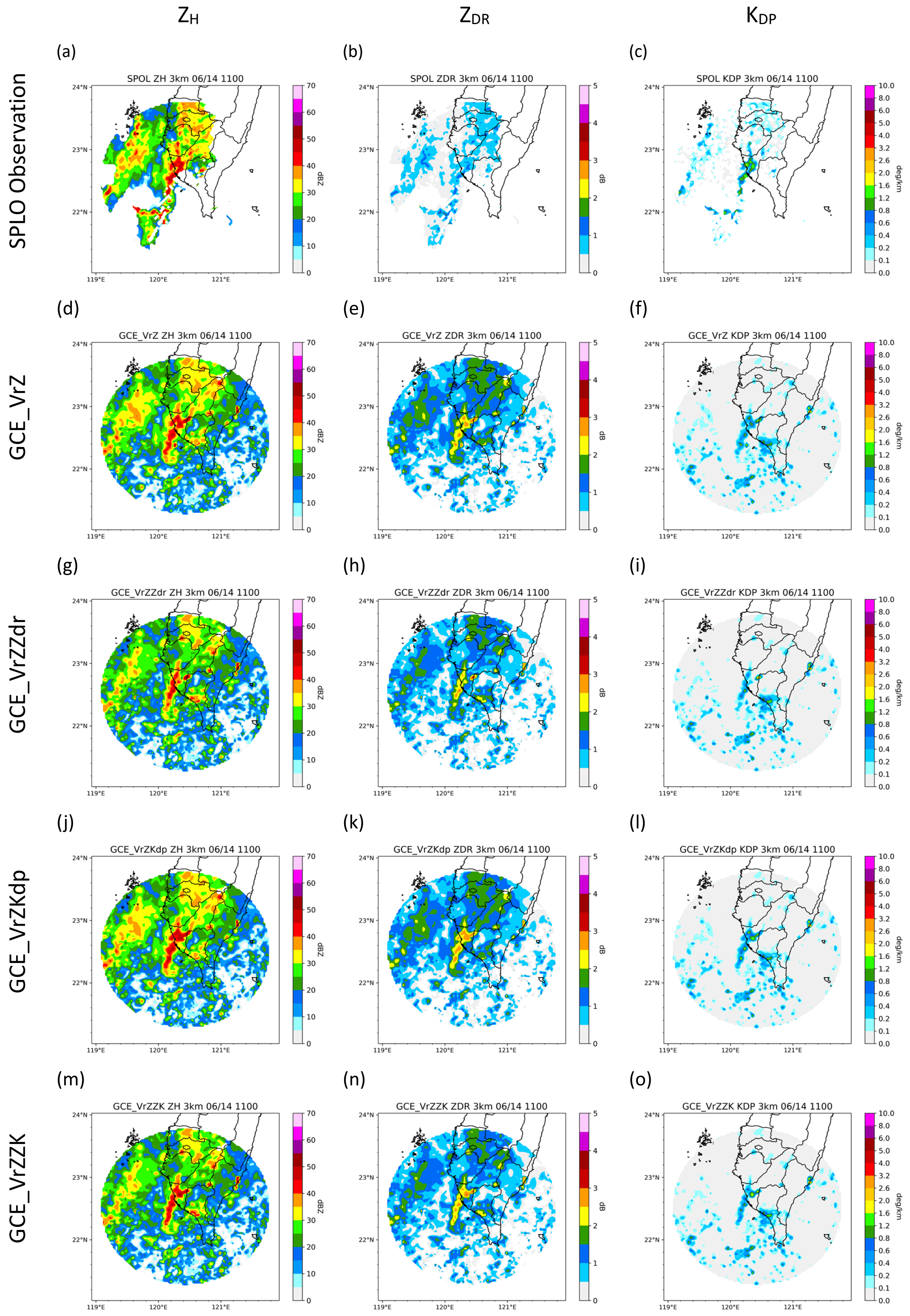

Figure 21 Polarimetric parameters at 3-km height of SPOL observation and the experiments with GCE scheme in the squall line case at 1100 UTC 14th June 2008.

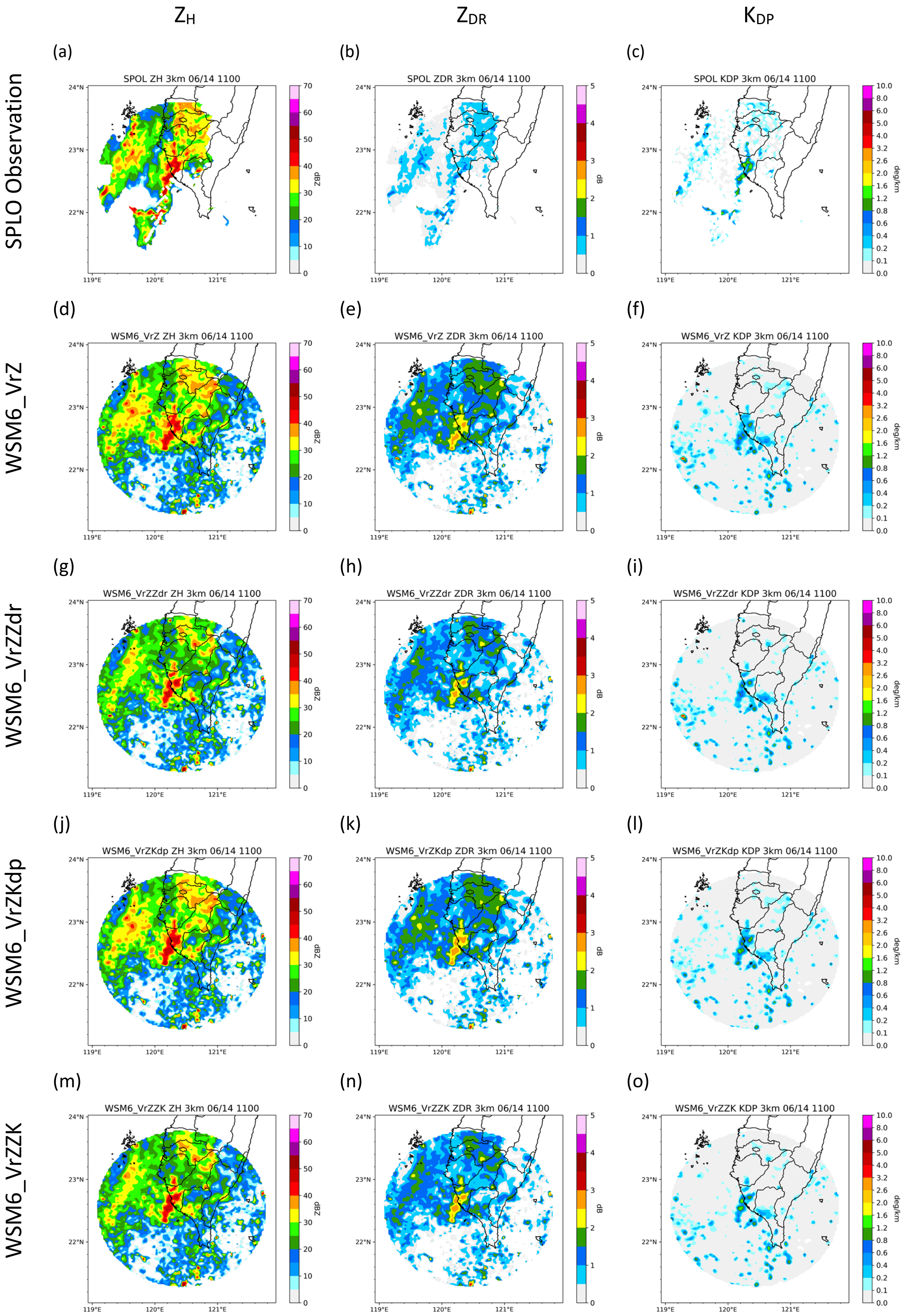

Figure 22 Polarimetric parameter at 3-km height of SPOL observation and the experiments with WSM6 scheme in the squall line case at 1100 UTC 14th June 2008.

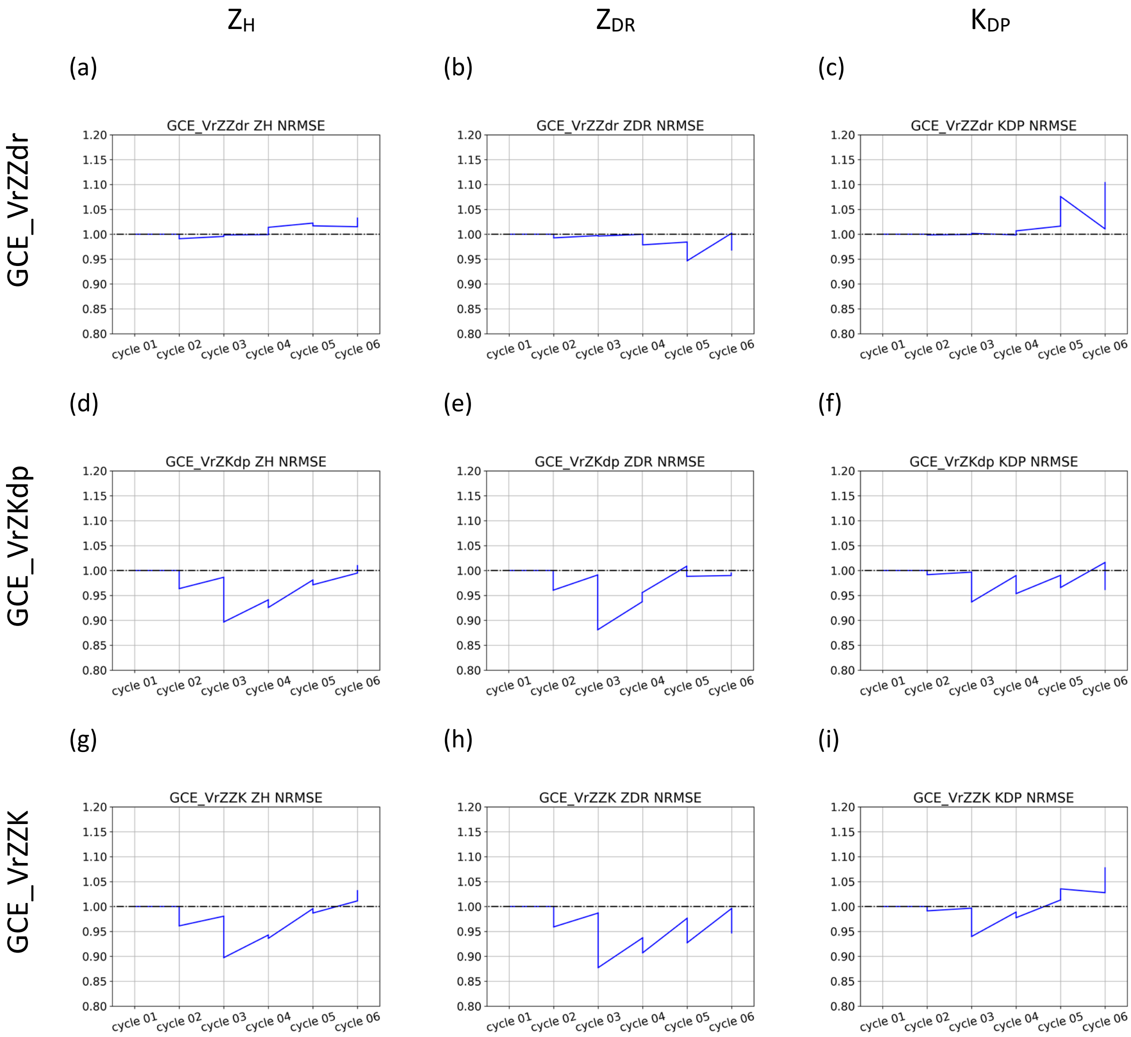

Figure 23 NRMSE of polarimetric parameters in the experiments with GCE scheme in the afternoon thunderstorm case from 0700 UTC to 0800 UTC on 20th July 2020.

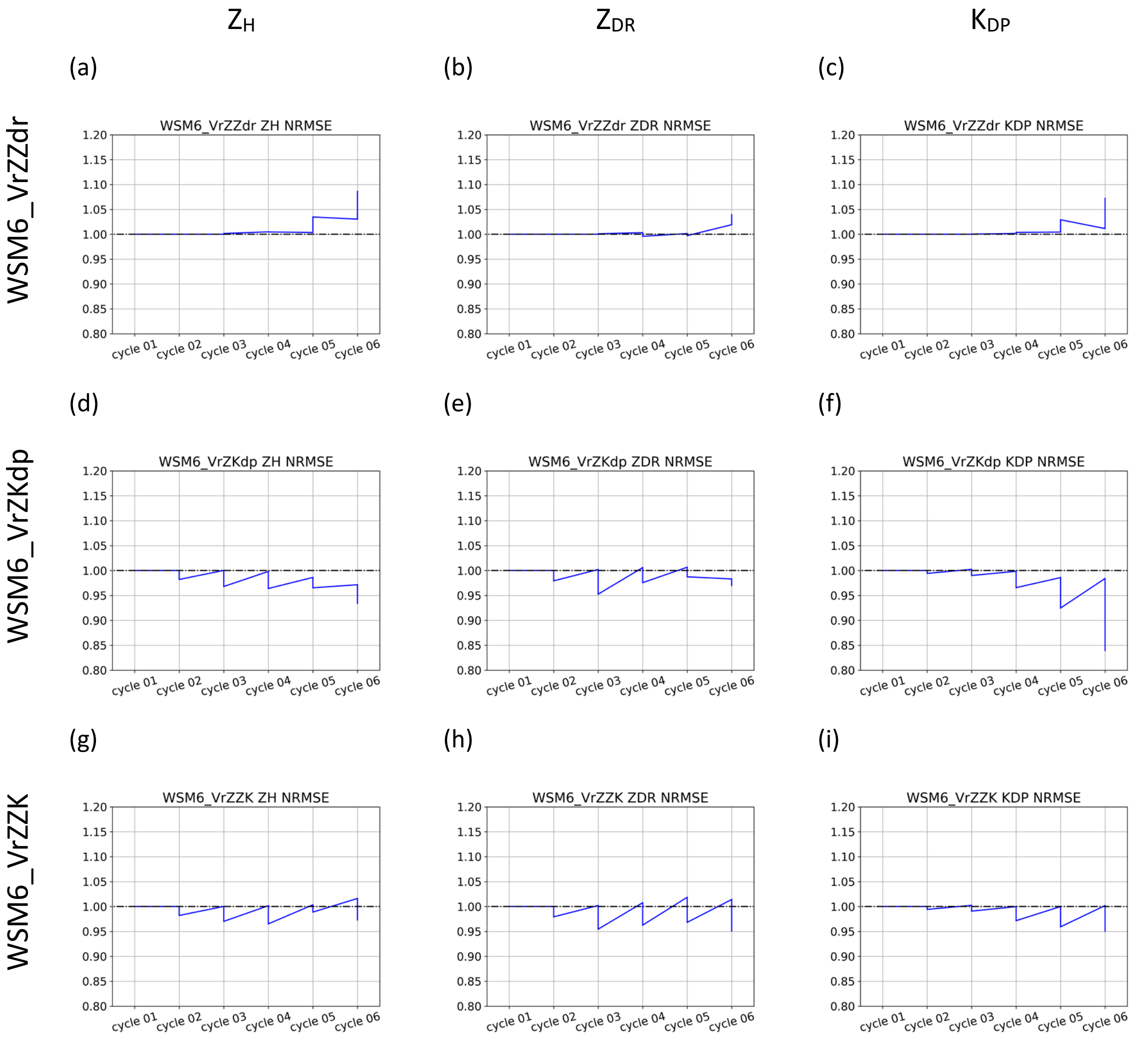

Figure 24 NRMSE of polarimetric parameters in the experiments with WSM6 scheme in the afternoon thunderstorm case from 0700 UTC to 0800 UTC on 20th July 2020.

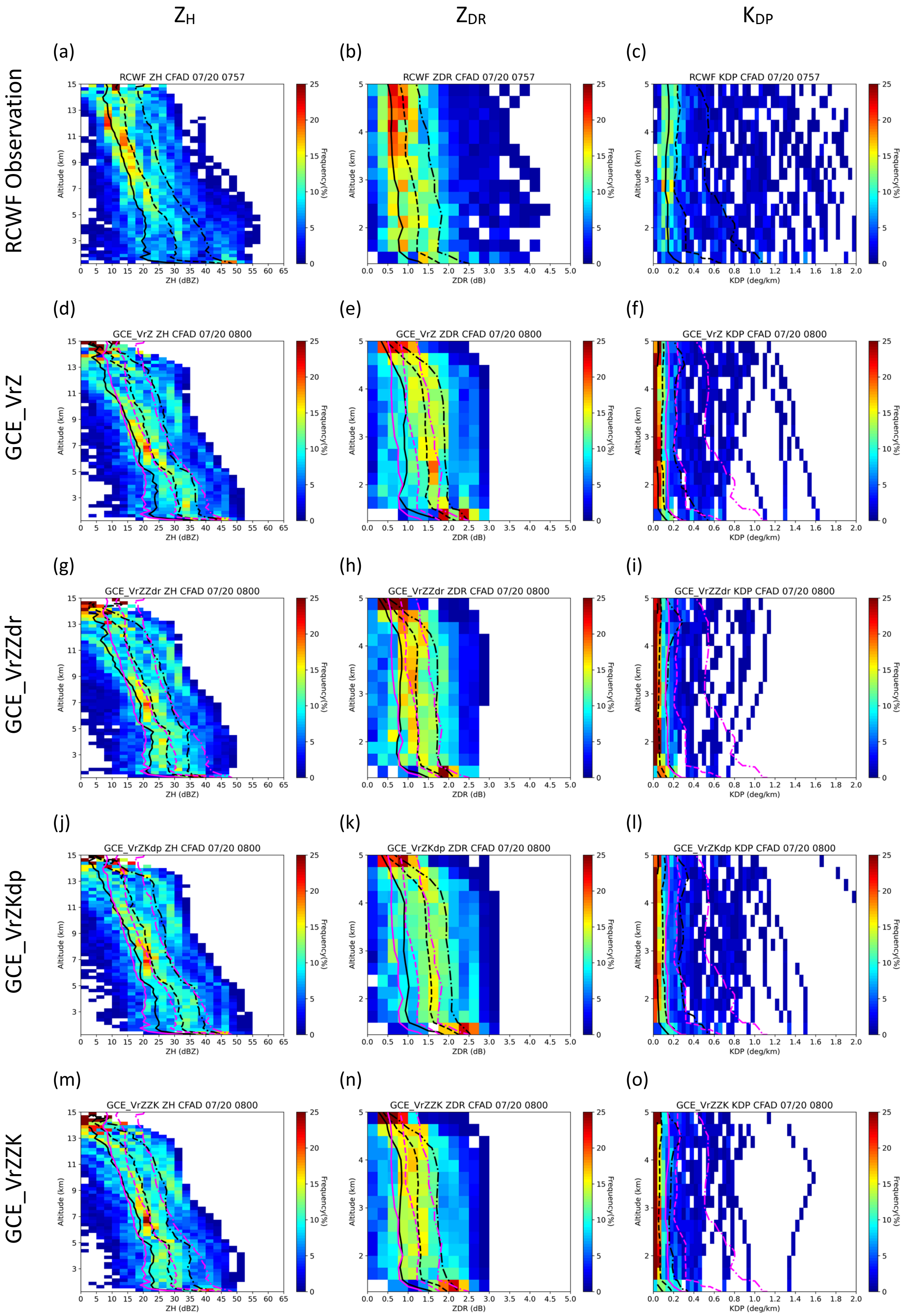

Figure 25 Polarimetric parameter CFADs of RCWF observation and the experiments with GCE scheme in the afternoon thunderstorm case at 0800 UTC 20th July 2020. The pink lines are the accumulated 25%, 50% and 75% of RCWF observation.

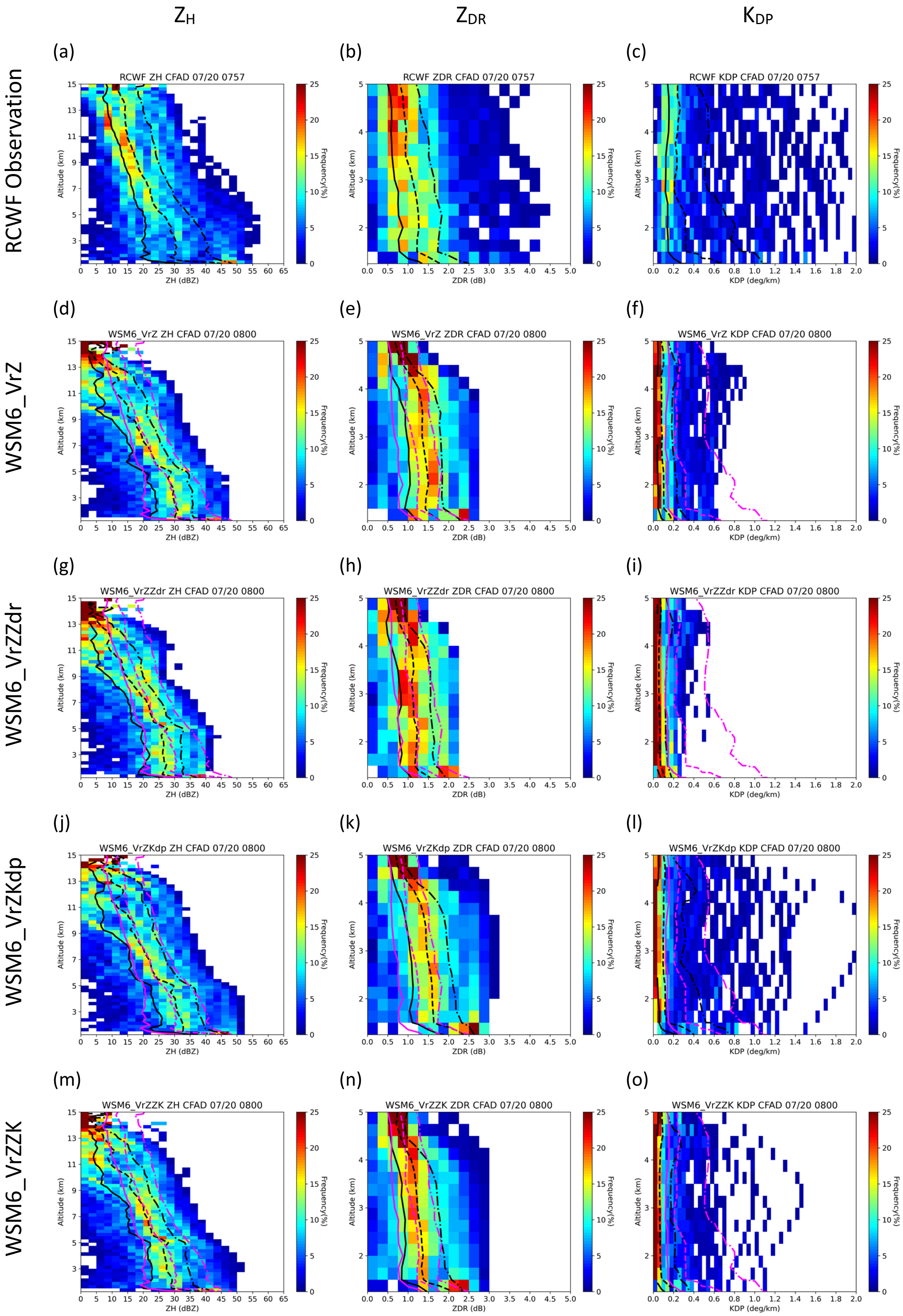

Figure 26 Polarimetric parameter CFADs of RCWF observation and the experiments with WSM6 scheme in the afternoon thunderstorm case at 0800 UTC 20th July 2020. The pink lines are the accumulated 25%, 50% and 75% of RCWF observation.

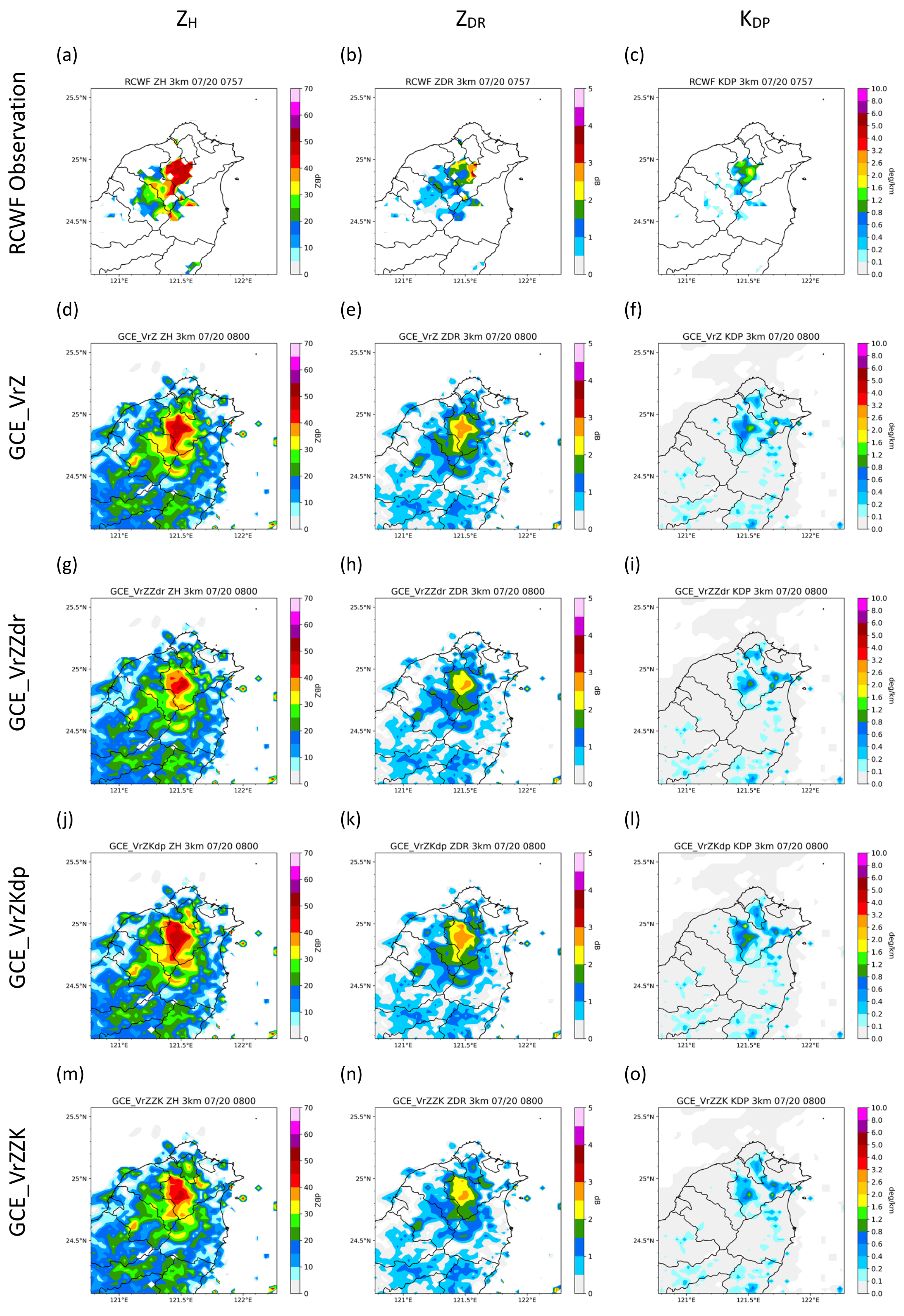

Figure 27 Polarimetric parameter at 3-km height of RCWF observation and the experiments with GCE scheme in the afternoon thunderstorm case at 0800 UTC 20th July 2020.

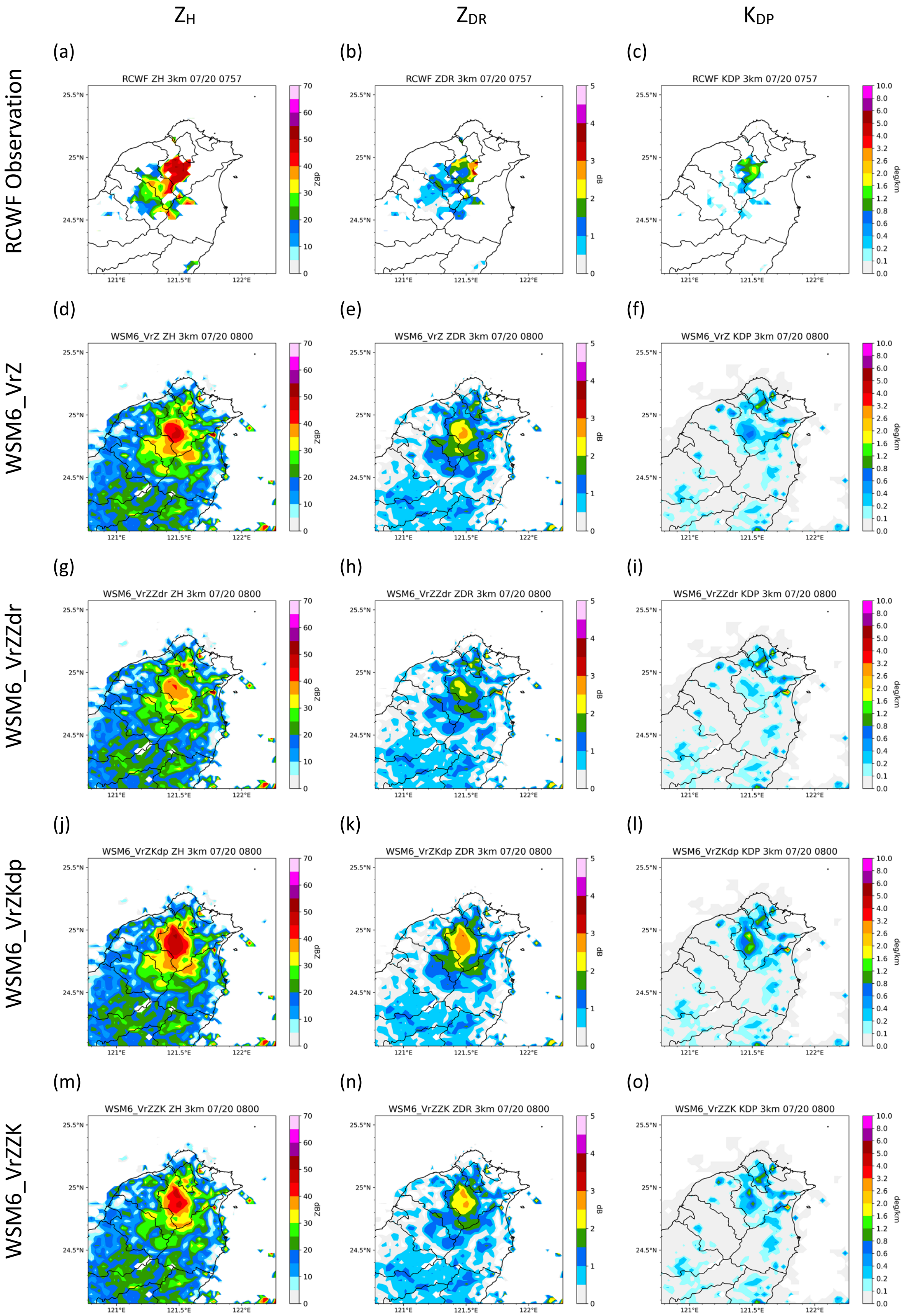

Figure 28 Polarimetric parameter at 3-km height of RCWF observation and the experiments with WSM6 scheme in the afternoon thunderstorm case at 0800 UTC 20th July 2020.

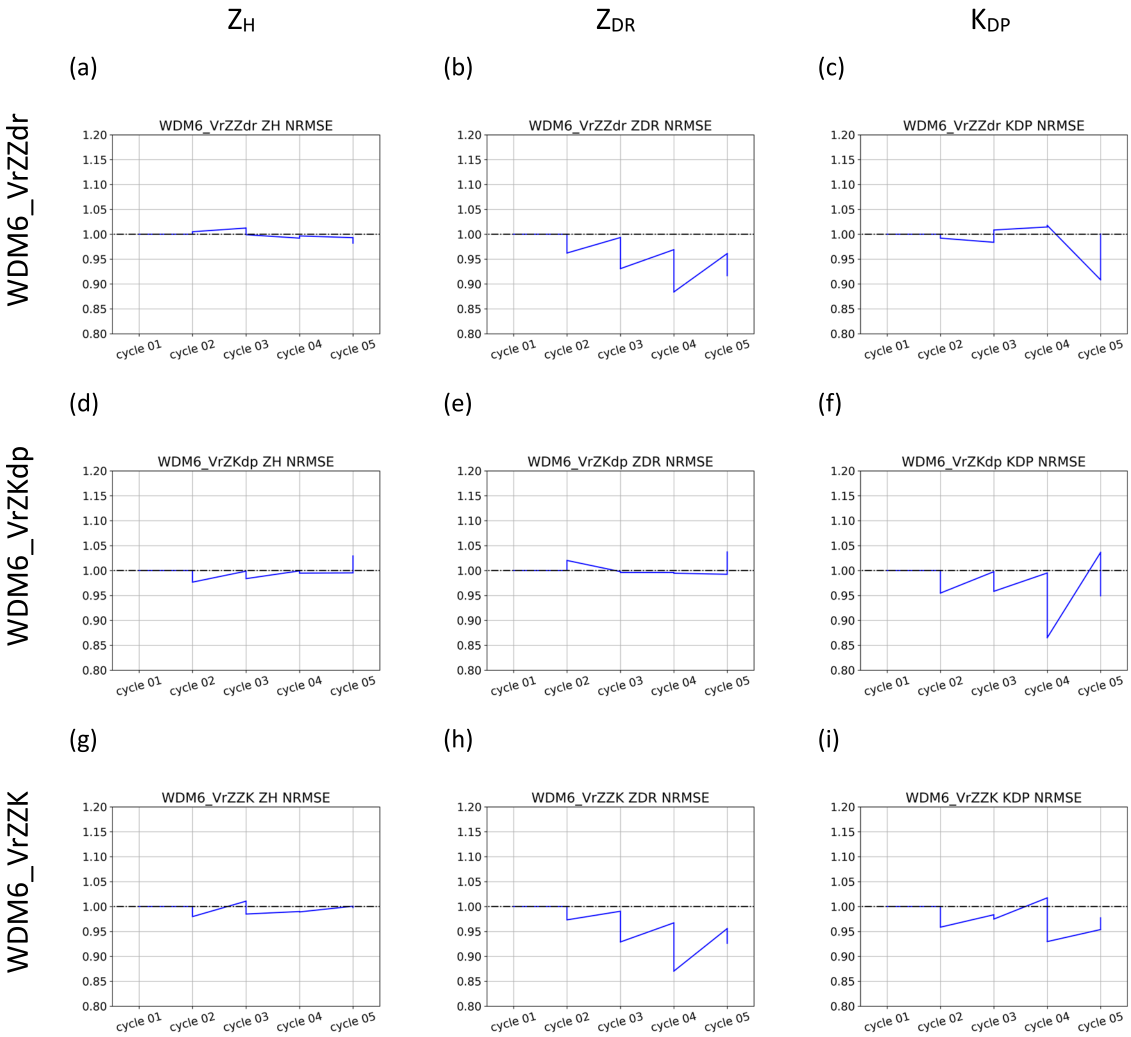

Figure 29 NRMSE of polarimetric parameter in the experiments with WDM6 scheme in the squall line case from 1000 UTC to 1100 UTC on 14th June 2008.

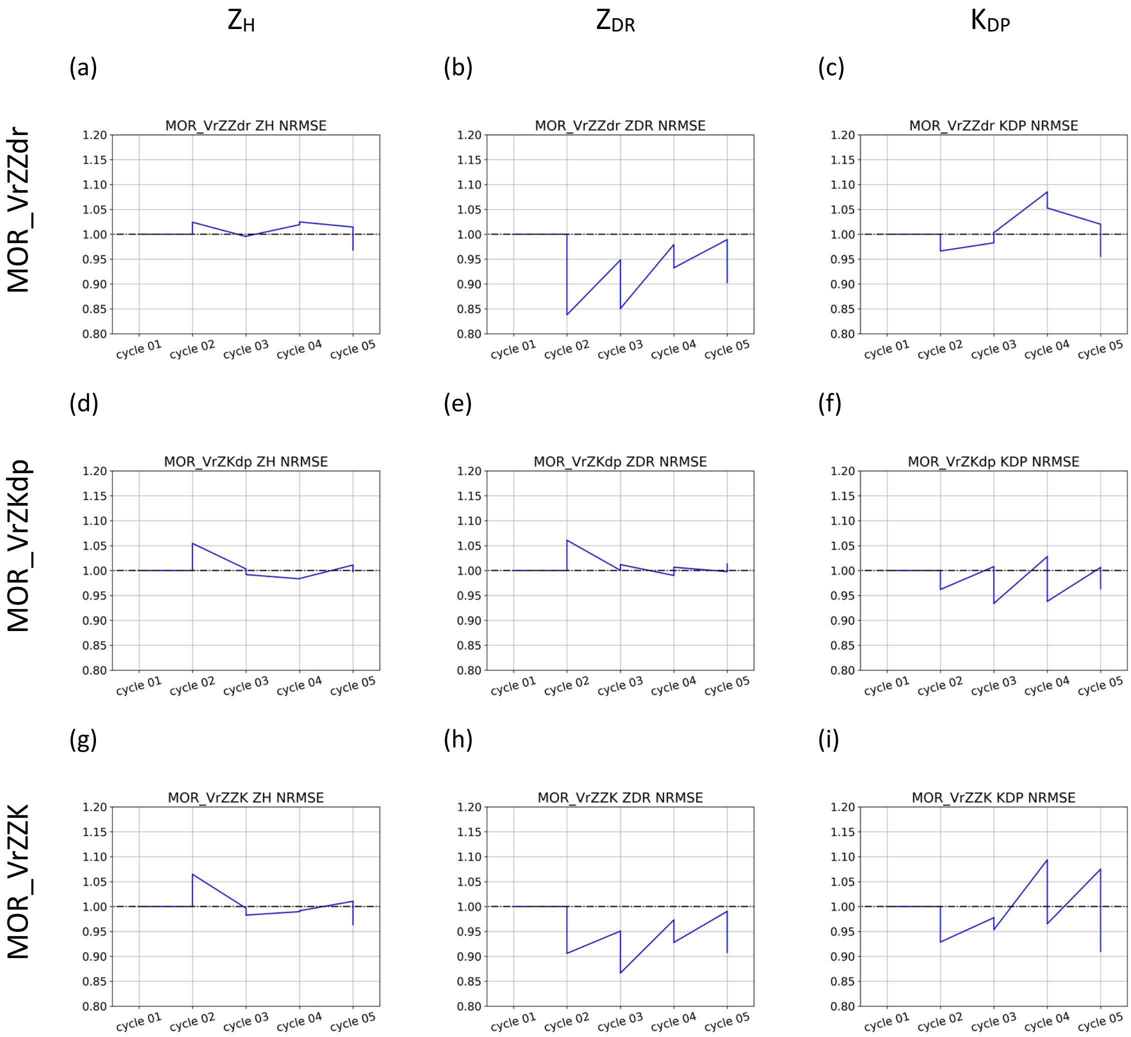

Figure 30 NRMSE of polarimetric parameters in the experiments with MOR scheme in the squall line case from 1000 UTC to 1100 UTC on 14th June 2008.

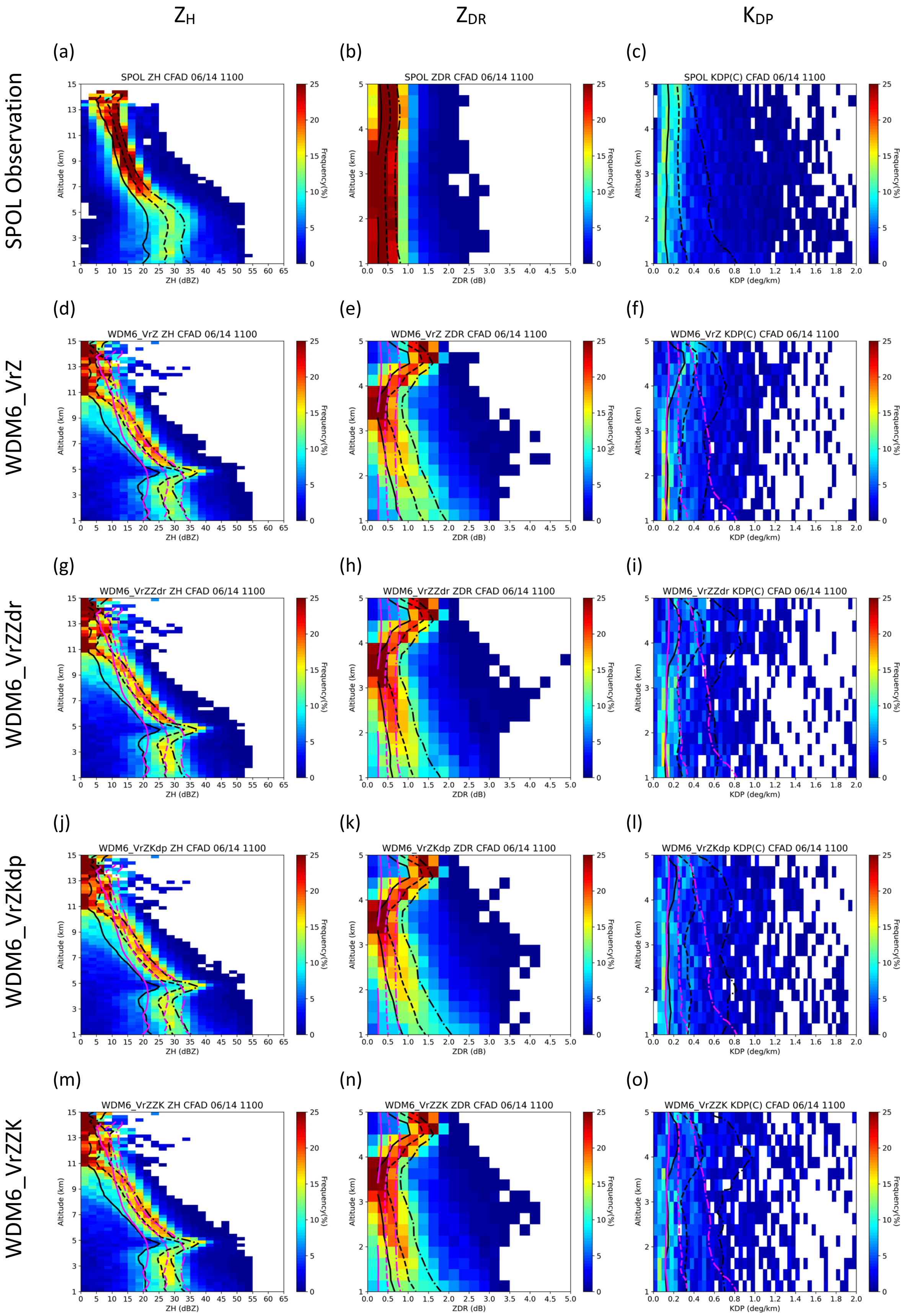

Figure 31 Polarimetric parameter CFADs of SPOL observation and the experiments with WDM6 scheme in the squall line case at 1100 UTC 14th June 2008. The pink lines are the accumulated 25%, 50% and 75% of SPOL observation.

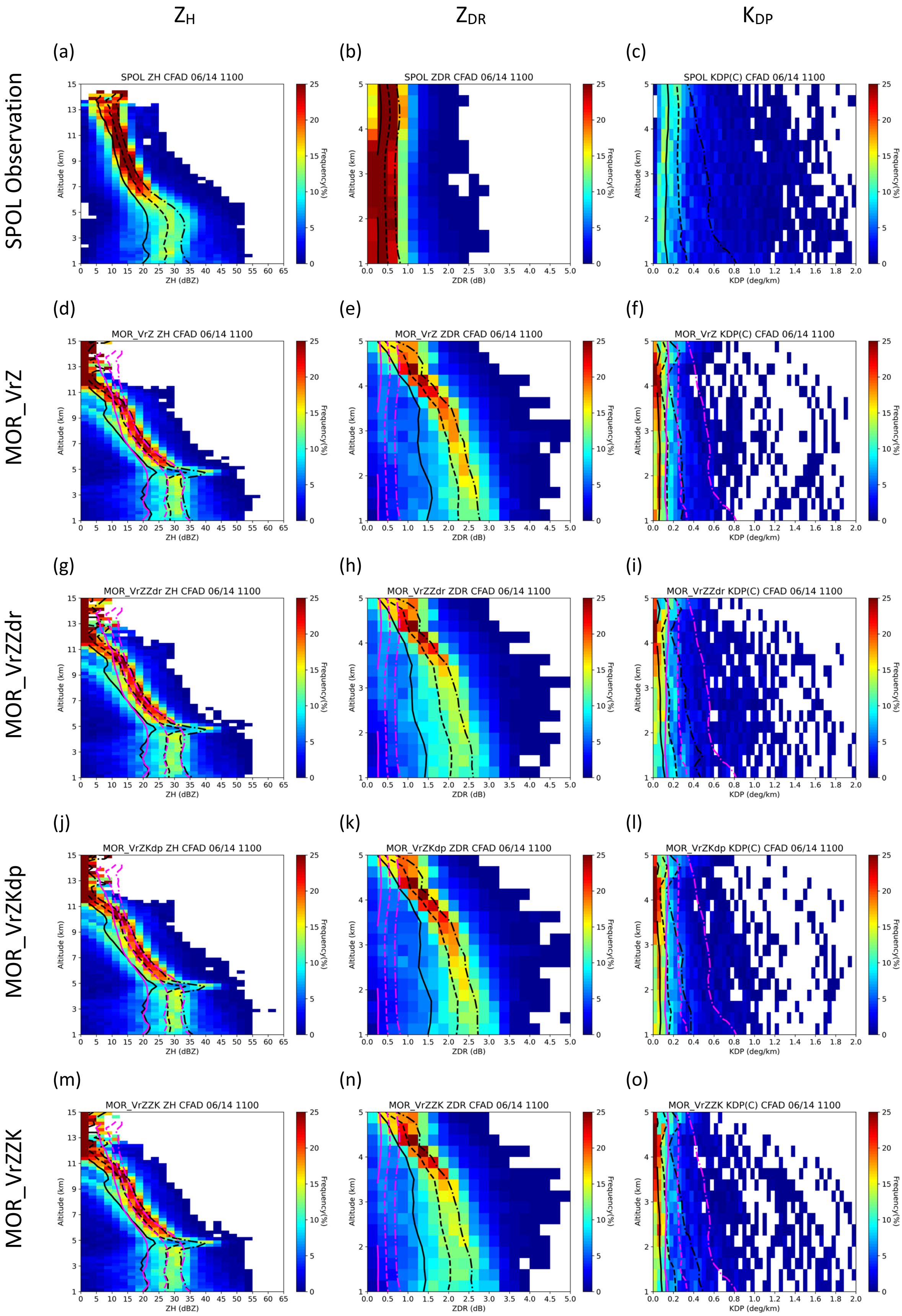

Figure 32 Polarimetric parameter CFADs of SPOL observation and the experiments with MOR scheme in the squall line case at 1100 UTC 14th June 2008. The pink lines are the accumulated 25%, 50% and 75% of SPOL observation.

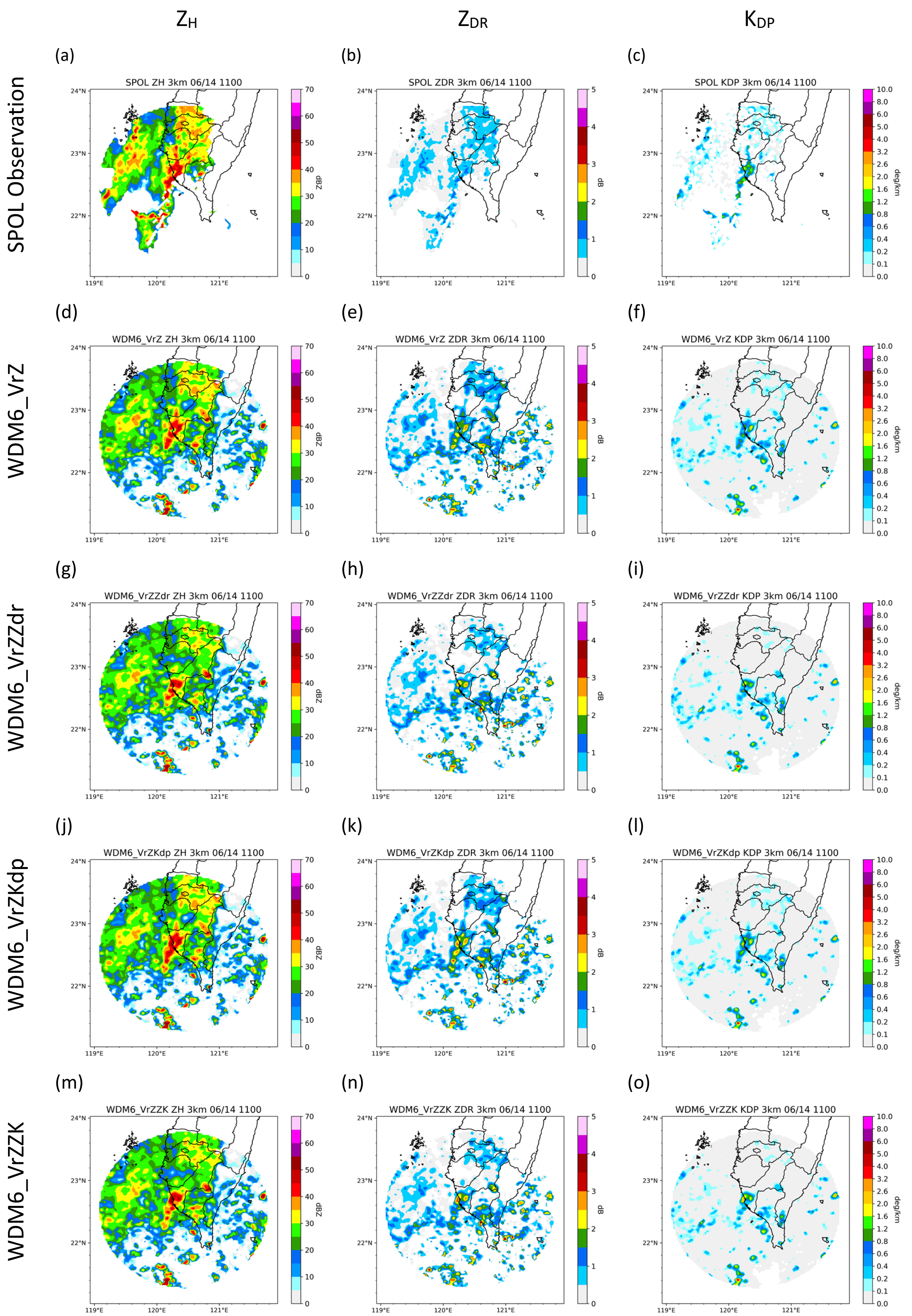

Figure 33 Polarimetric parameter at 3-km height of SPOL observation and the experiments with WDM6 scheme in the squall line case at 1100 UTC 14th June 2008.

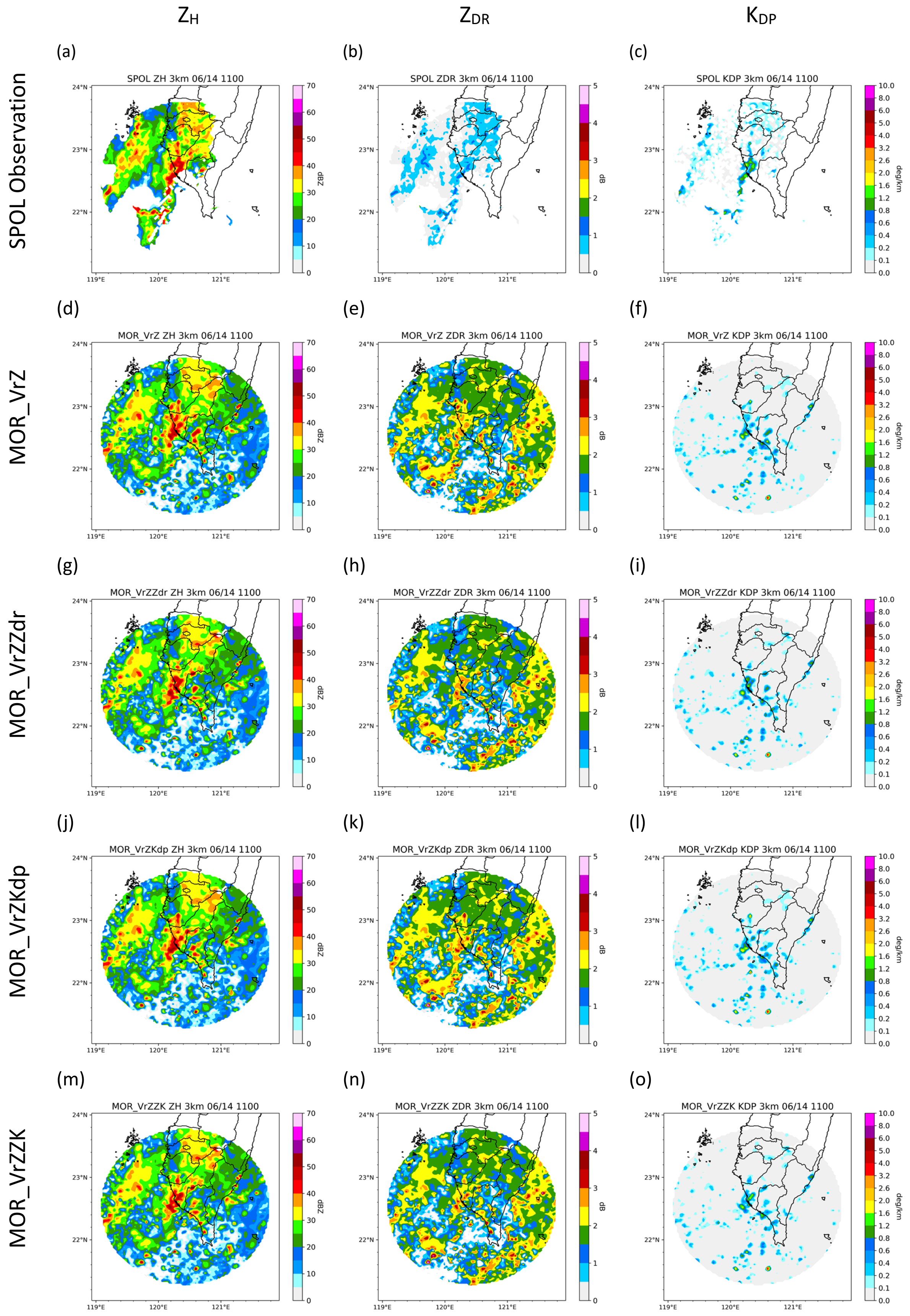

Figure 34 Polarimetric parameter at 3-km height of SPOL observation and the experiments with MOR scheme in the squall line case at 1100 UTC 14th June 2008.

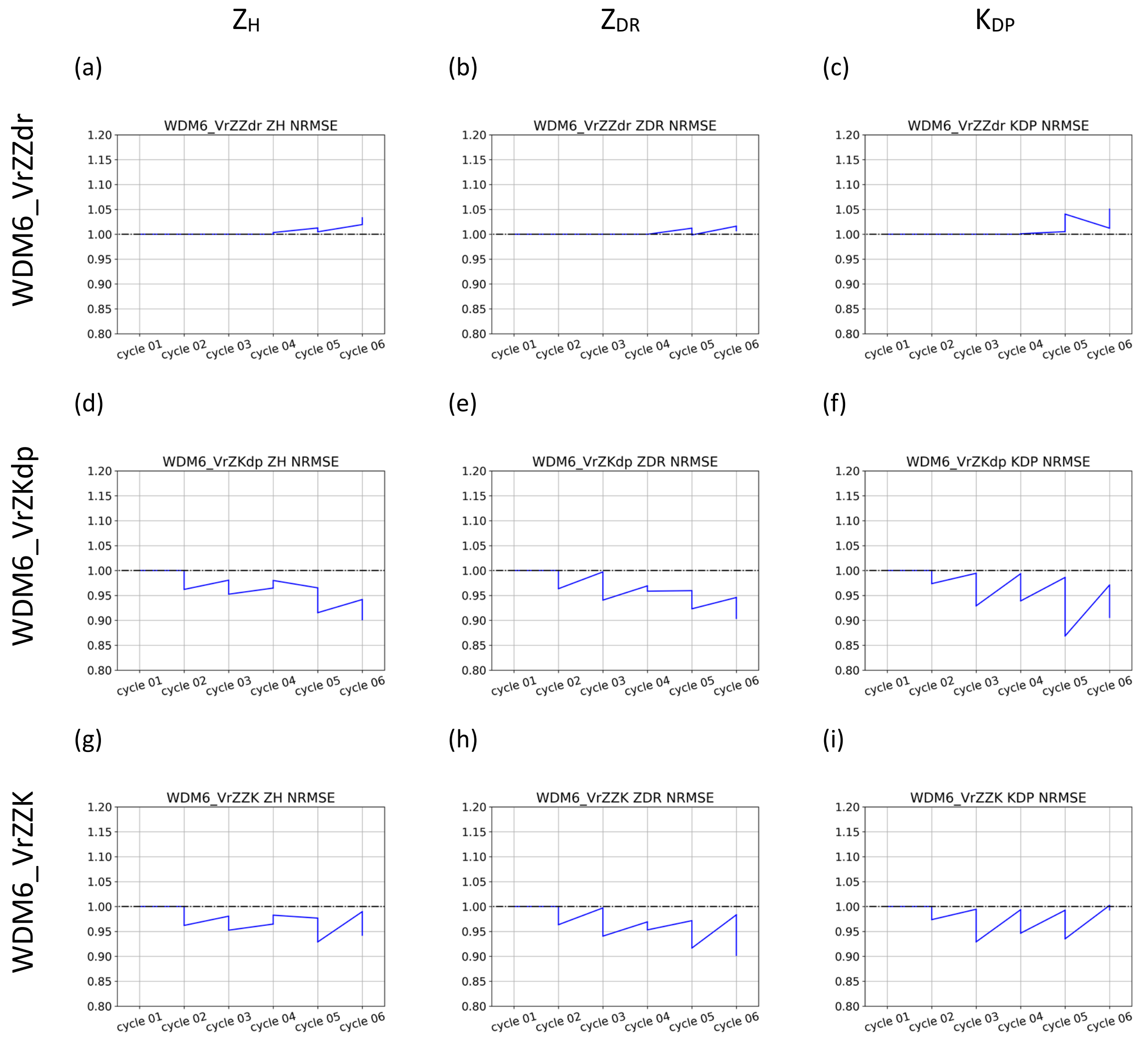

Figure 35 NRMSE of polarimetric parameters in the experiments with WDM6 scheme in the afternoon thunderstorm case from 0700 UTC to 0800 UTC on 20th July 2020.

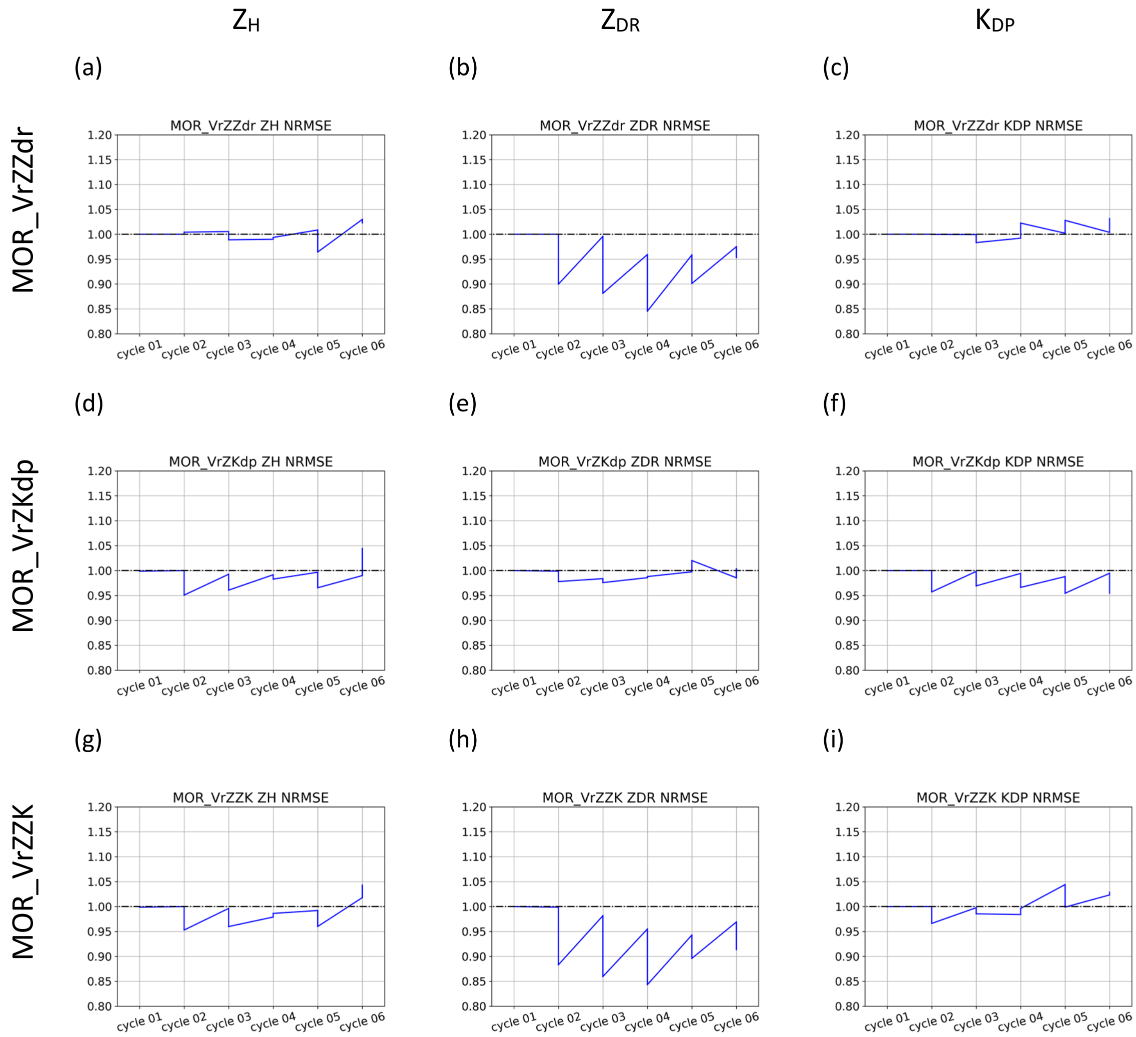

Figure 36 NRMSE of polarimetric parameters in the experiments with MOR scheme in the afternoon thunderstorm case from 0700 UTC to 0800 UTC on 20th July 2020.

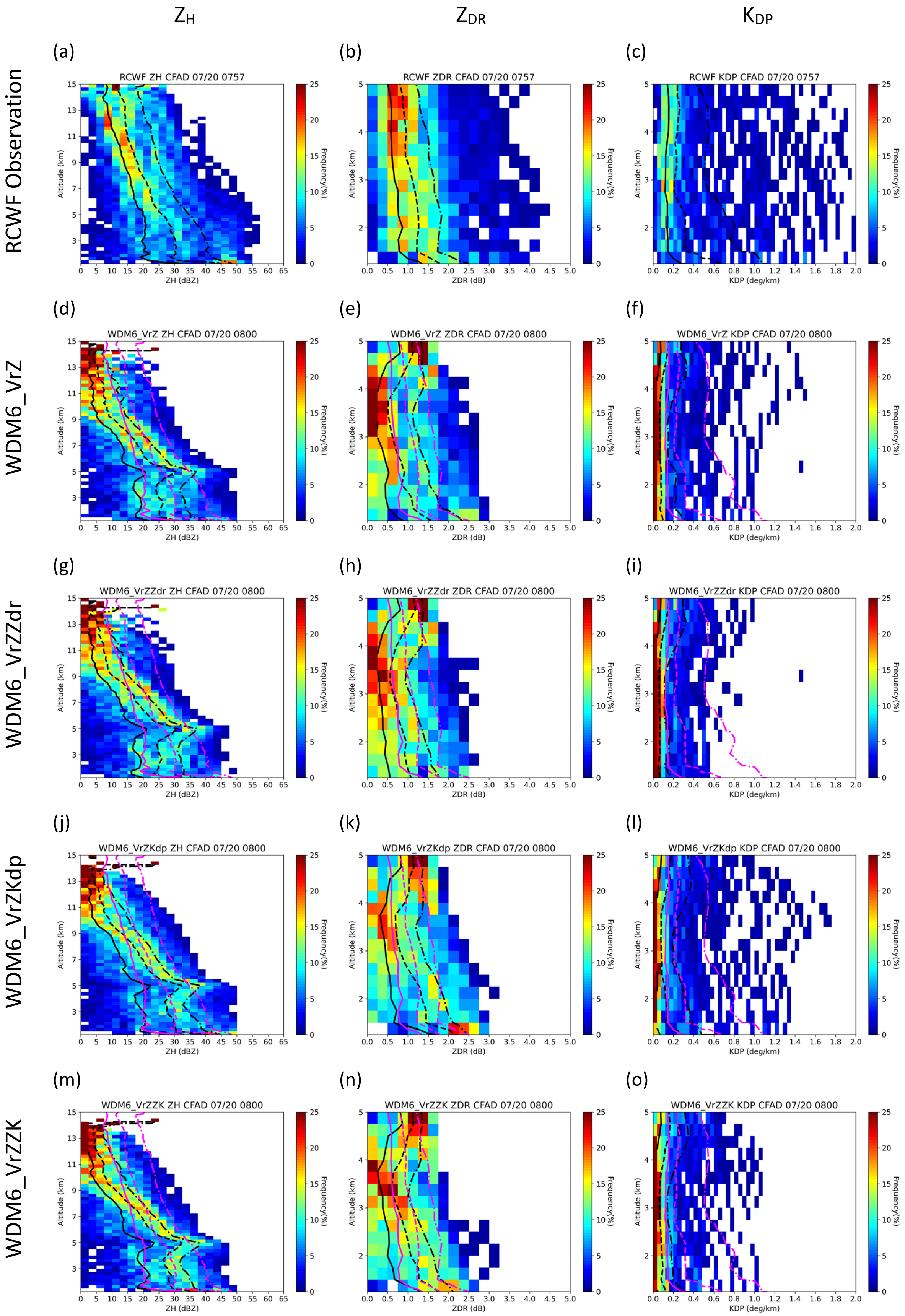

Figure 37 Polarimetric parameter CFADs of RCWF observation and the experiments with WDM6 scheme in the afternoon thunderstorm case at 0800 UTC 20th July 2020. The pink lines are the accumulated 25%, 50% and 75% of RCWF observation.

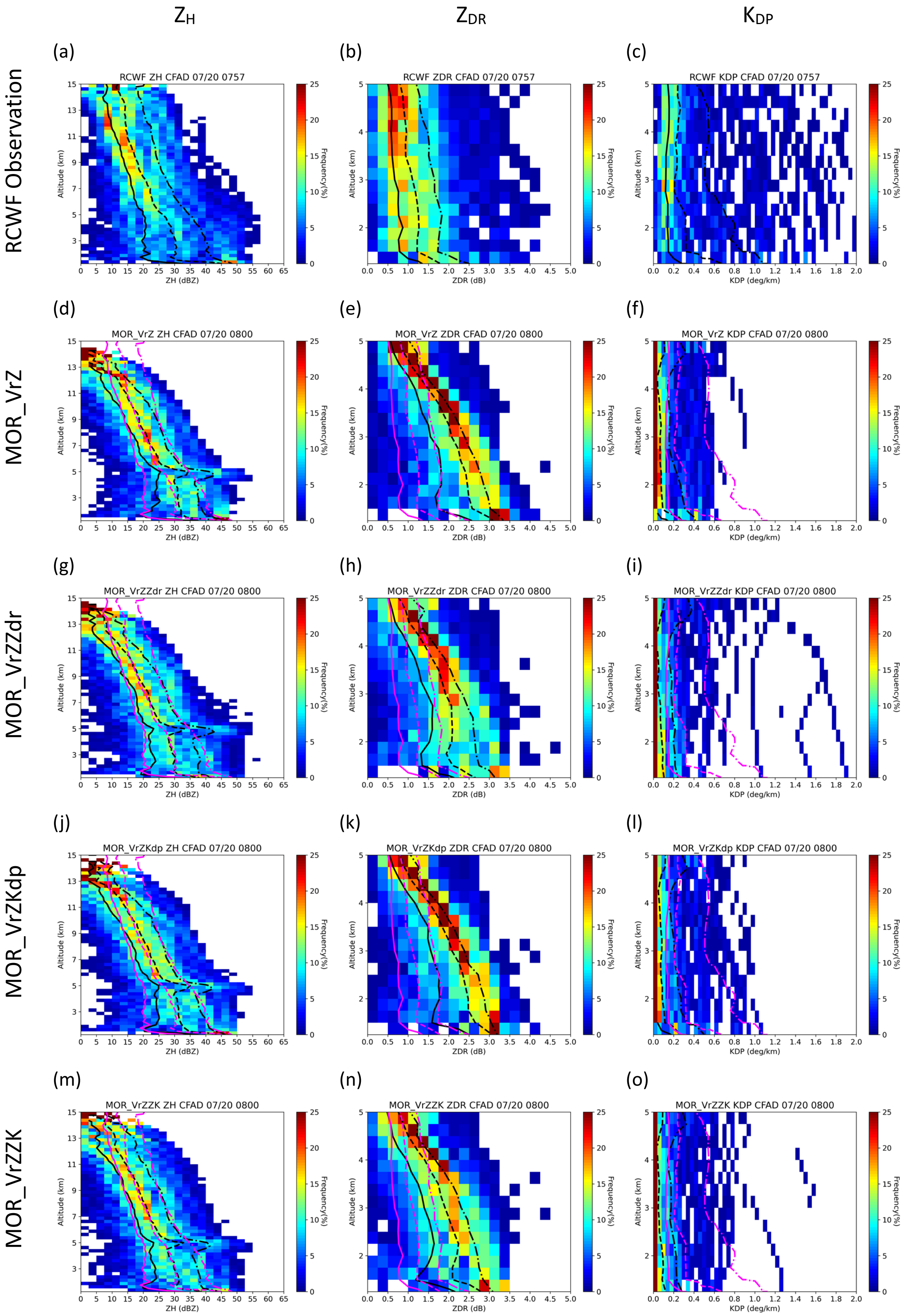

Figure 38 Polarimetric parameter CFADs of RCWF observation and the experiments with MOR scheme in the afternoon thunderstorm case at 0800 UTC 20th July 2020. The pink lines are the accumulated 25%, 50% and 75% of RCWF observation.

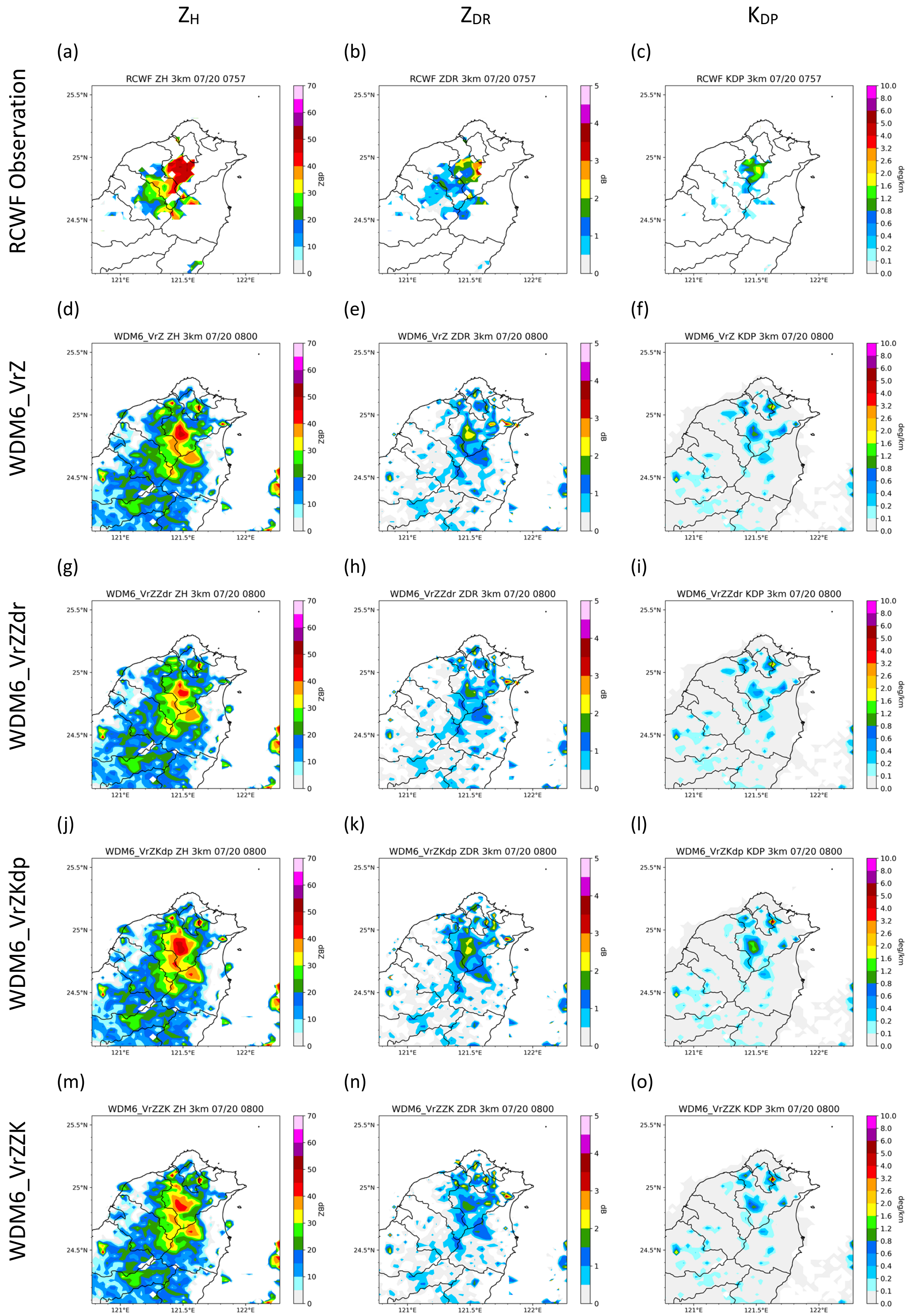

Figure 39 Polarimetric parameter at 3-km height of RCWF observation and the experiments with WDM6 scheme in the afternoon thunderstorm case at 0800 UTC 20th July 2020.

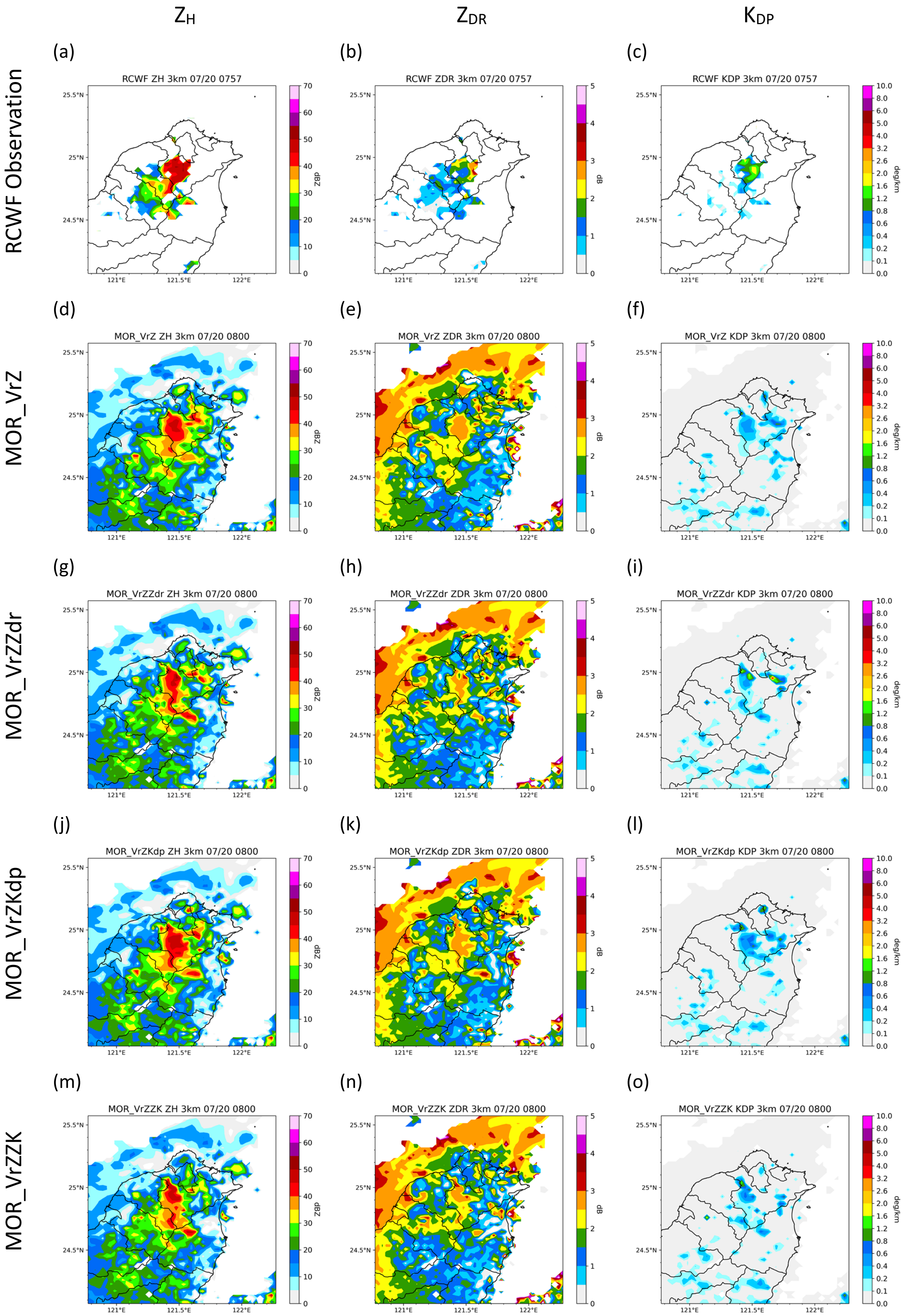

Figure 40 Polarimetric parameter at 3-km height of RCWF observation and the experiments with MOR scheme in the afternoon thunderstorm case at 0800 UTC 20th July 2020.

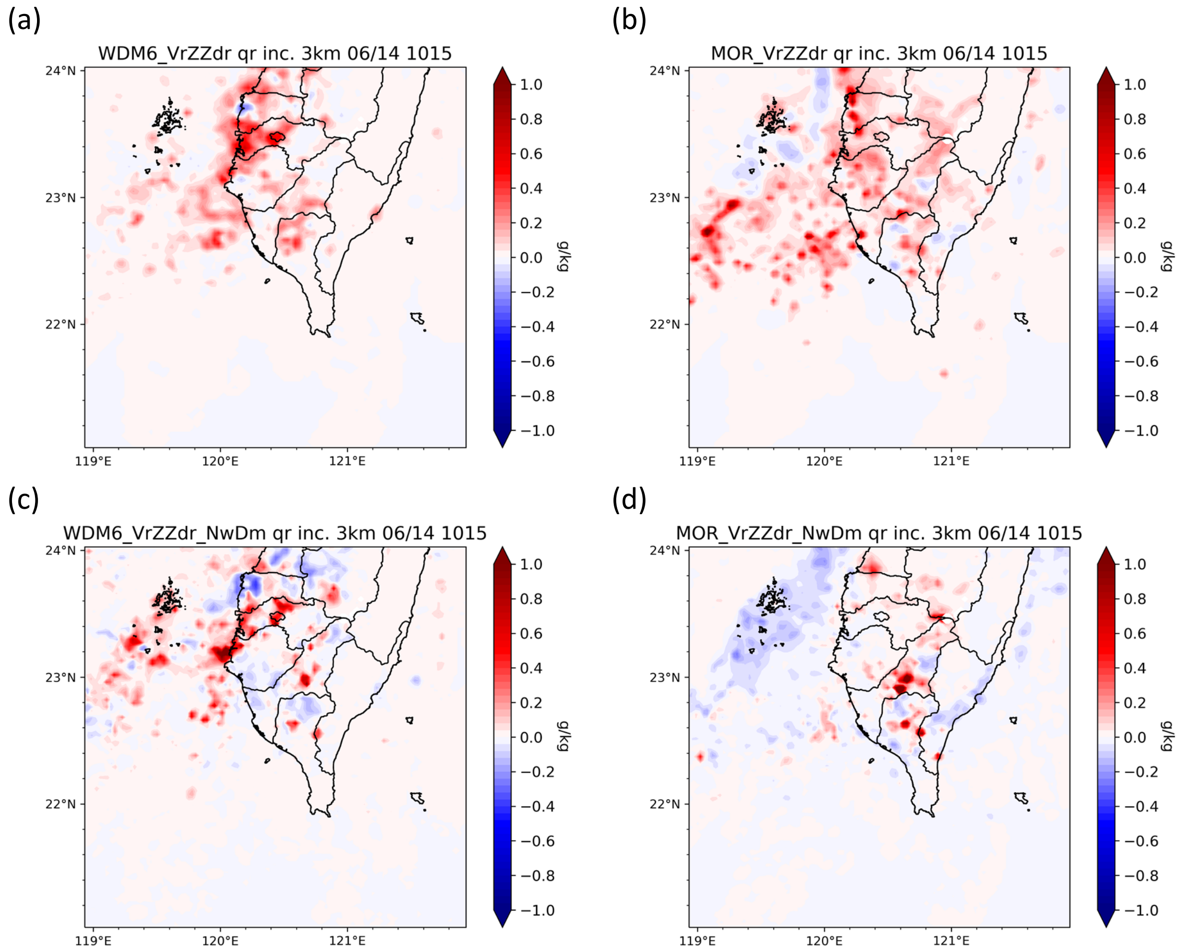

Figure 41 Increment of q_r at 3-km height in the squall line case at 1015 UTC 14th June 2008. (a) WDM6_VrZZdr (b) MOR_VrZZdr (c) MOR_VrZZdr_NwDm (d) MOR_VrZZdr_NwDm.

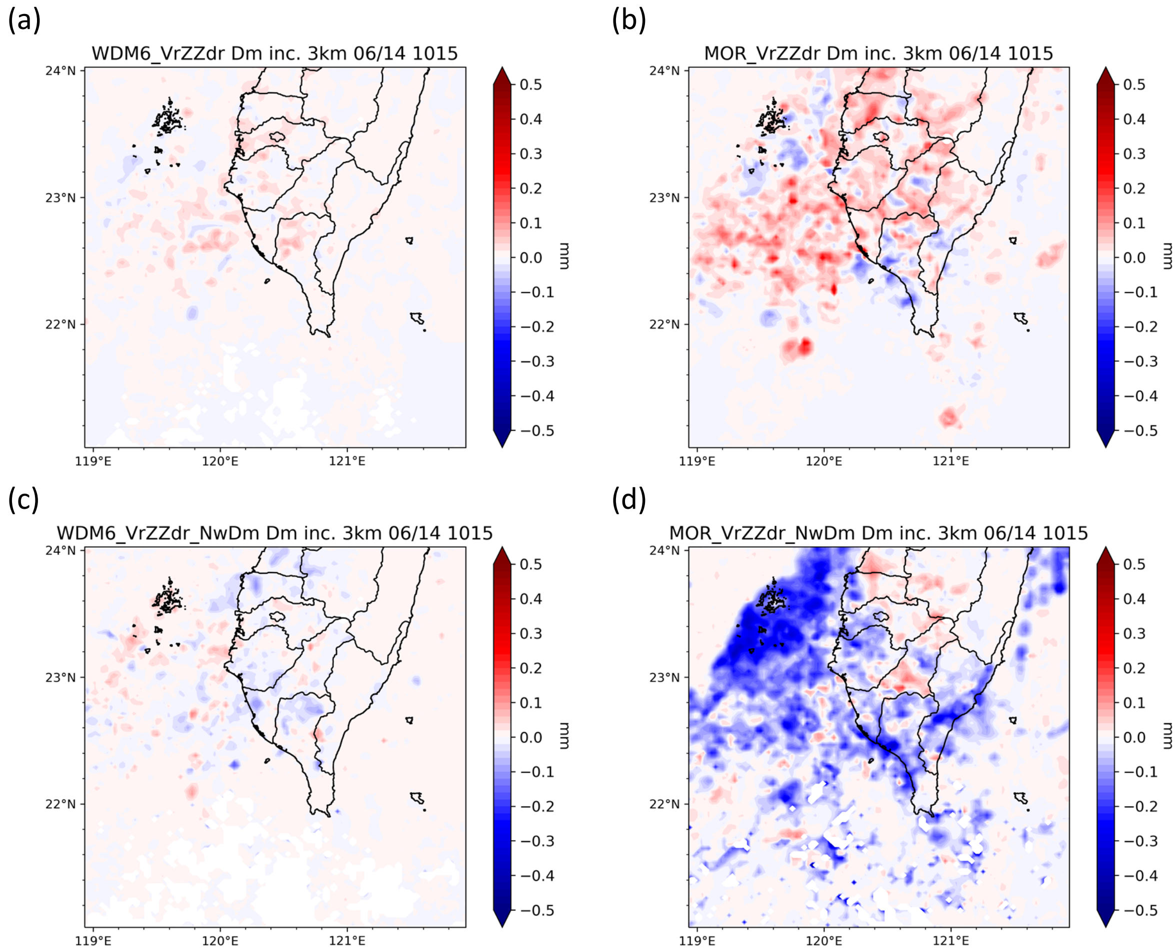

Figure 42 Increment of D_m at 3-km height in the squall line case at 1015 UTC 14th June 2008. (a) WDM6_VrZZdr (b) MOR_VrZZdr (c) MOR_VrZZdr_NwDm (d) MOR_VrZZdr_NwDm.

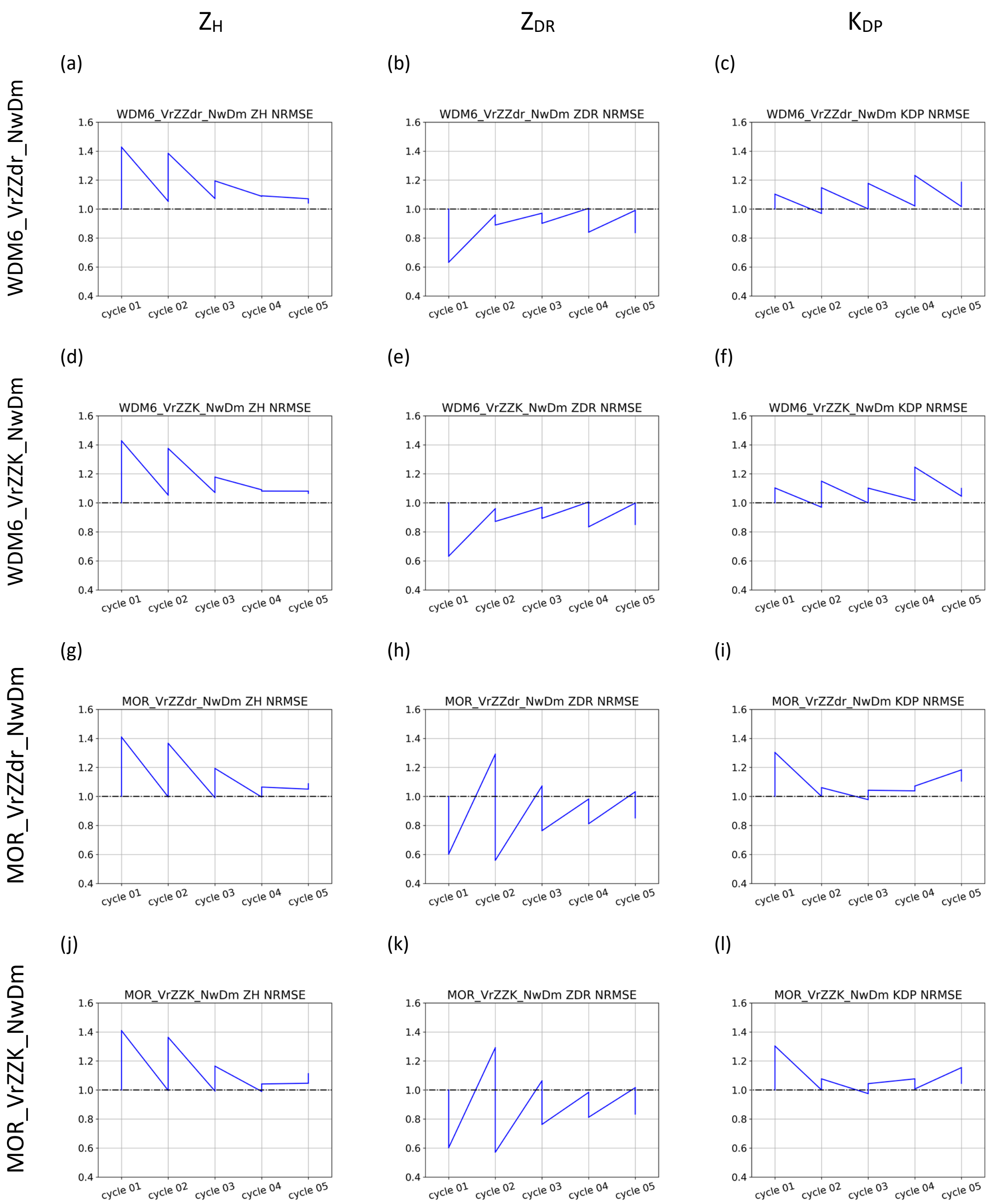

Figure 43 NRMSE of polarimetric parameters in the experiments with the new approach in the squall line case from 1000 UTC to 1100 UTC 14th June 2020.

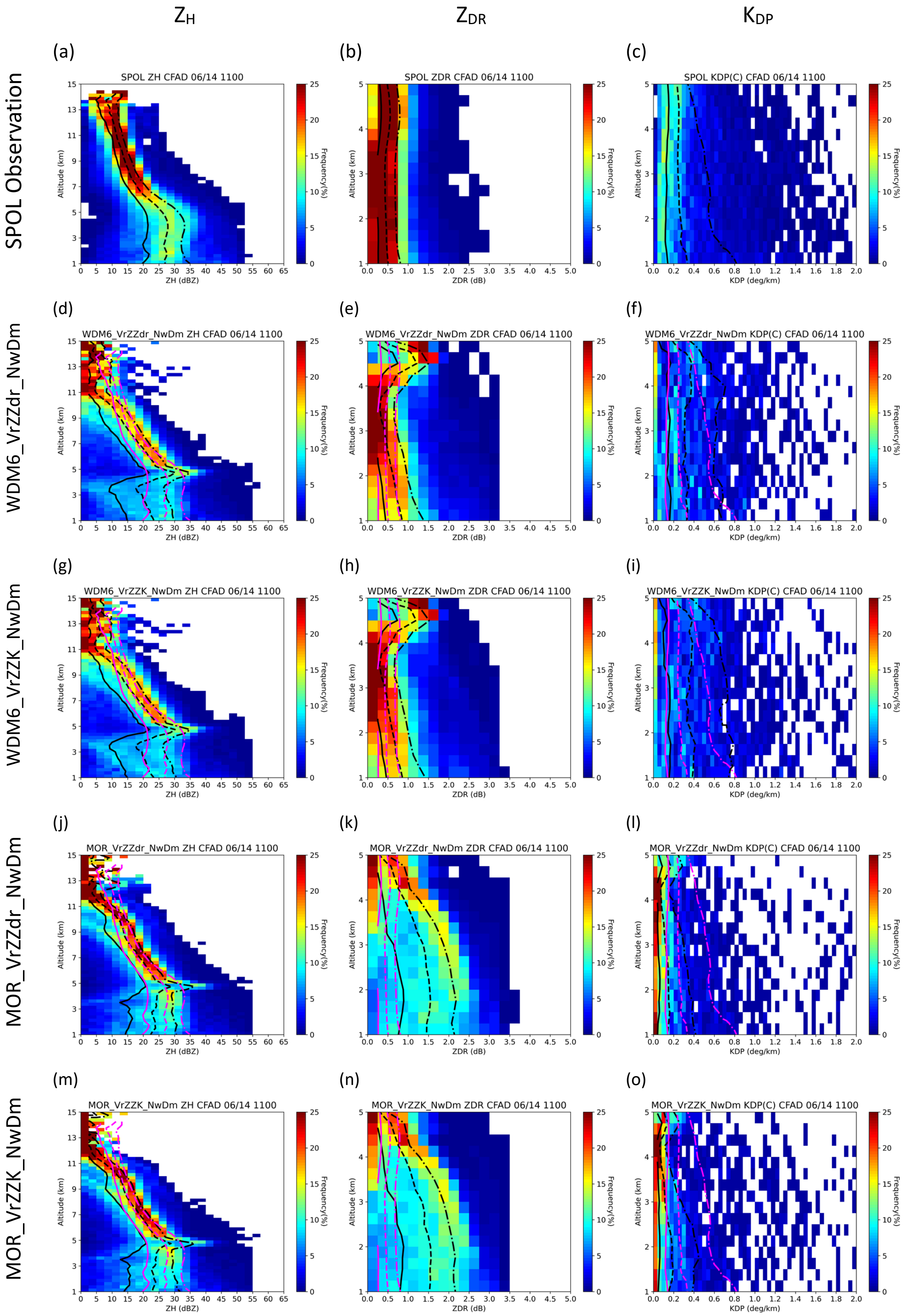

Figure 44 Polarimetric parameter CFADs of SPOL observation and the experiments with the new approach in the squall line case at 1100 UTC 14th June 2008. The pink lines are the accumulated 25%, 50% and 75% of SPOL observation.

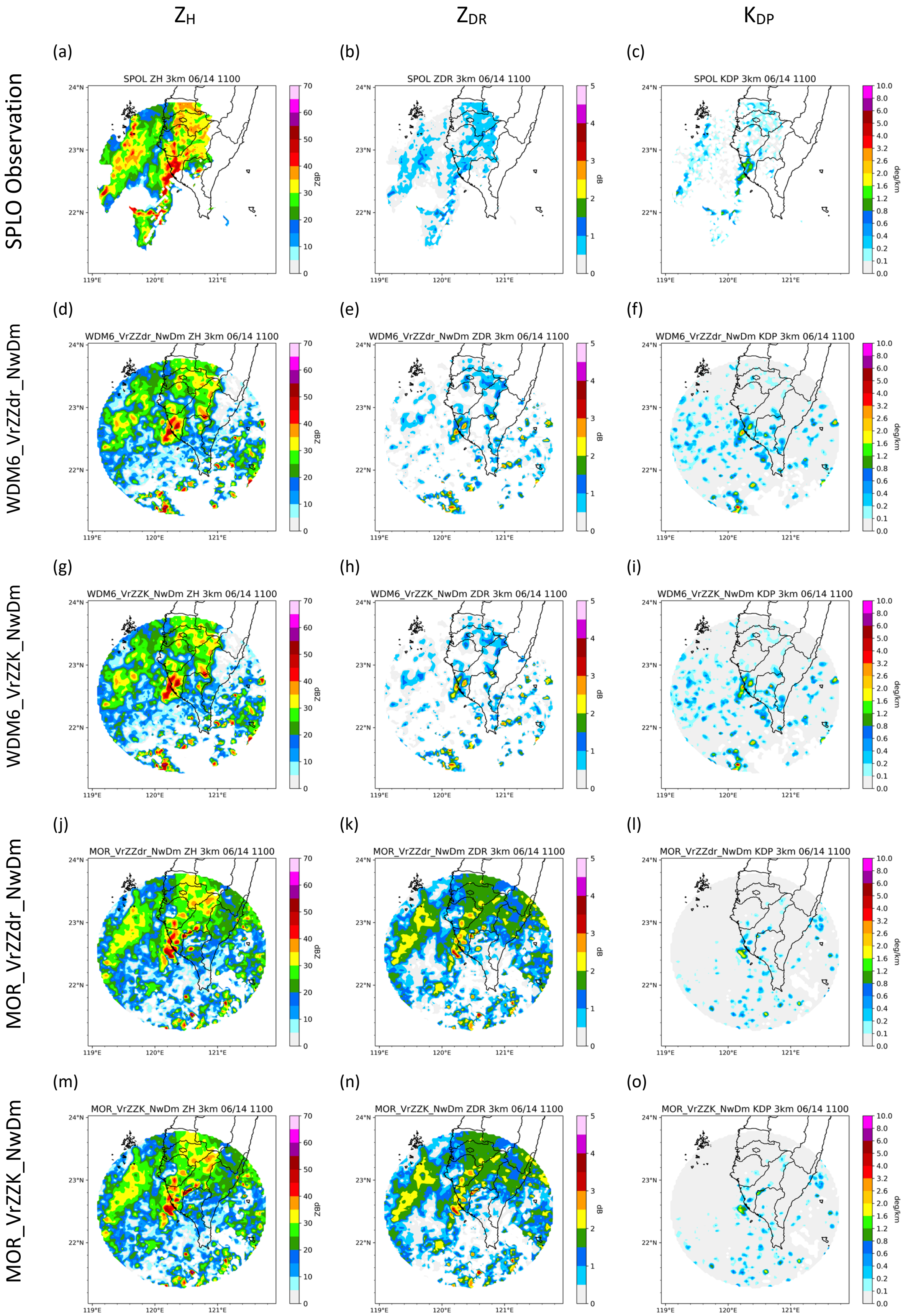

Figure 45 Polarimetric parameter at 3-km height of SPOL observation and the experiments with the new approach in the squall line case at 1100 UTC 14th June 2008.

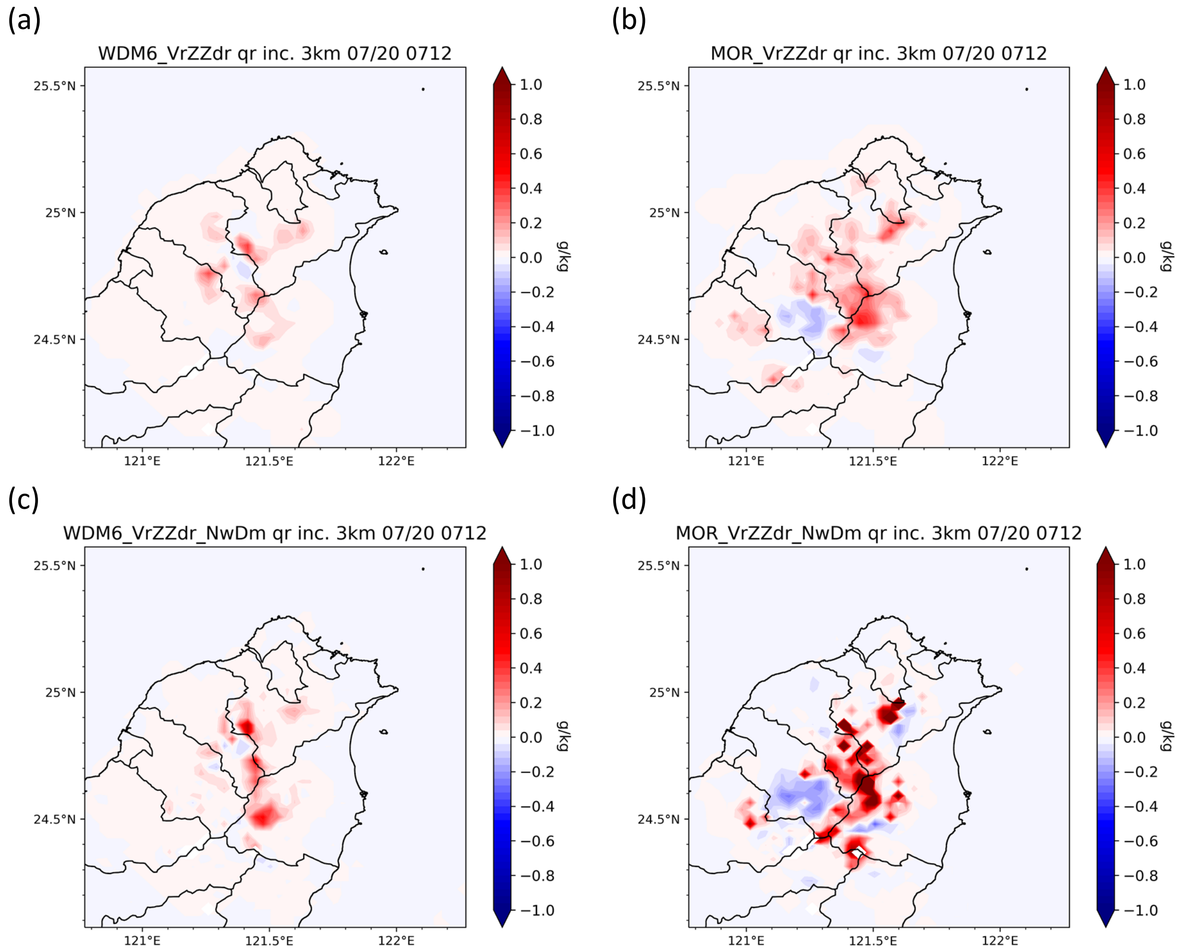

Figure 46 Increment of q_r at 3-km height in the afternoon thunderstorm case at 0712 UTC 20th July 2020. (a) WDM6_VrZZdr (b) MOR_VrZZdr (c) MOR_VrZZdr_NwDm (d) MOR_VrZZdr_NwDm.

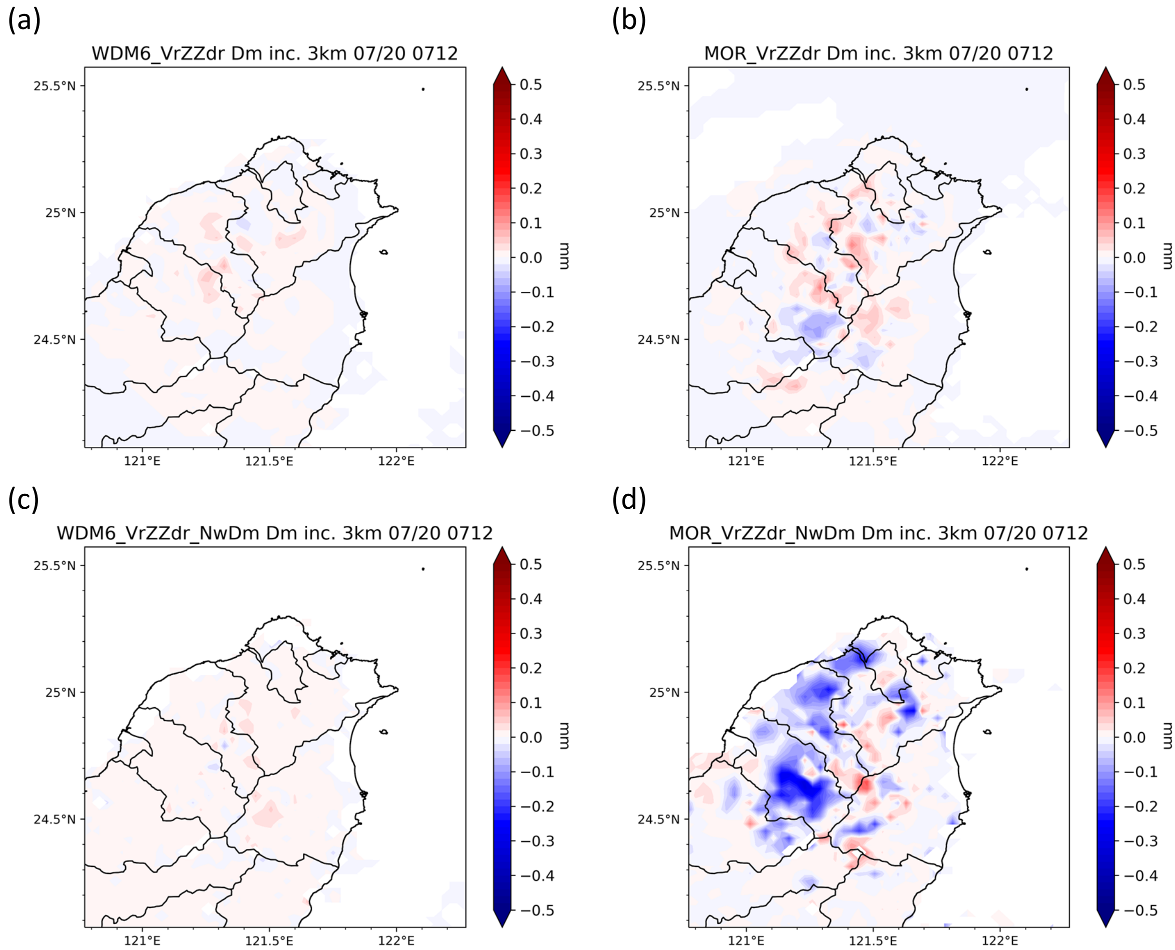

Figure 47 Increment of D_m at 3-km height in the afternoon thunderstorm case at 0712 UTC 20th July 2008. (a) WDM6_VrZZdr (b) MOR_VrZZdr (c) WDM6_VrZZdr_NwDm (d) MOR_VrZZdr_NwDm.

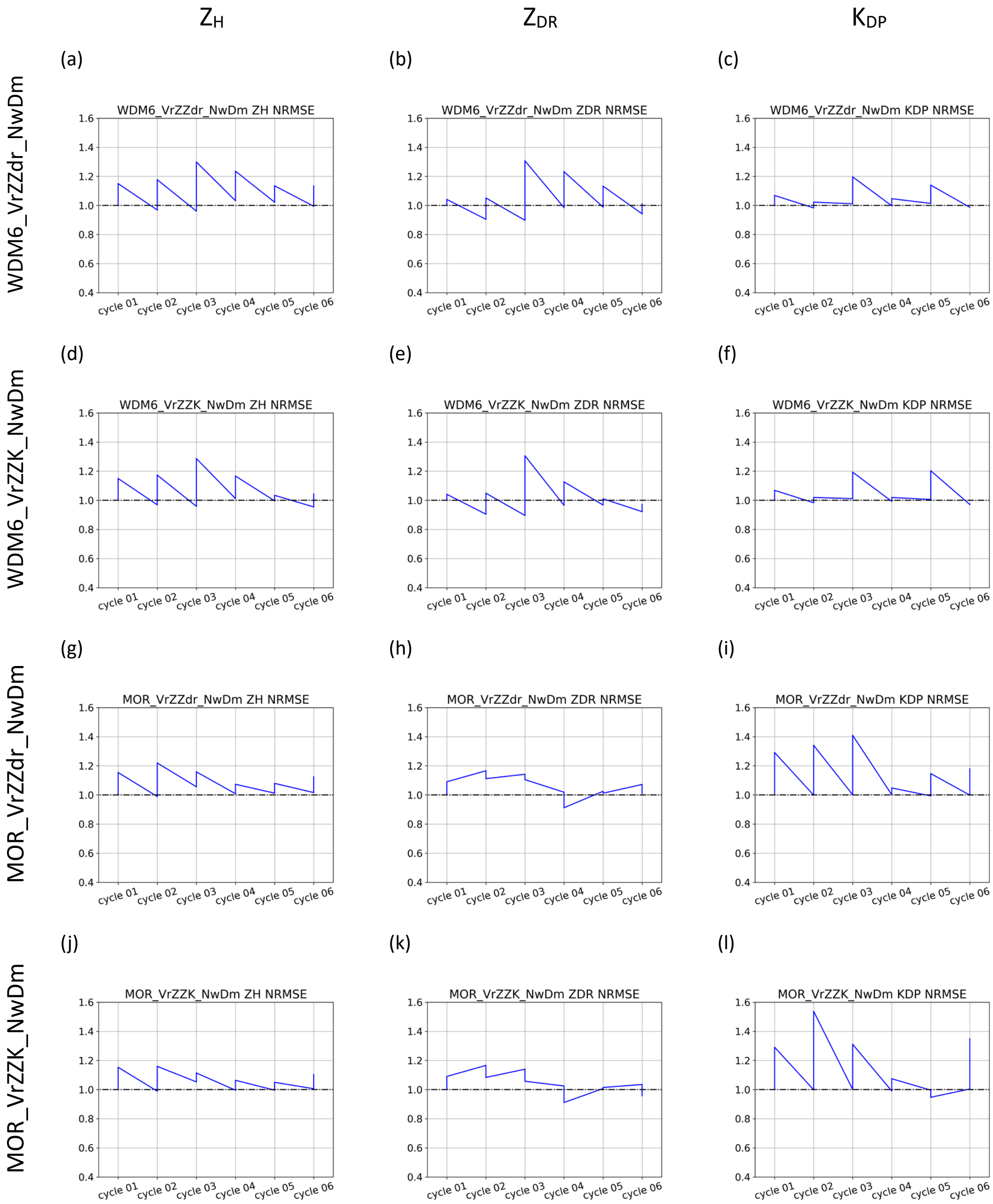

Figure 48 NRMSE of polarimetric parameters in the experiments with the new approach in the afternoon thunderstorm case from 0700UTC to 0800UTC on 20th July 2020.

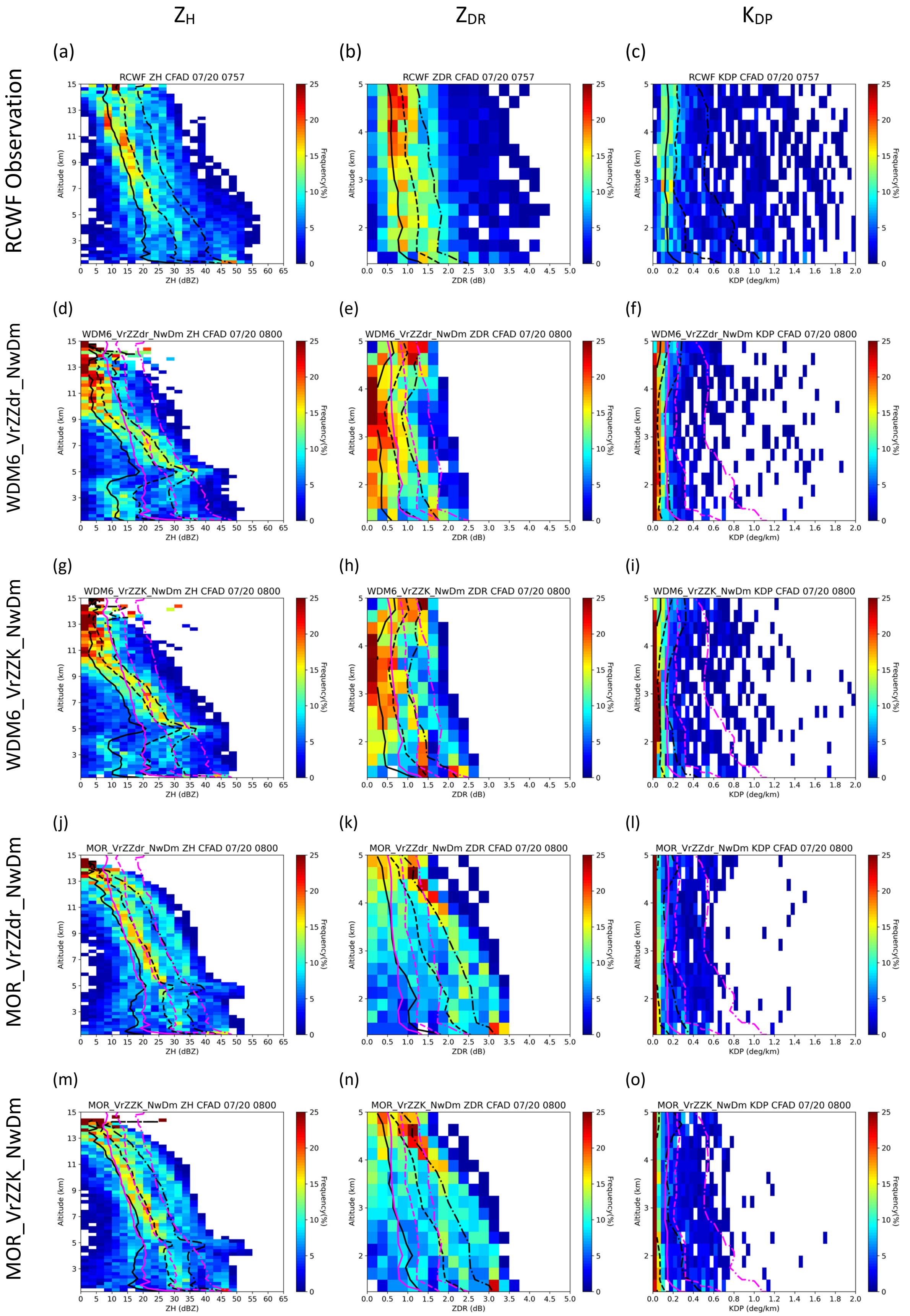

Figure 49 Polarimetric parameter CFADs of RCWF observation and the experiments with the new approach in the afternoon thunderstorm case at 0800 UTC 20th July 2020. The pink lines are the accumulated 25%, 50% and 75% of RCWF observation.

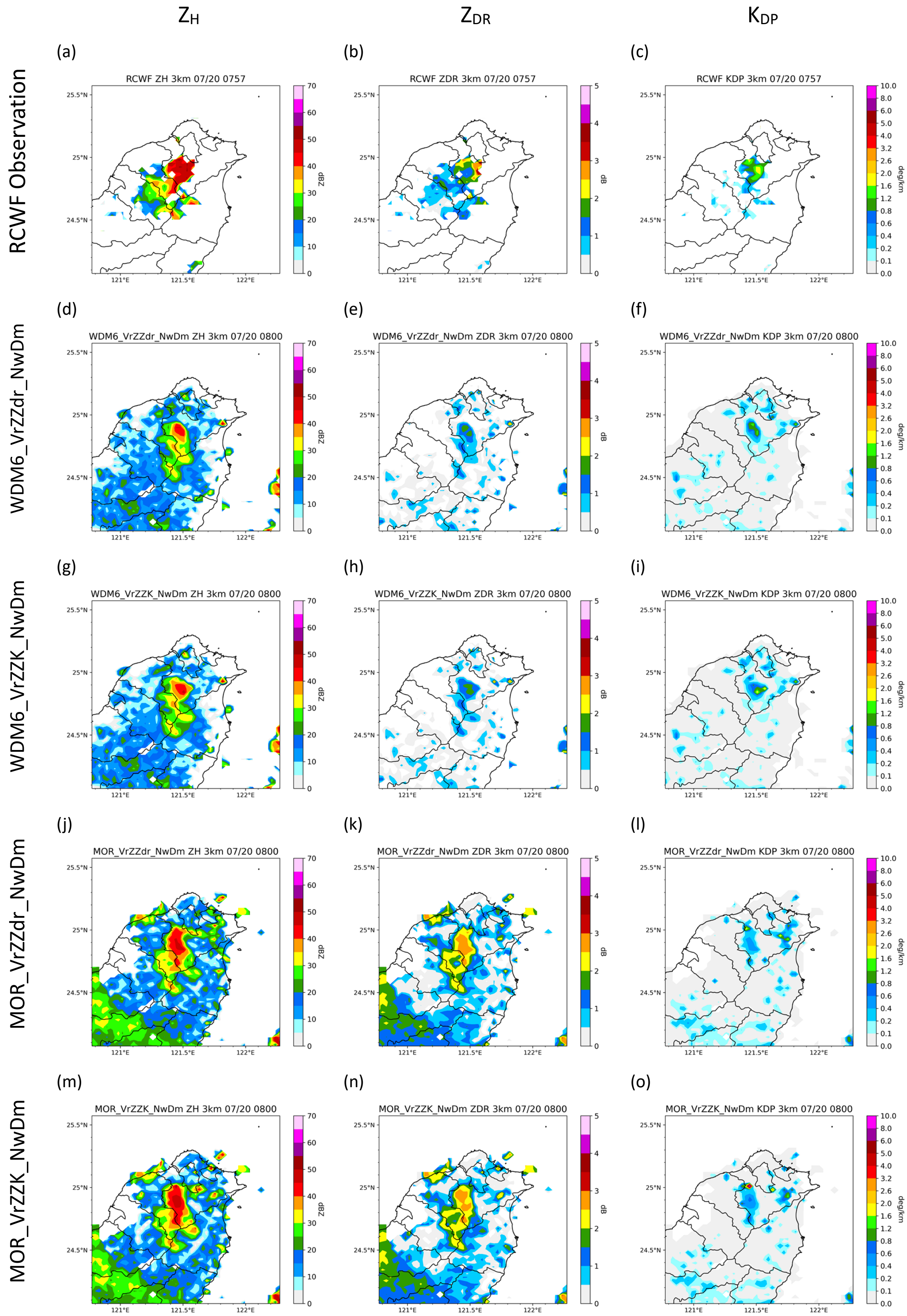

Figure 50 Polarimetric parameter at 3-km height of SPOL observation and the experiments with the new approach in the afternoon thunderstorm case at 0800 UTC 20th July 2020.

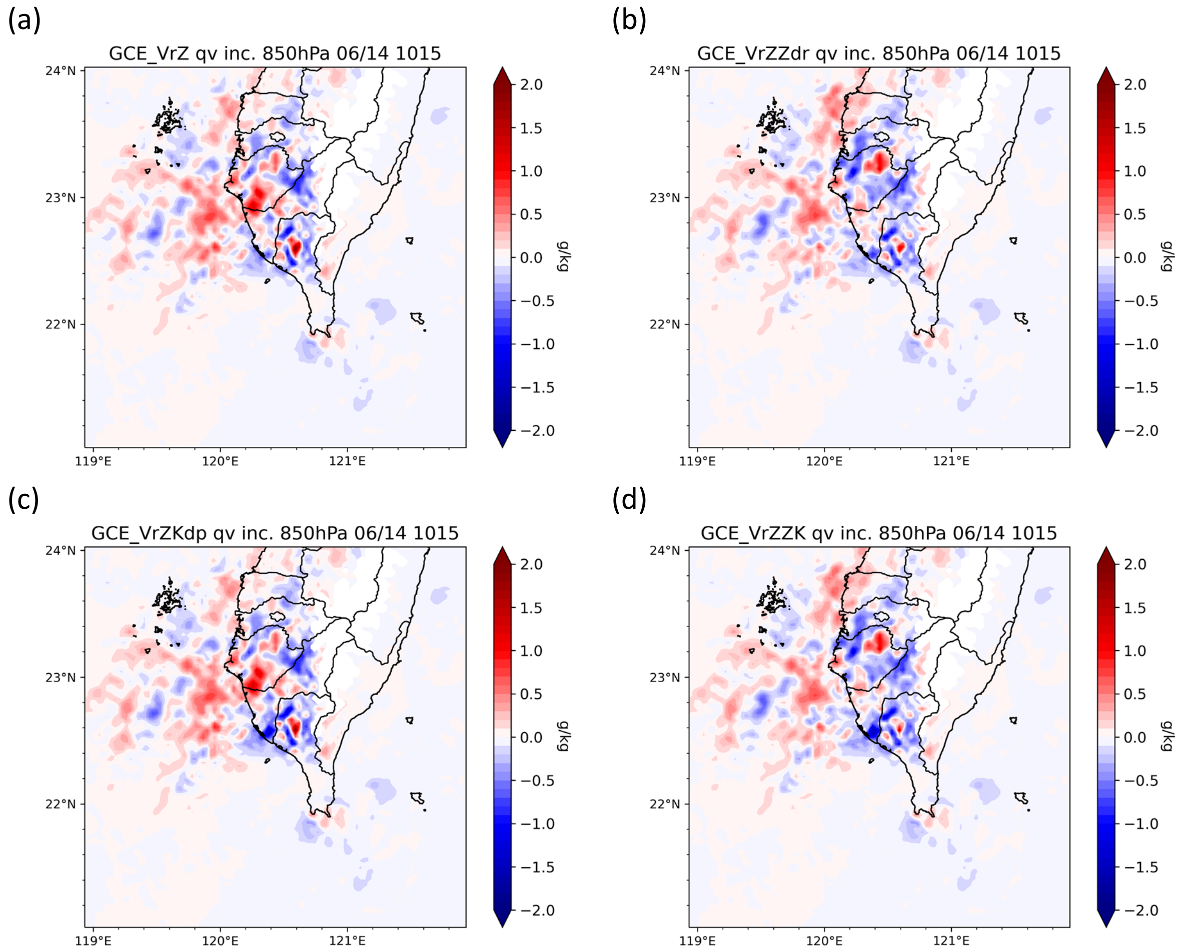

Figure 51 Water vapor increment at 850 hPa in the squall line experiments with GCE scheme at 1015 UTC 14th June 2008. (a) GCE_VrZ (b) GCE_VrZZdr (c) GCE_VrZKdp (d) GCE_VrZZK.

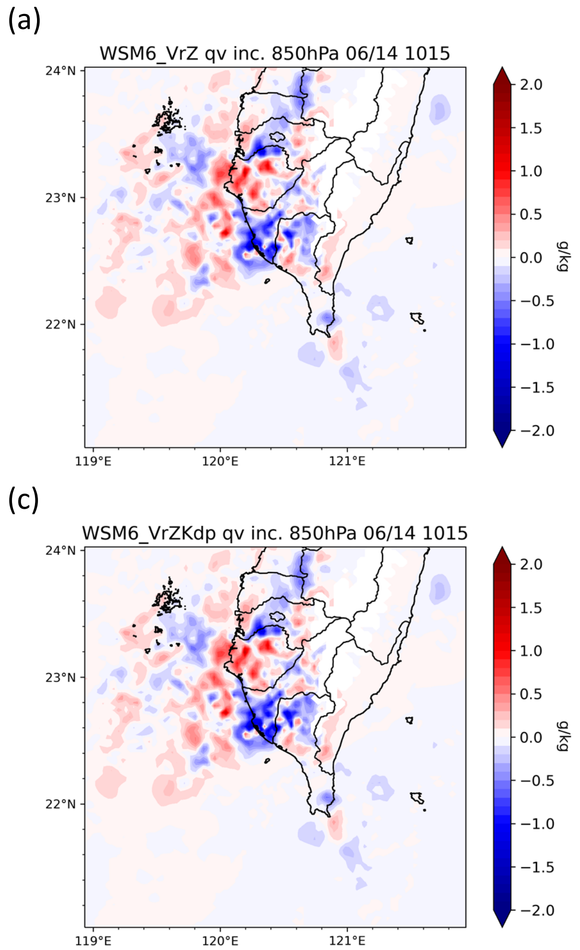

Figure 52 Water vapor increment at 850 hPa in the squall line experiments with WSM6 scheme at 1015 UTC 14th June 2008. (a) WSM6_VrZ (b) WSM6_VrZZdr (c) WSM6_VrZKdp (d) WSM6_VrZZK.

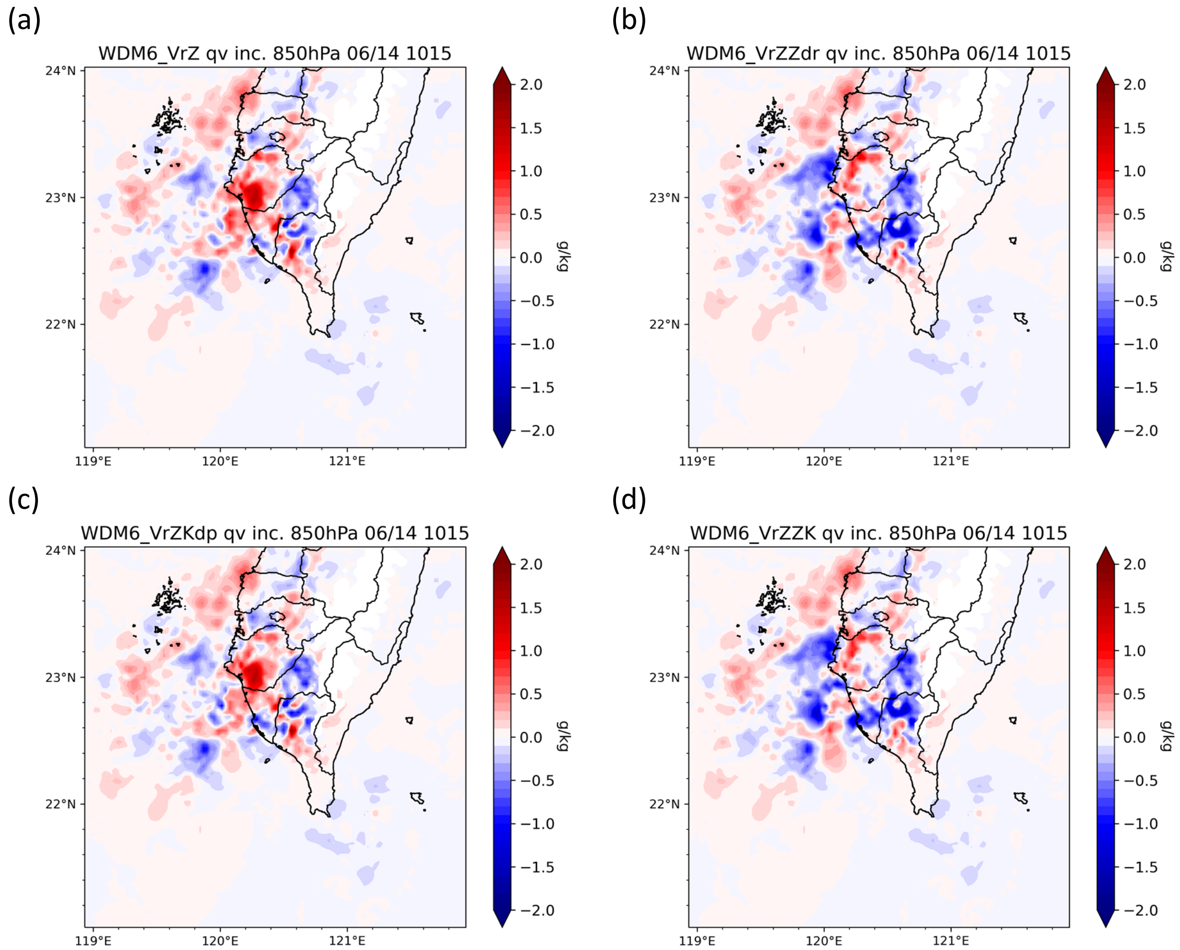

Figure 53 Water vapor increment at 850 hPa in the squall line experiments with WDM6 scheme at 1015 UTC 14th June 2008. (a) WDM6_VrZ (b) WDM6_VrZZdr (c) WDM6_VrZKdp (d) WDM6_VrZZK.

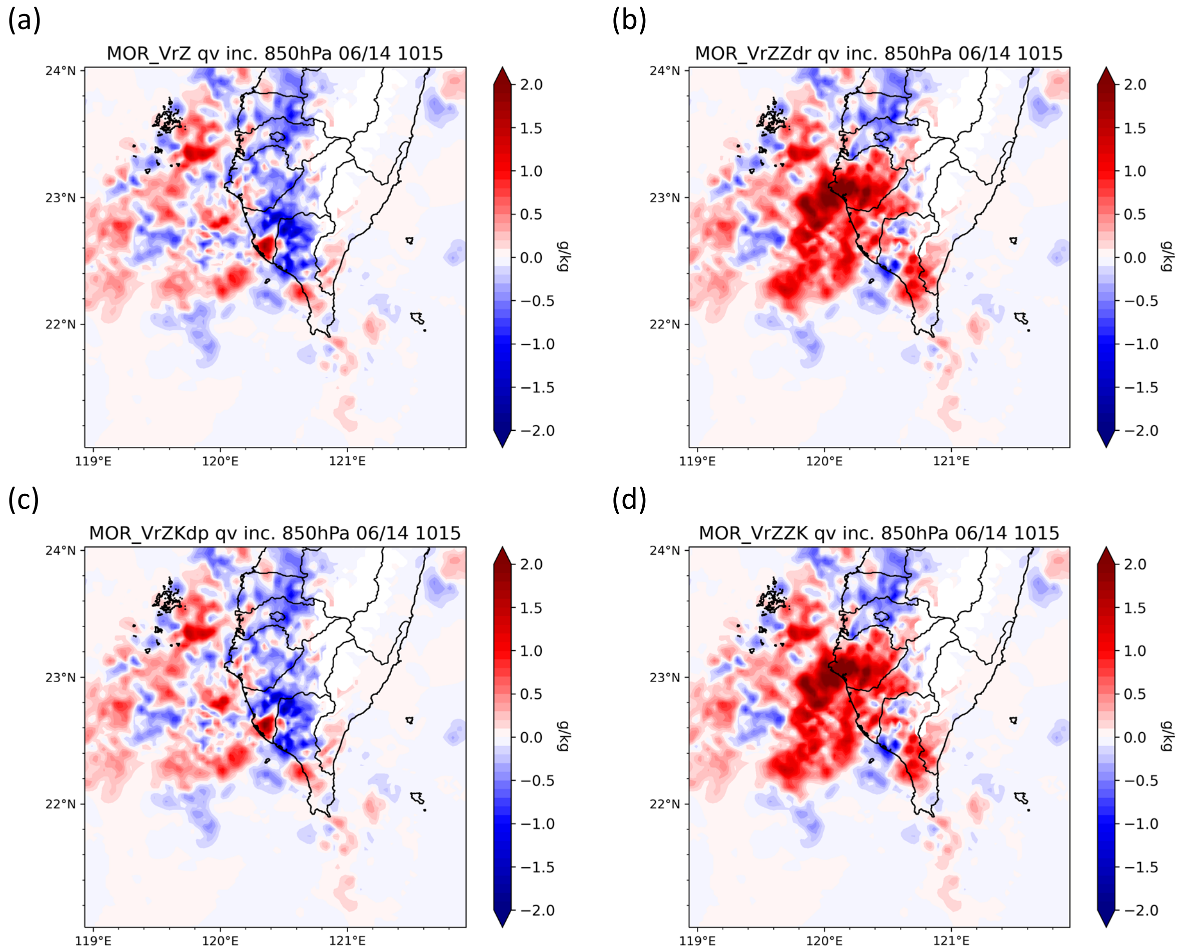

Figure 54 Water vapor increment at 850 hPa in the squall line experiments with MOR scheme at 1015 UTC 14th June 2008. (a) MOR_VrZ (b) MOR_VrZZdr (c) MOR_VrZKdp (d) MOR_VrZZK.

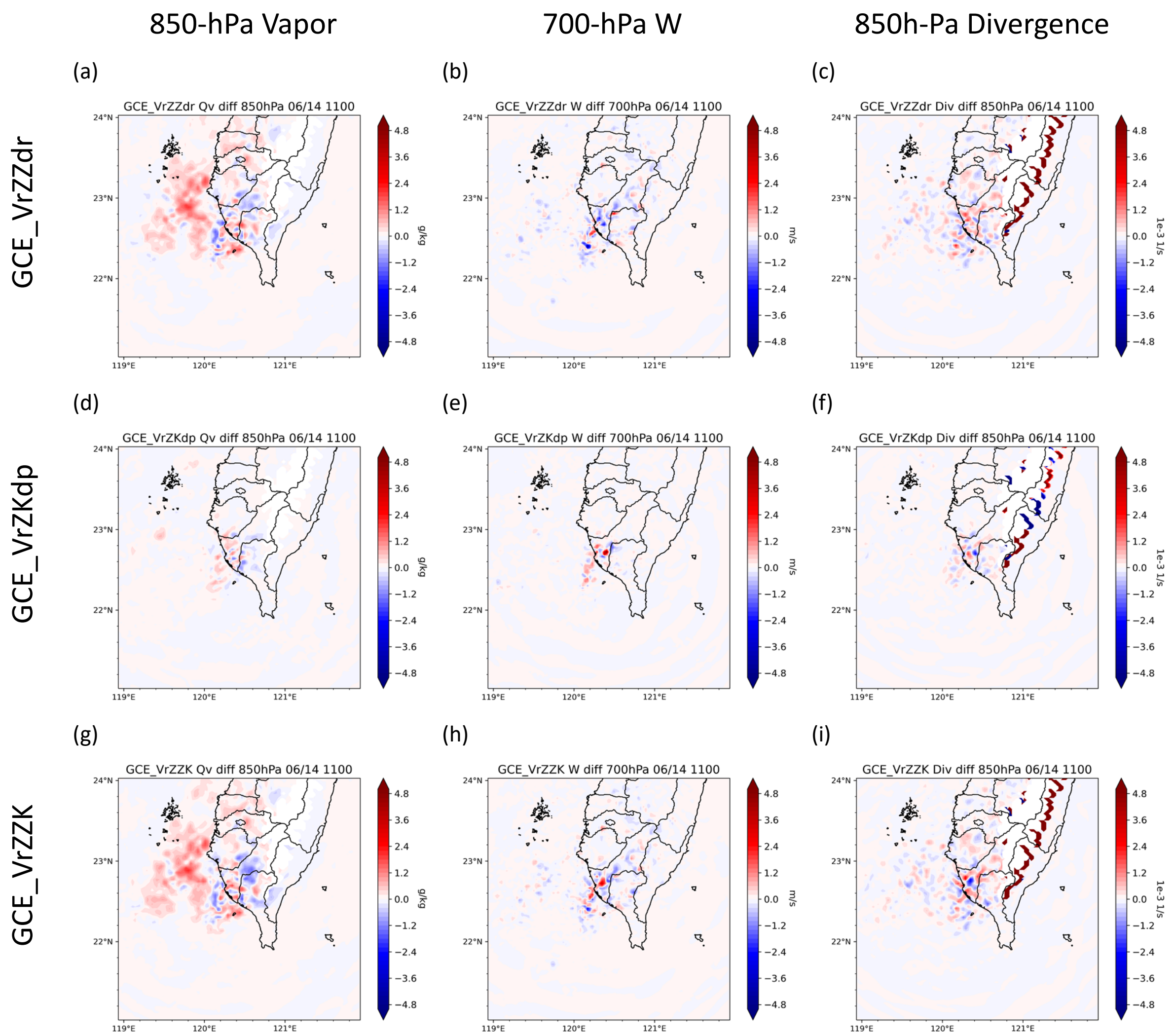

Figure 55 Analysis mean difference of 850-hPa water vapor, 700-hPa vertical velocity and 850-hPa divergence in the squall line experiments with GCE scheme at 1100 UTC 14th June 2008. GCE_VrZ is the reference.

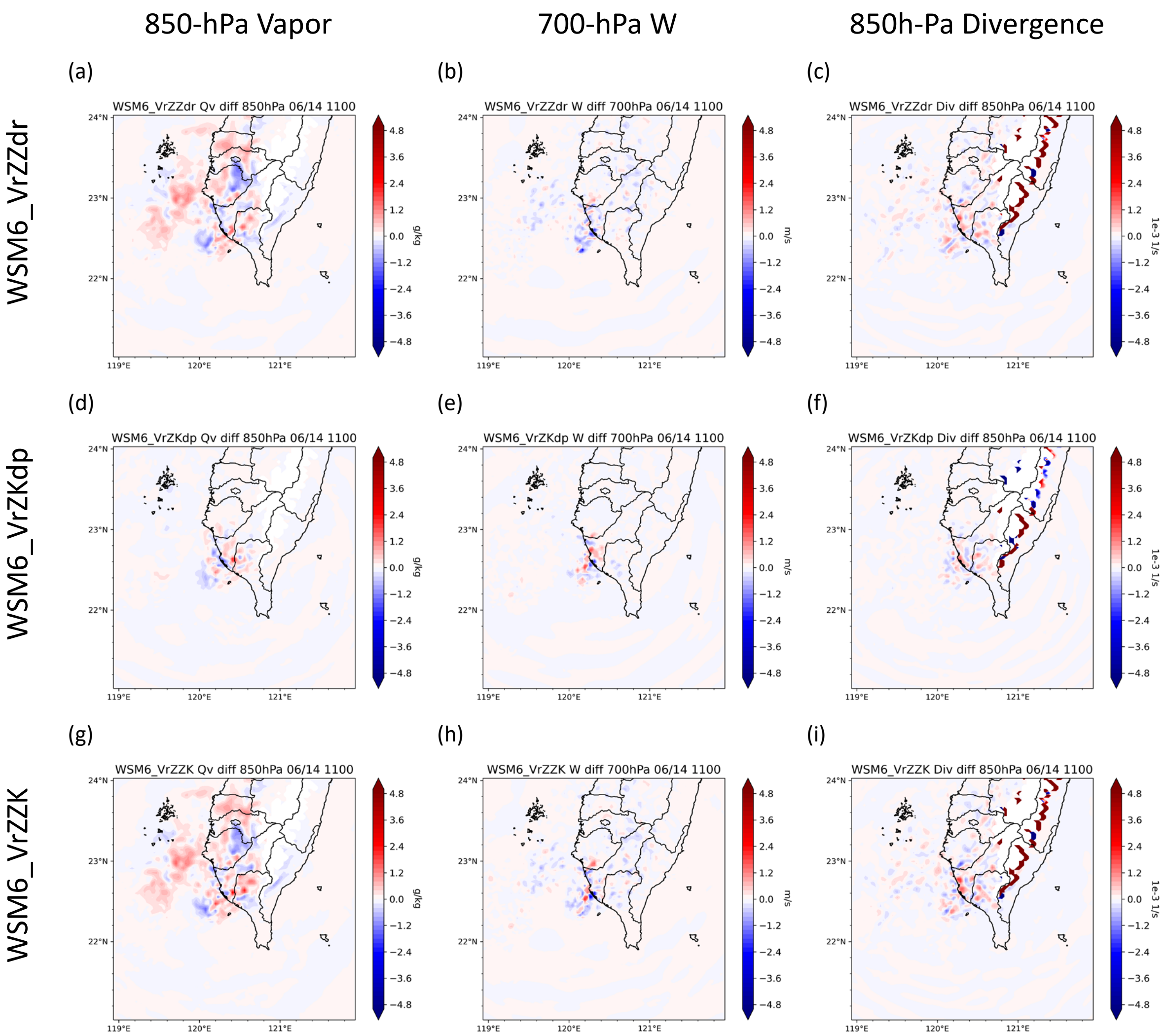

Figure 56 Analysis mean difference of 850-hPa water vapor, 700-hPa vertical velocity and 850-hPa divergence in the squall line experiments with WSM6 scheme at 1100 UTC 14th June 2008. WSM6_VrZ is the reference.

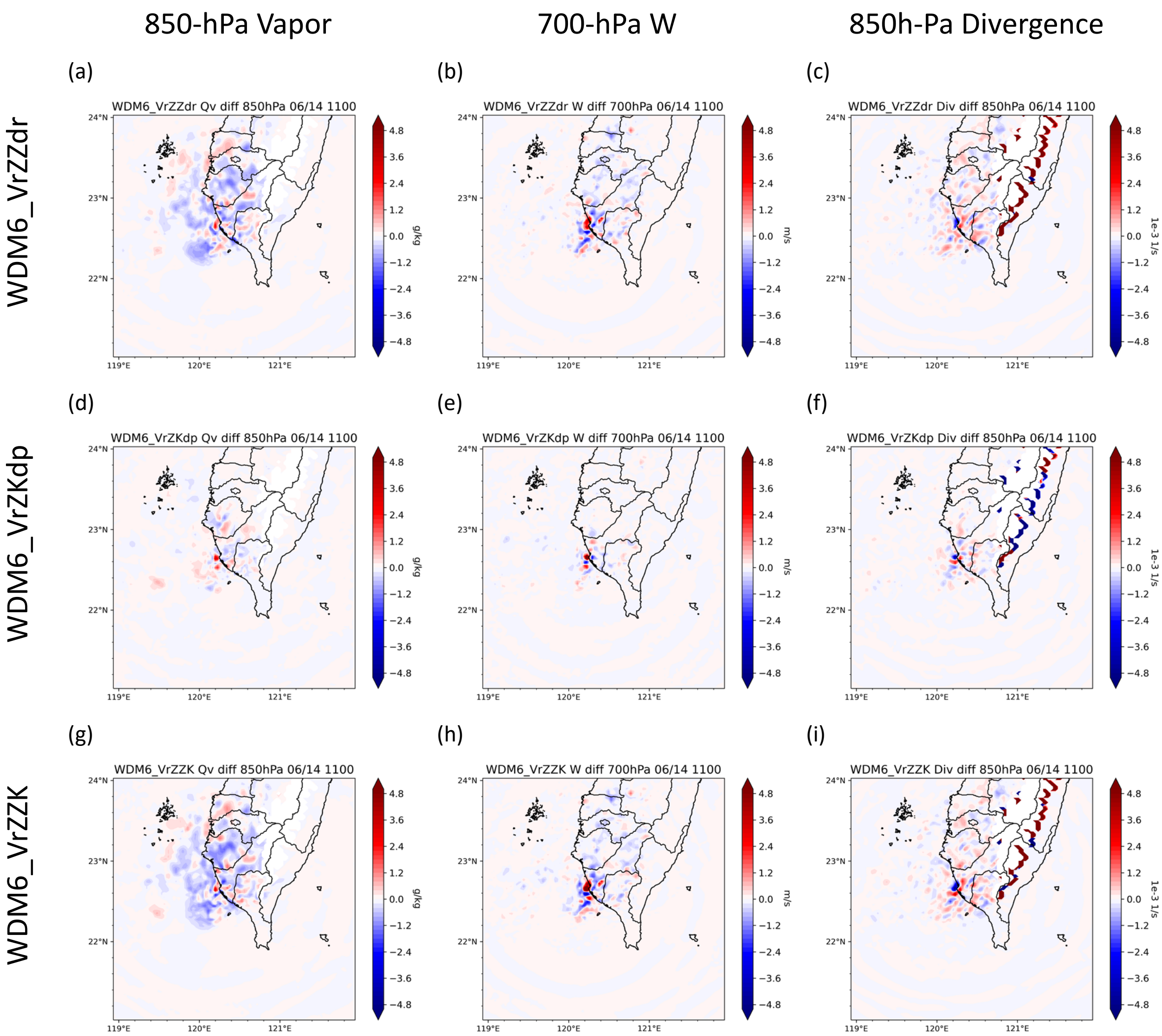

Figure 57 Analysis mean difference of 850-hPa water vapor, 700-hPa vertical velocity and 850-hPa divergence in the squall line experiments with WDM6 scheme at 1100 UTC 14th June 2008. WDM6_VrZ is the reference.

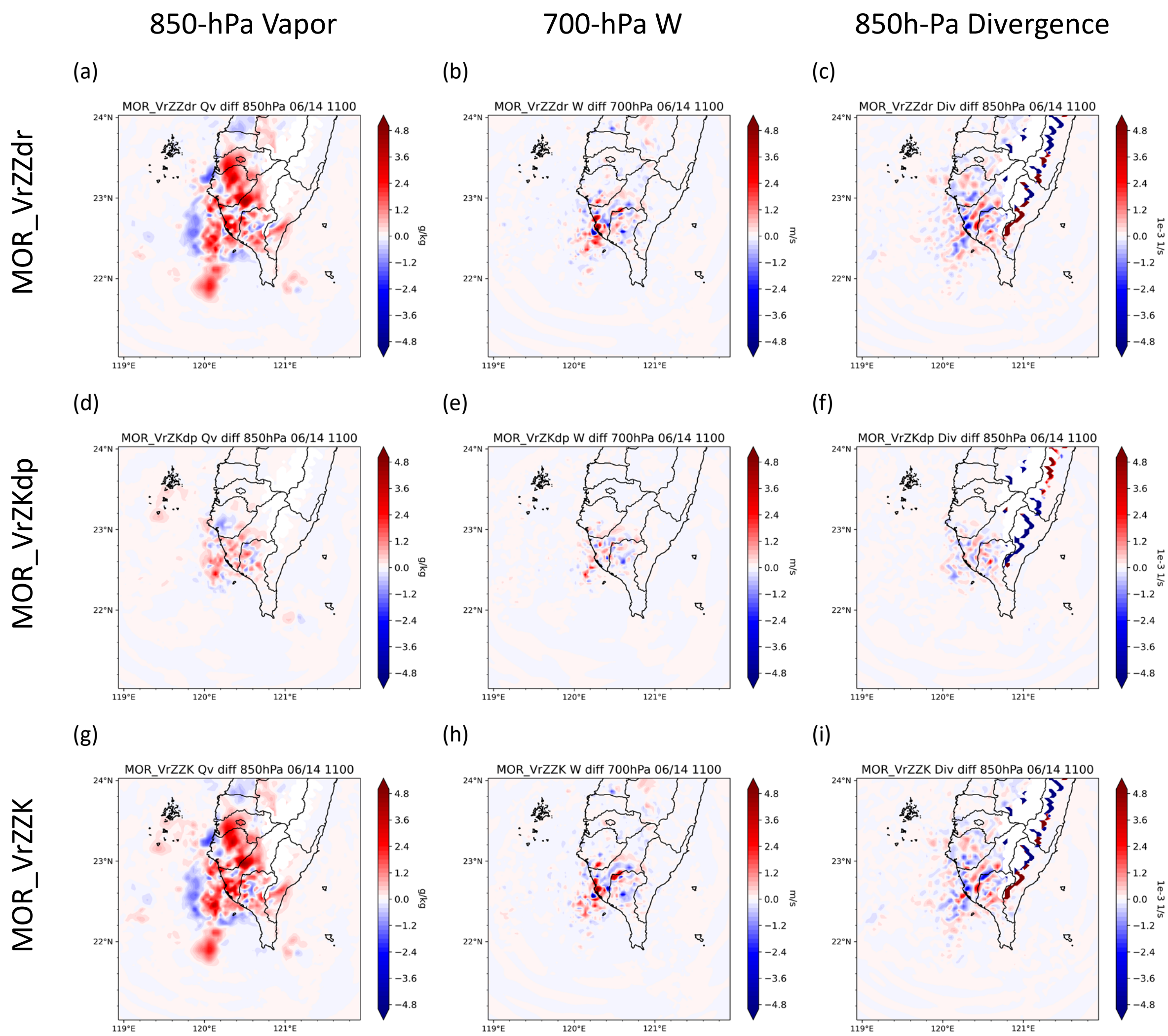

Figure 58 Analysis mean difference of 850-hPa water vapor, 700-hPa vertical velocity and 850-hPa divergence in the squall line experiments with MOR scheme at 1100 UTC 14th June 2008. MOR_VrZ is the reference.

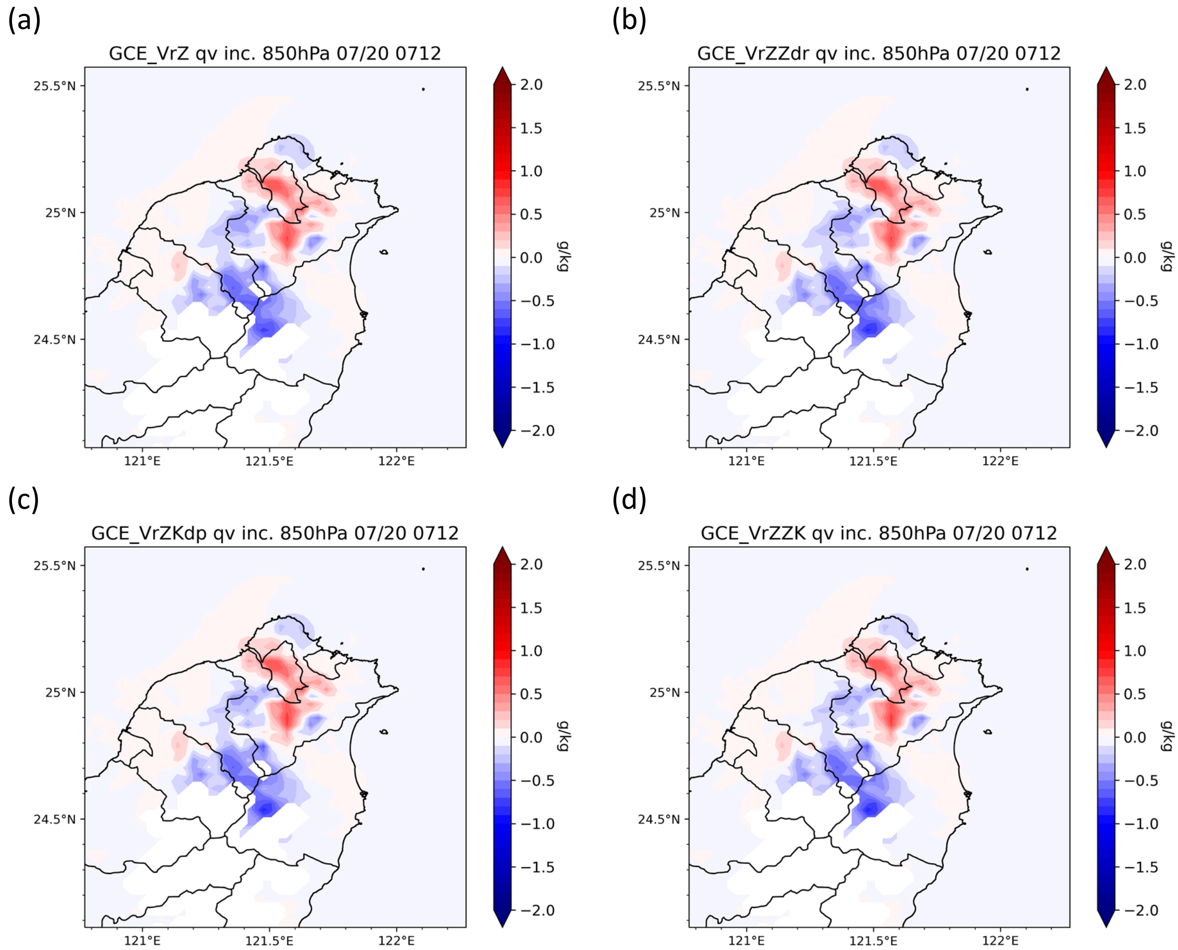

Figure 59 Water vapor increment at 850 hPa in the afternoon thunderstorm experiments with GCE scheme at 0712 UTC 20th July 2020. (a) GCE_VrZ (b) GCE_VrZZdr (c) GCE_VrZKdp (d) GCE_VrZZK

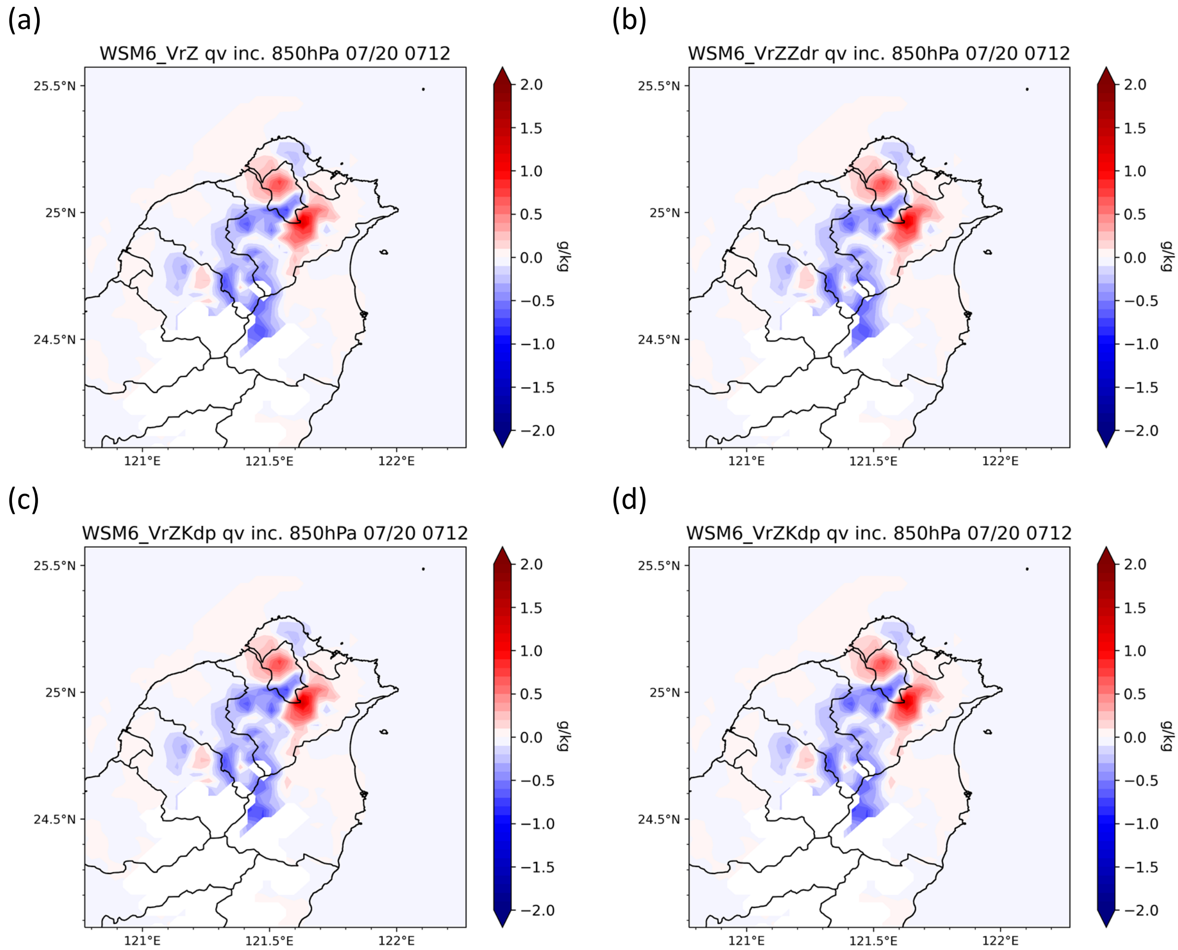

Figure 60 Water vapor increment at 850 hPa in the afternoon thunderstorm experiments with WSM6 scheme at 0712 UTC 20th July 2020. (a) WSM6_VrZ (b) WSM6_VrZZdr (c) WSM6_VrZKdp (d) WSM6_VrZZK.

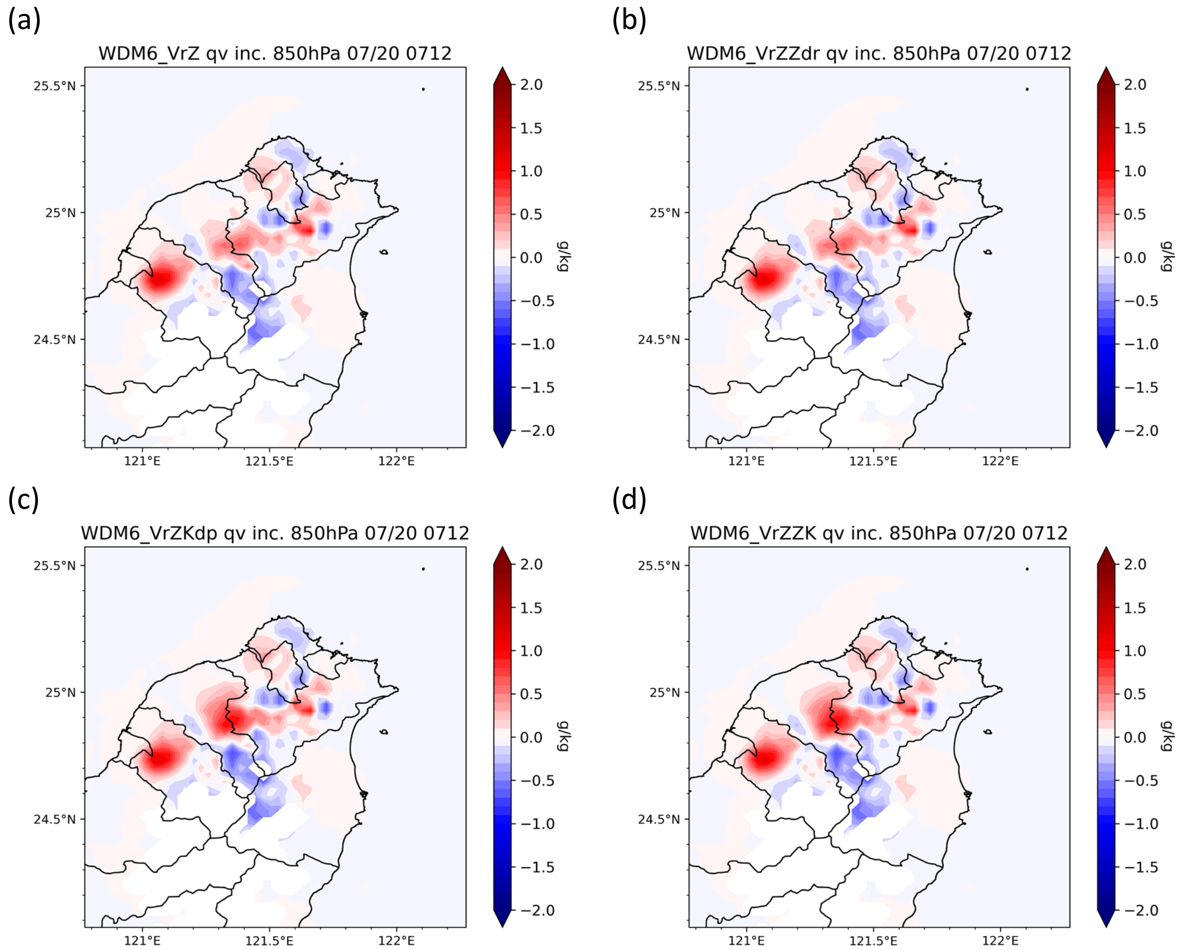

Figure 61 Water vapor increment at 850 hPa in the afternoon thunderstorm experiments with WDM6 scheme at 0712 UTC 20th July 2020. (a) WDM6_VrZ (b) WDM6_VrZZdr (c) WDM6_VrZKdp (d) WDM6_VrZZK.

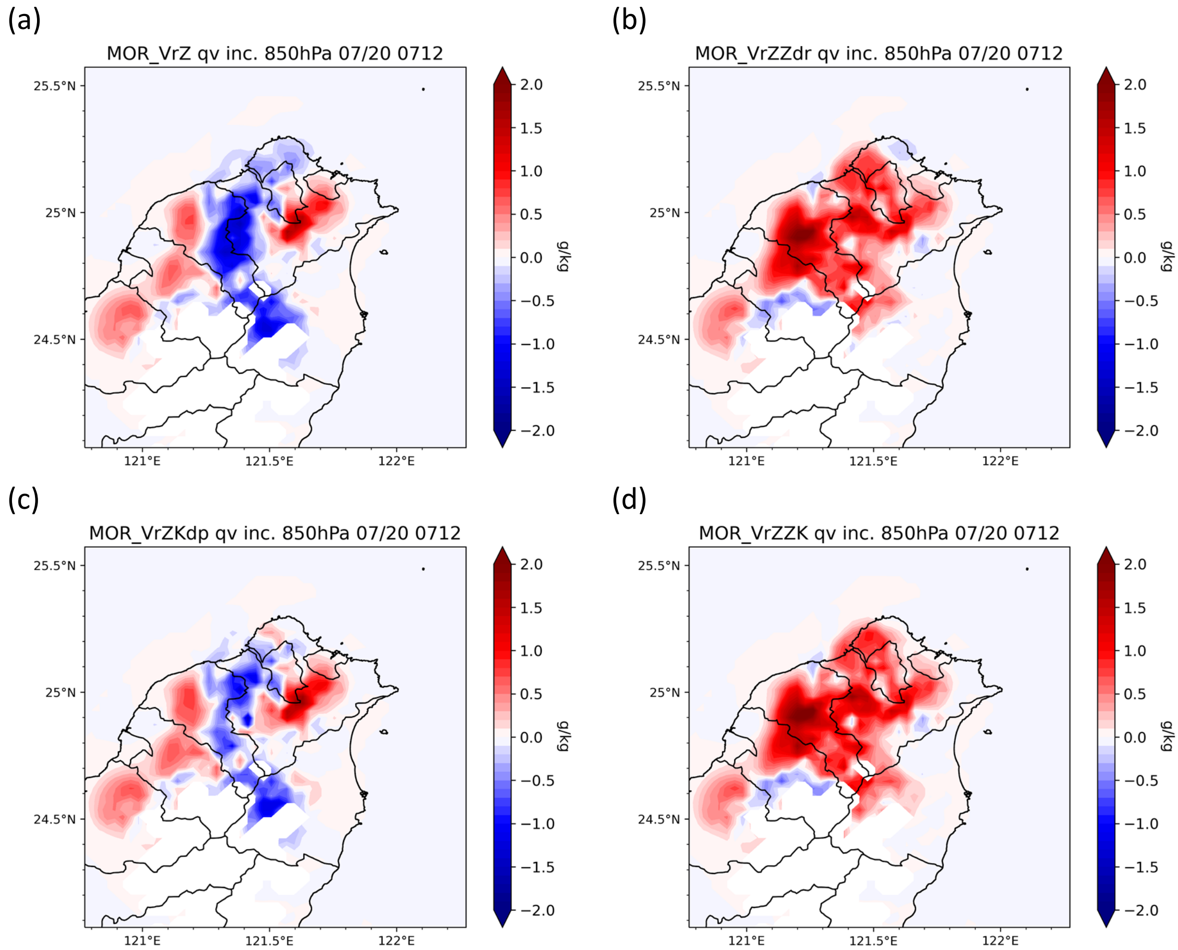

Figure 62 Water vapor increment at 850 hPa in the afternoon thunderstorm experiments with MOR scheme at 0712 UTC 20th July 2020. (a) MOR_VrZ (b) MOR_VrZZdr (c) MOR_VrZKdp (d) MOR_VrZZK.

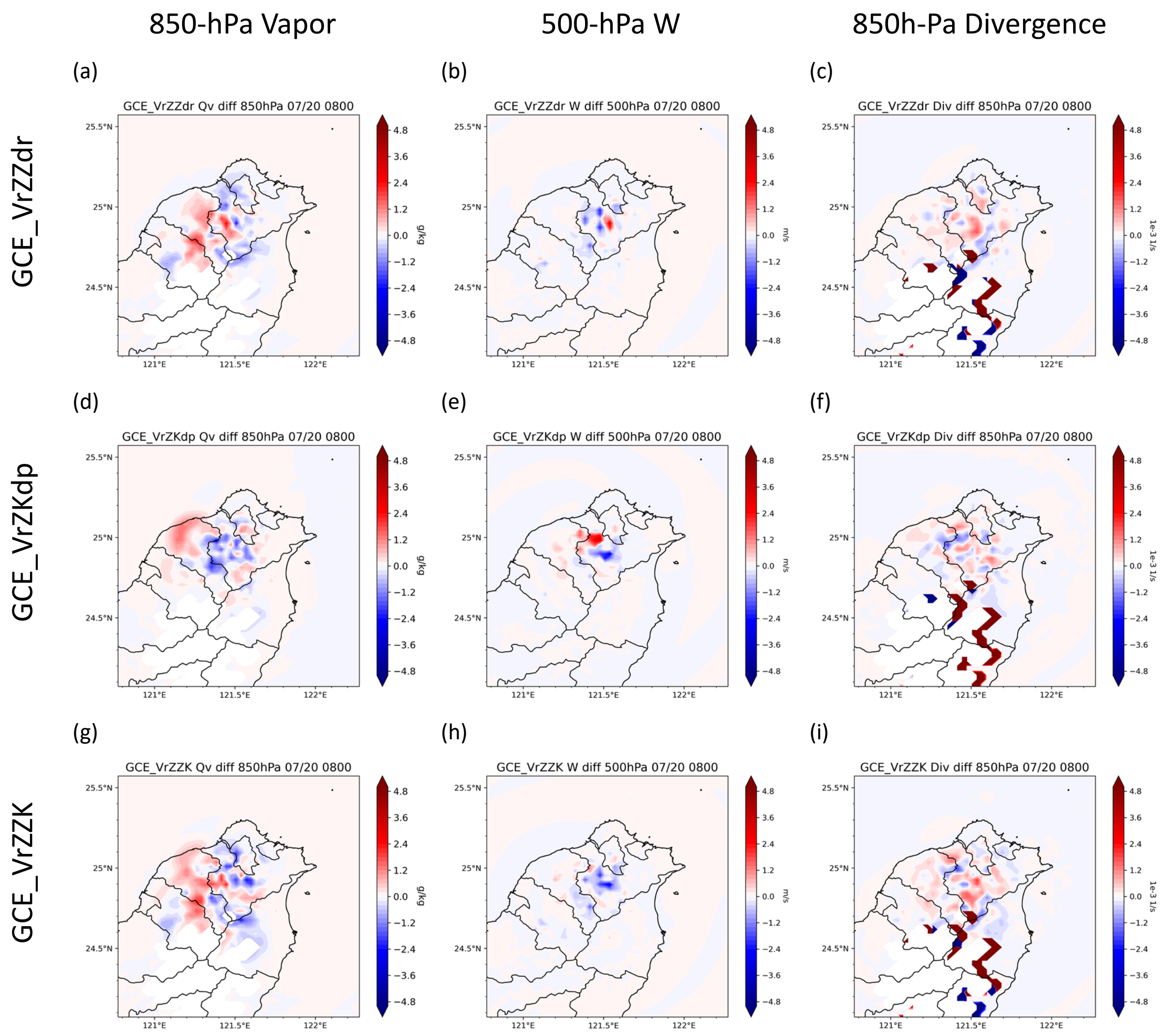

Figure 63 Analysis mean difference of 850-hPa water vapor, 500-hPa vertical velocity and 850-hPa divergence in the squall line experiments with GCE scheme at 0800 UTC 20th July 2020. GCE_VrZ is the reference.

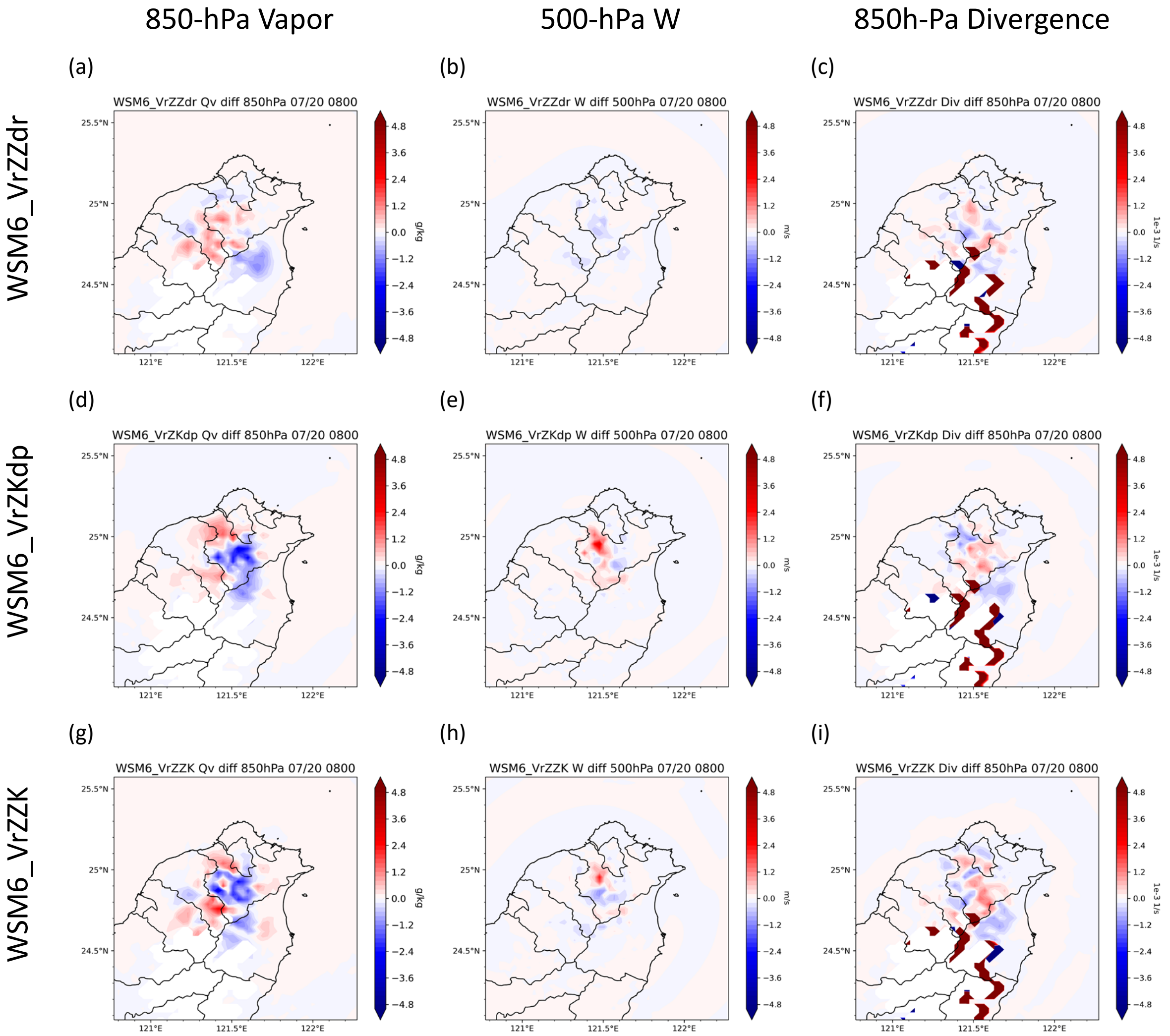

Figure 64 Analysis mean difference of 850-hPa water vapor, 500-hPa vertical velocity and 850-hPa divergence in the squall line experiments with WSM6 scheme at 0800 UTC 20th July 2020. WSM6_VrZ is the reference.

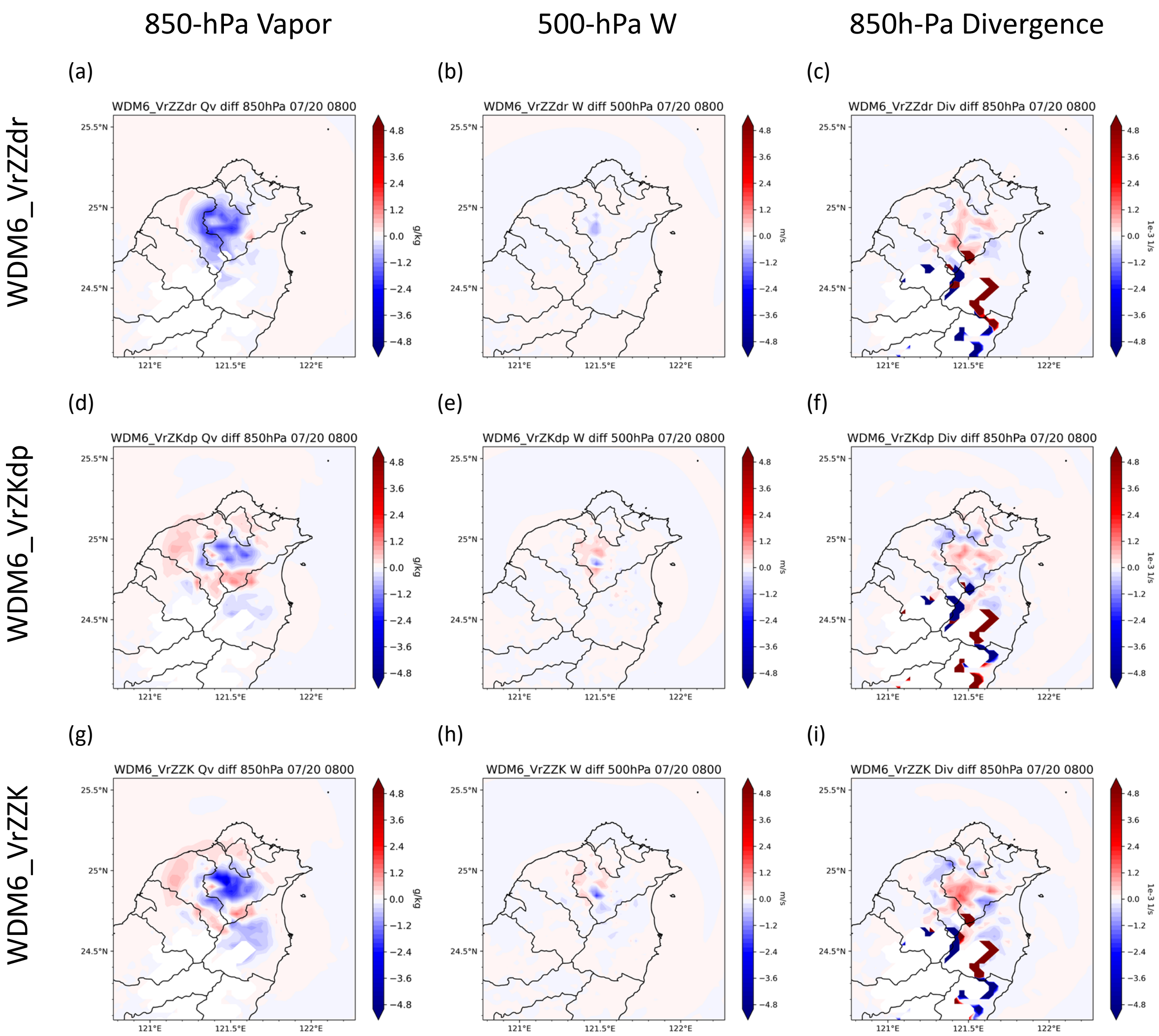

Figure 65 Analysis mean difference of 850-hPa water vapor, 500-hPa vertical velocity and 850-hPa divergence in the squall line experiments with WDM6 scheme at 0800 UTC 20th July 2020. WDM6_VrZ is the reference.

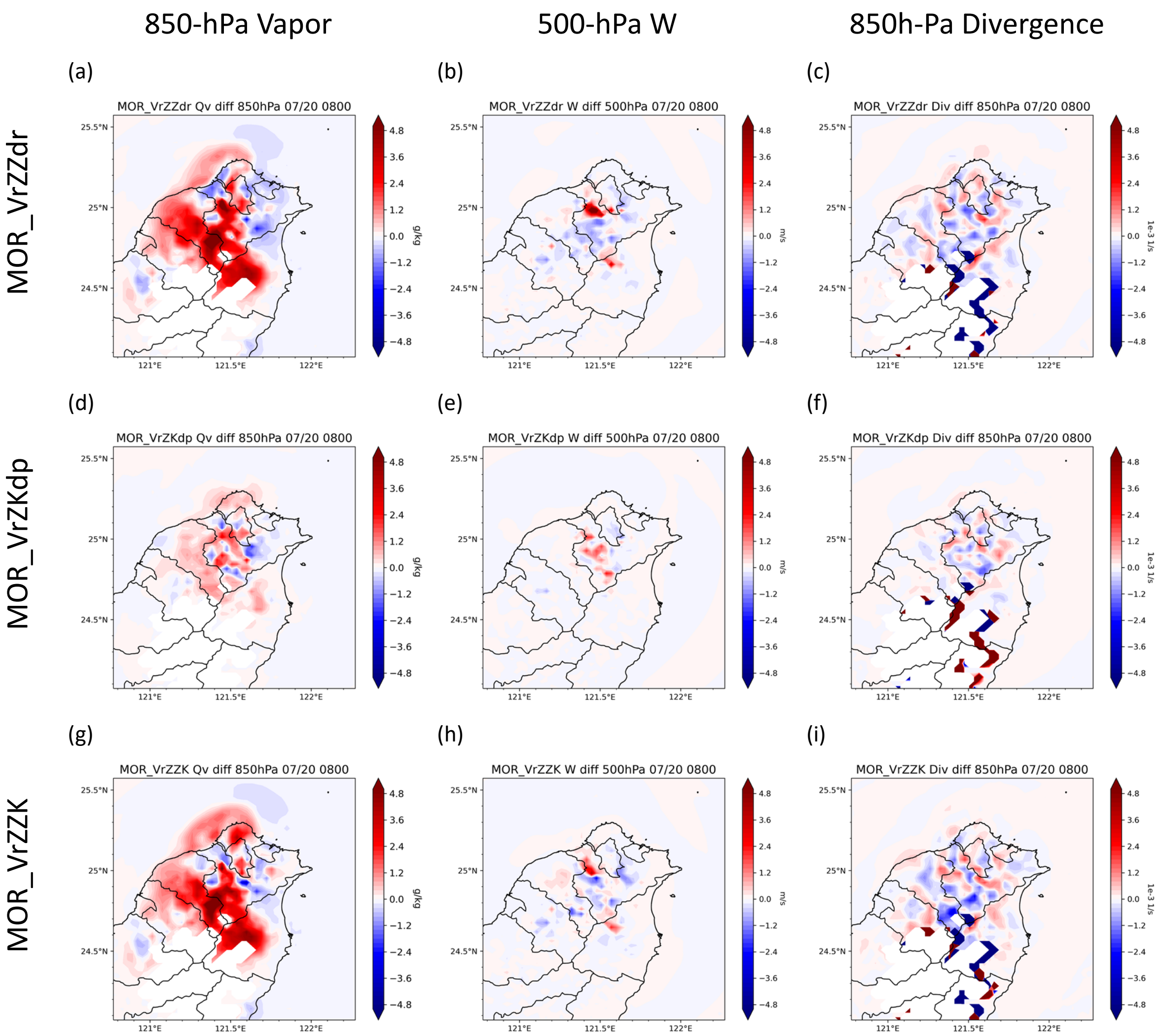

Figure 66 Analysis mean difference of 850-hPa water vapor, 500-hPa vertical velocity and 850-hPa divergence in the squall line experiments with MOR scheme at 0800 UTC 20th July 2020. MOR_VrZ is the reference.

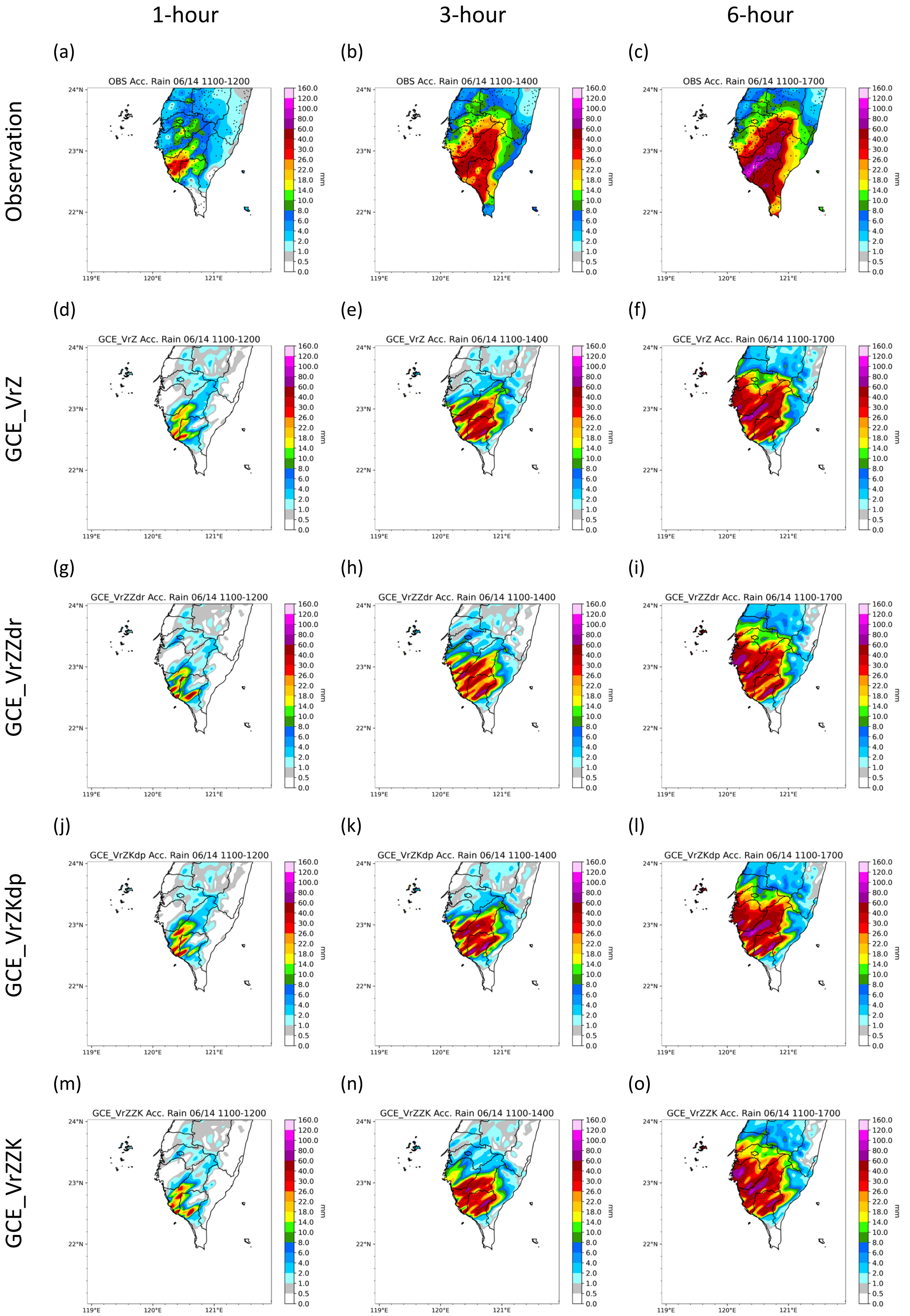

Figure 67 1-hour, 3-hour and 6-hour accumulated rainfall observation and analysis mean QPF after data assimilation in the squall line experiments with GCE scheme.

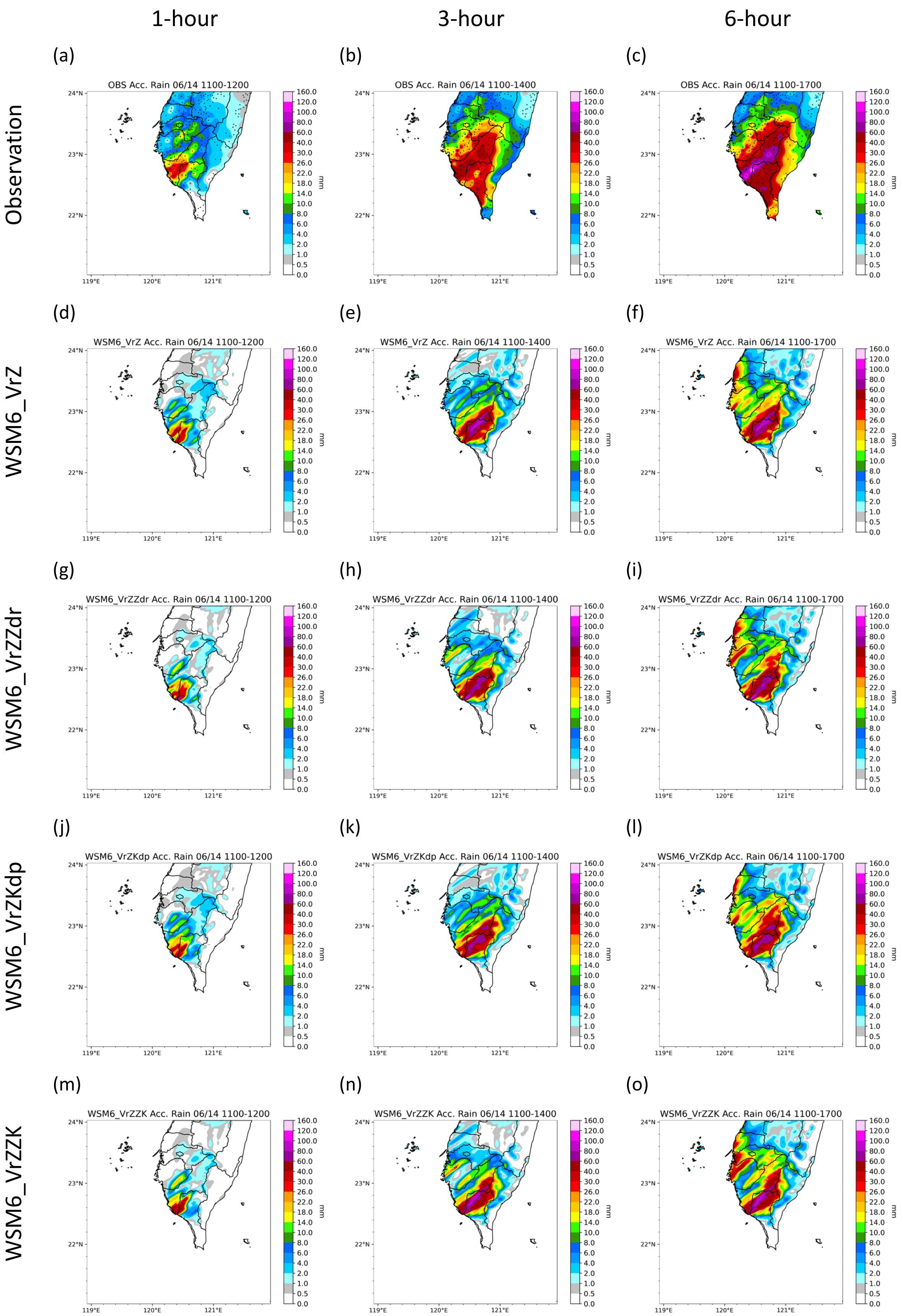

Figure 68 1-hour, 3-hour and 6-hour accumulated rainfall observation and analysis mean QPF after data assimilation in the squall line experiments with WSM6 scheme.

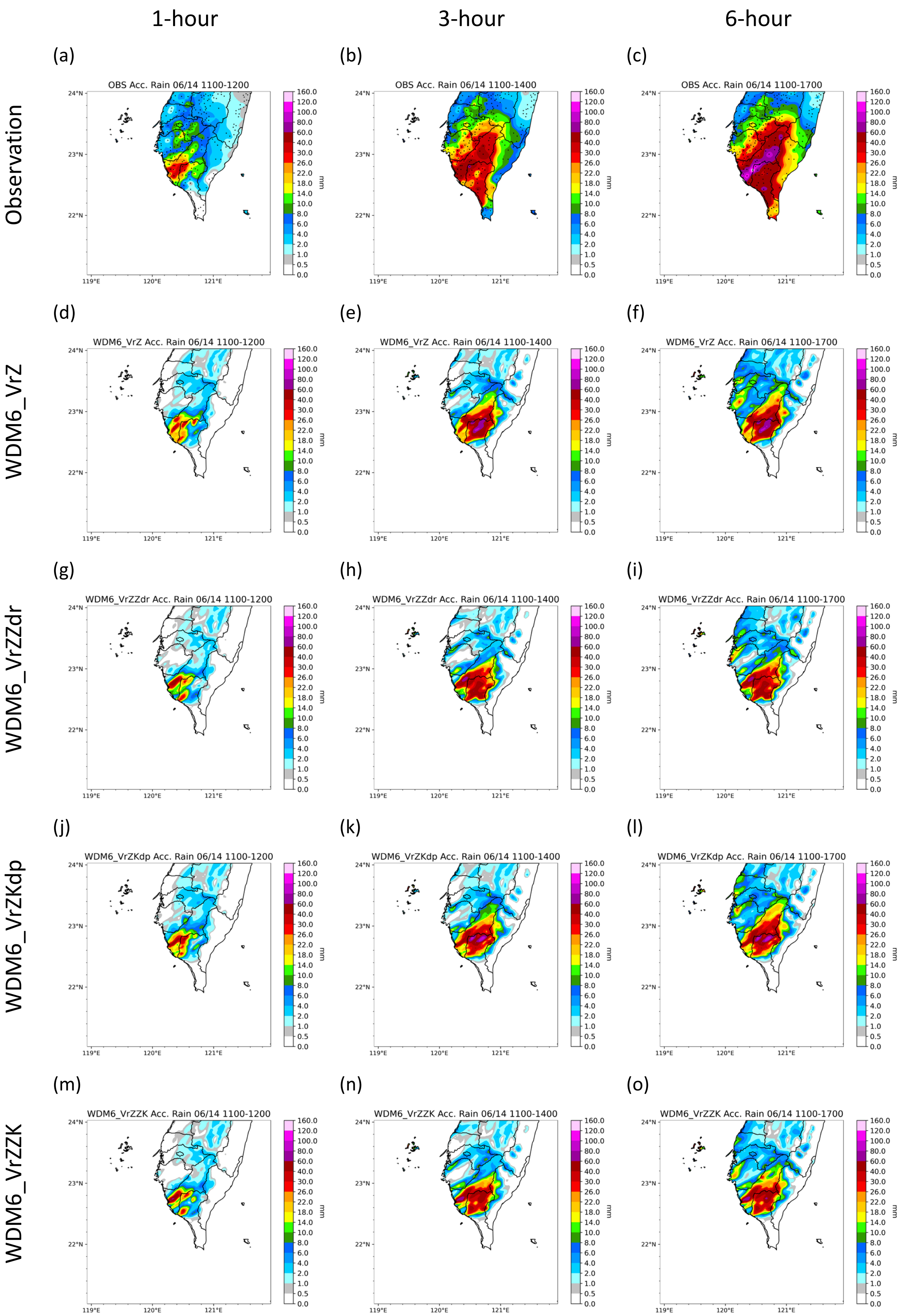

Figure 69 1-hour, 3-hour and 6-hour accumulated rainfall observation and analysis mean QPF after data assimilation in the squall line experiments with WDM6 scheme.

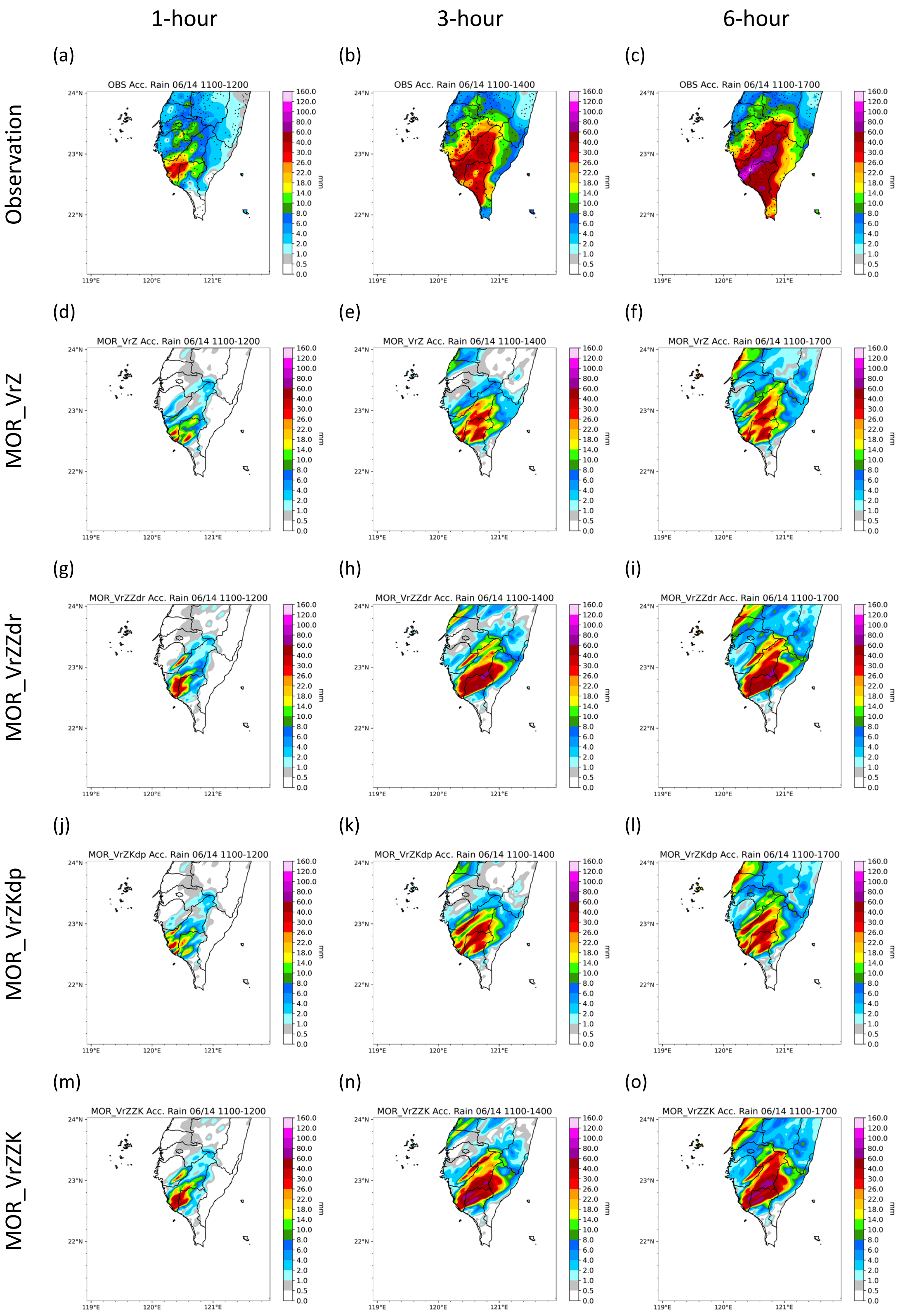

Figure 70 1-hour, 3-hour and 6-hour accumulated rainfall observation and analysis mean QPF after data assimilation in the squall line experiments with MOR scheme.

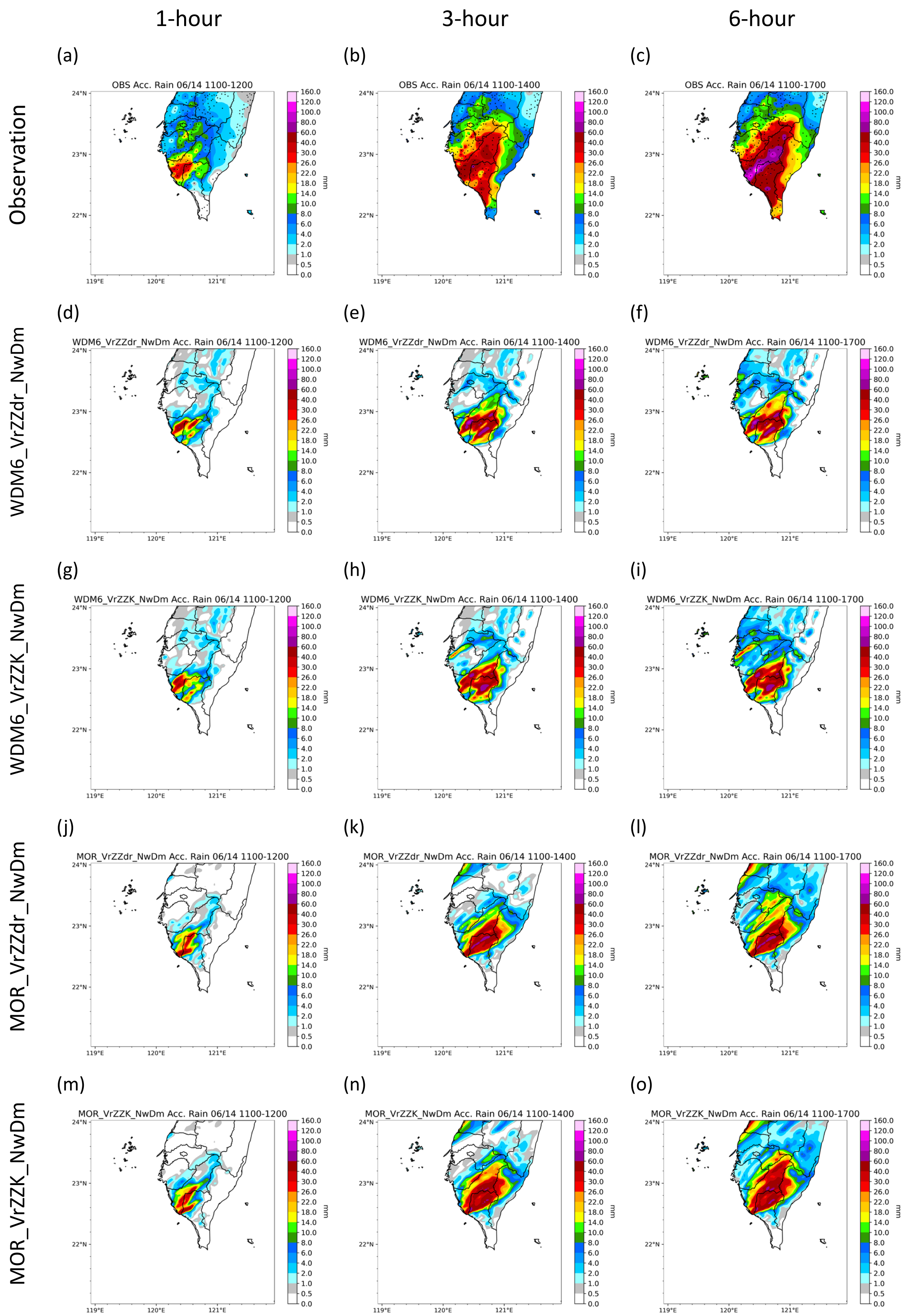

Figure 71 1-hour, 3-hour and 6-hour accumulated rainfall observation and analysis mean QPF after data assimilation in the squall line experiments with the new approach.

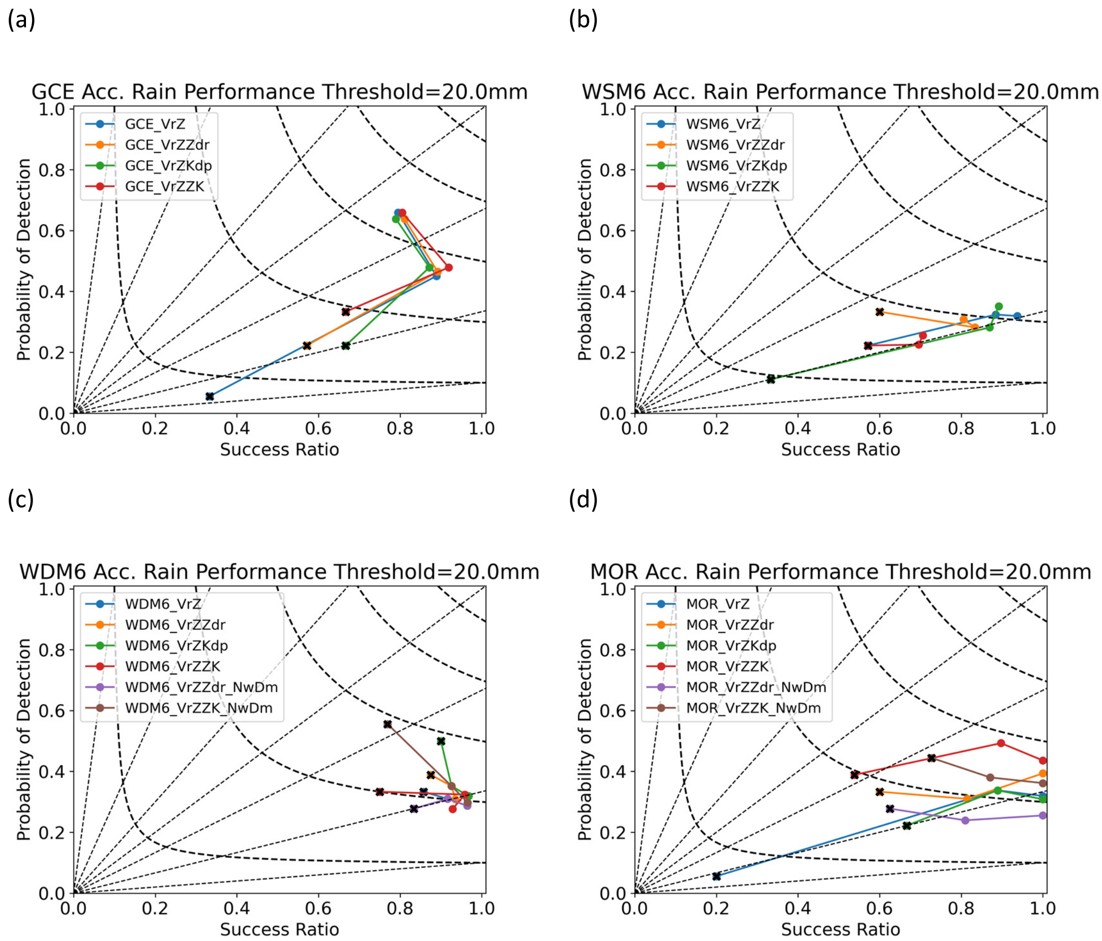

Figure 72 Performance diagrams of 1-hour, 3-hour and 6-hour accumulated rainfall exceeding 20 mm in the squall line case. The black cross indicates the 1st hour. (a) GCE (b) WSM6 (c) WDM6 (d) MOR.

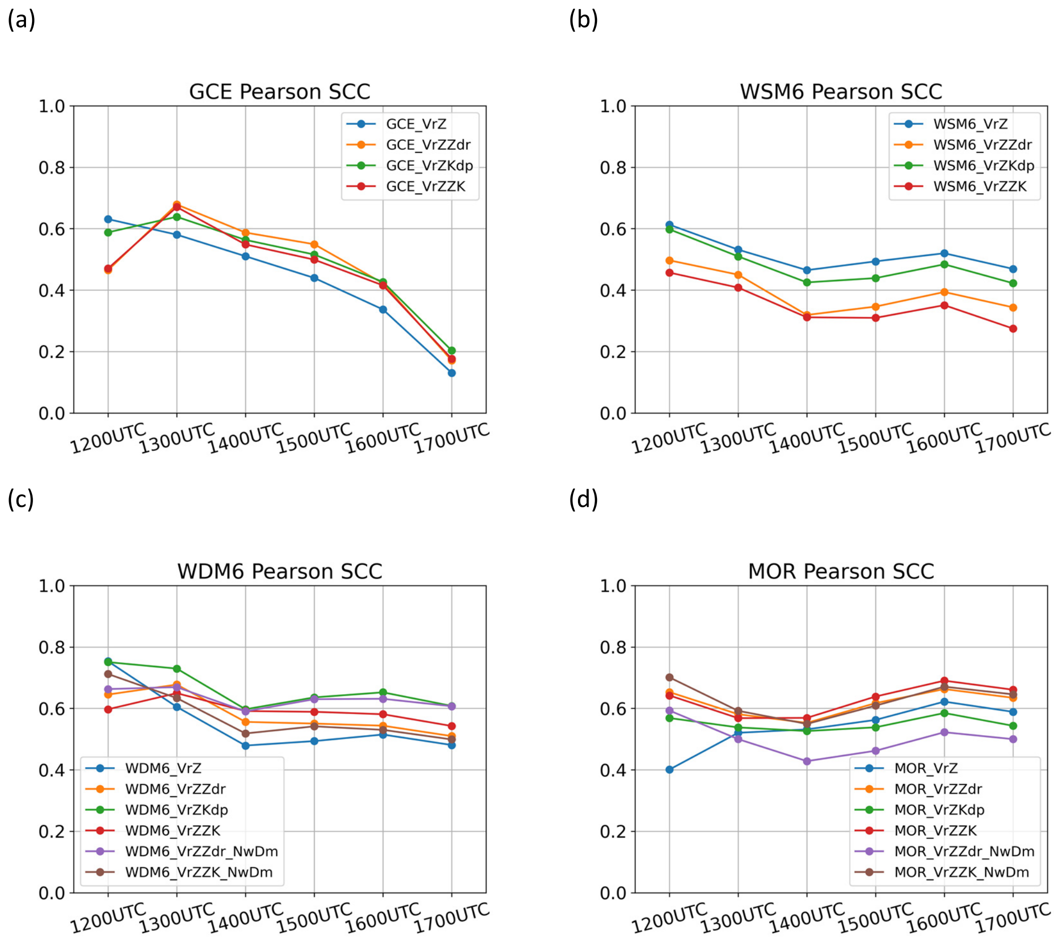

Figure 73 Pearson spatial correlation coefficient time series of 6-hour accumulated rainfall in the squall line case. (a) GCE (b) WSM6 (c) WDM6 (d) MOR.

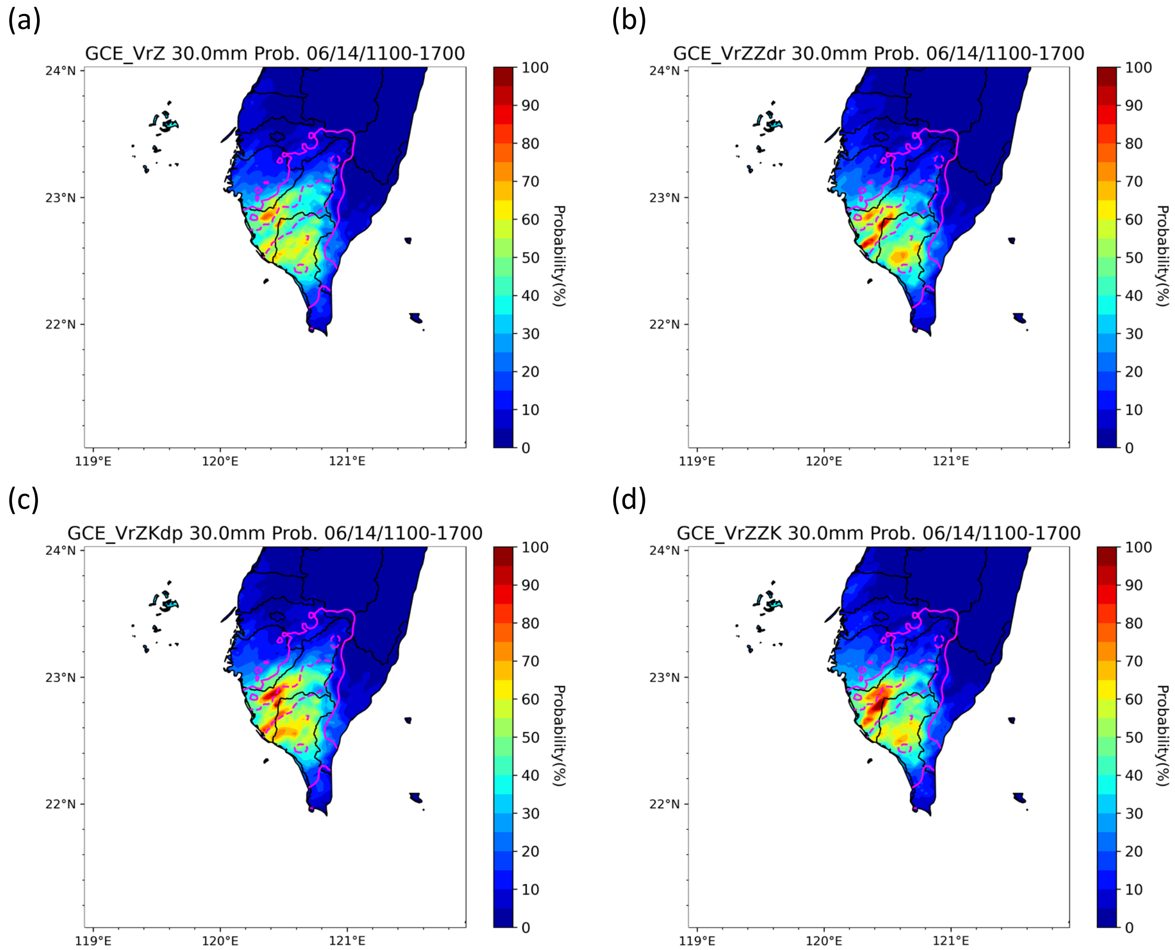

Figure 74 Probability of 6-hour accumulated rainfall exceeding 30 mm in the squall line experiments with GCE scheme. The solid contour and the dashed contour represent 30-mm and 60-mm contours respectively.

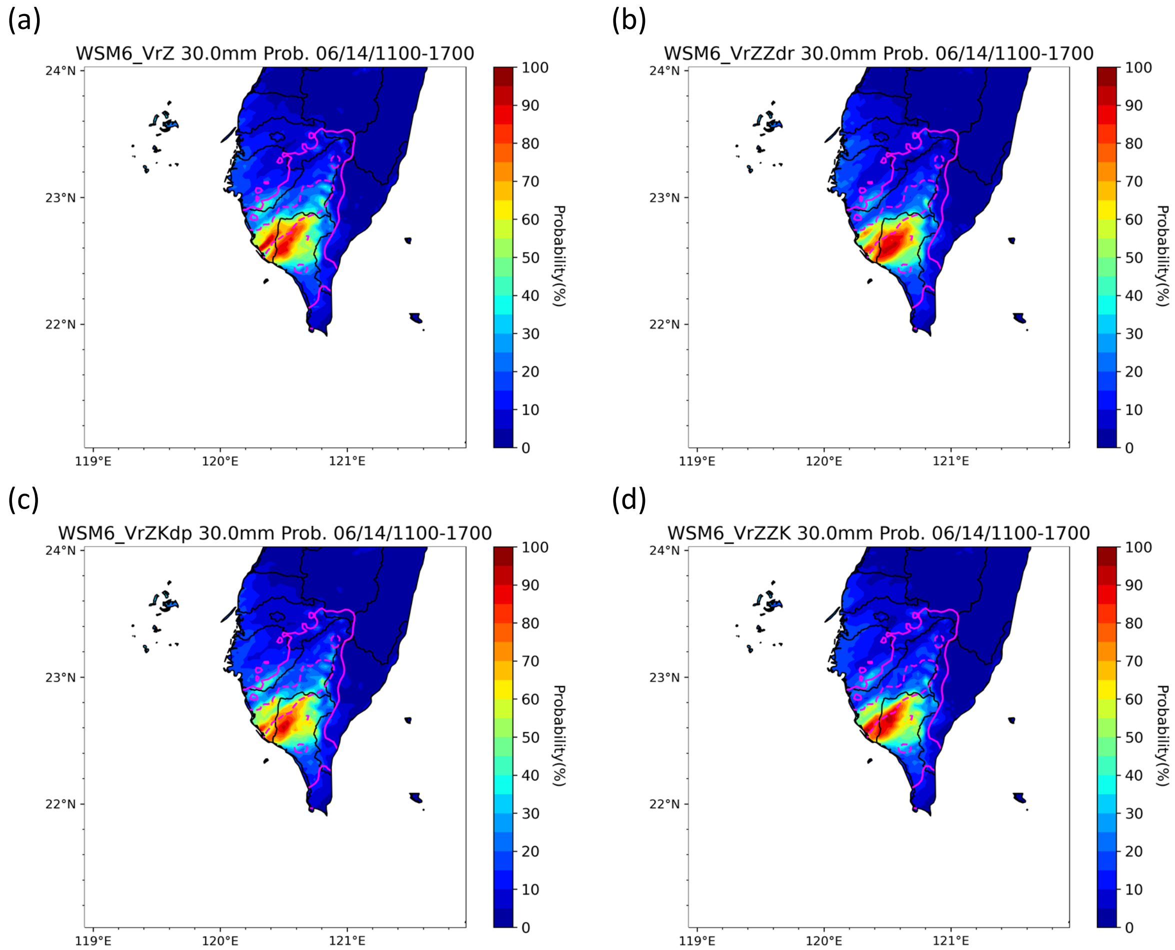

Figure 75 Probability of 6-hour accumulated rainfall exceeding 30 mm in the squall line experiments with WSM6 scheme. The solid contour and the dashed contour represent 30-mm and 60-mm contours respectively.

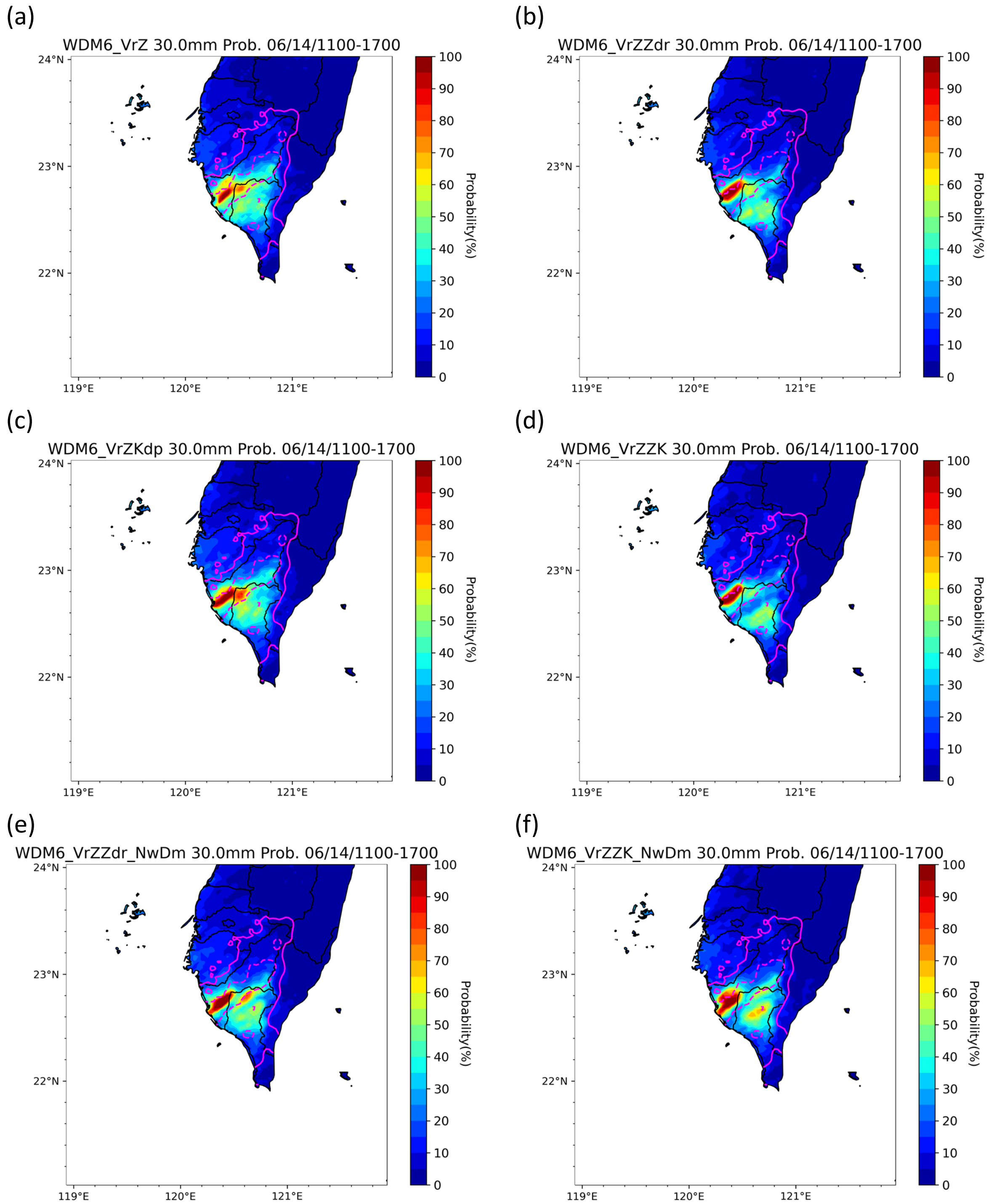

Figure 76 Probability of 6-hour accumulated rainfall exceeding 30 mm in the squall line experiments with WDM6 scheme. The solid contour and the dashed contour represent 30-mm and 60-mm contours respectively.

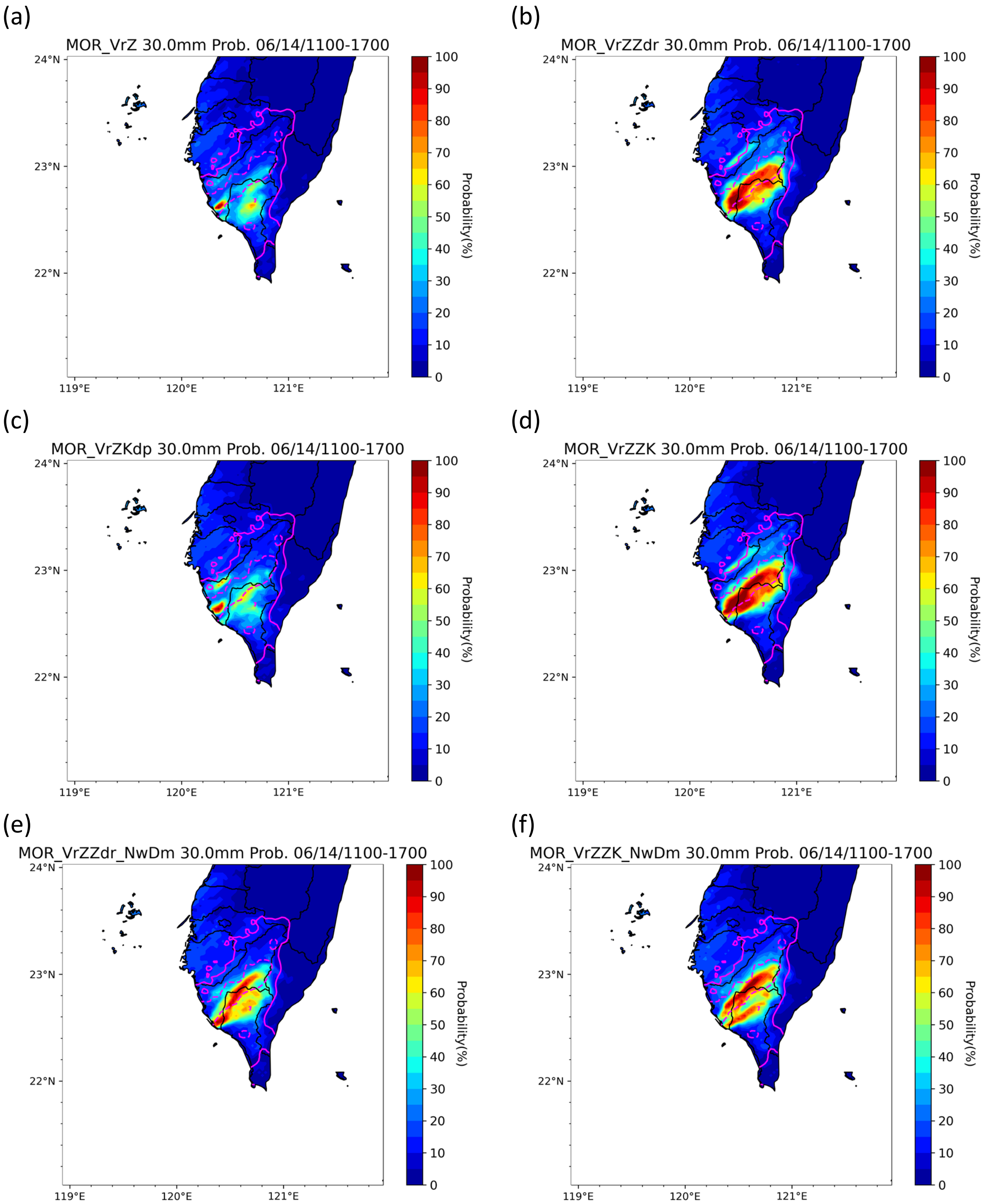

Figure 77 Probability of 6-hour accumulated rainfall exceeding 30 in the squall line experiments with MOR scheme. The solid contour and the dashed contour represent 30-mm and 60-mm contours respectively.

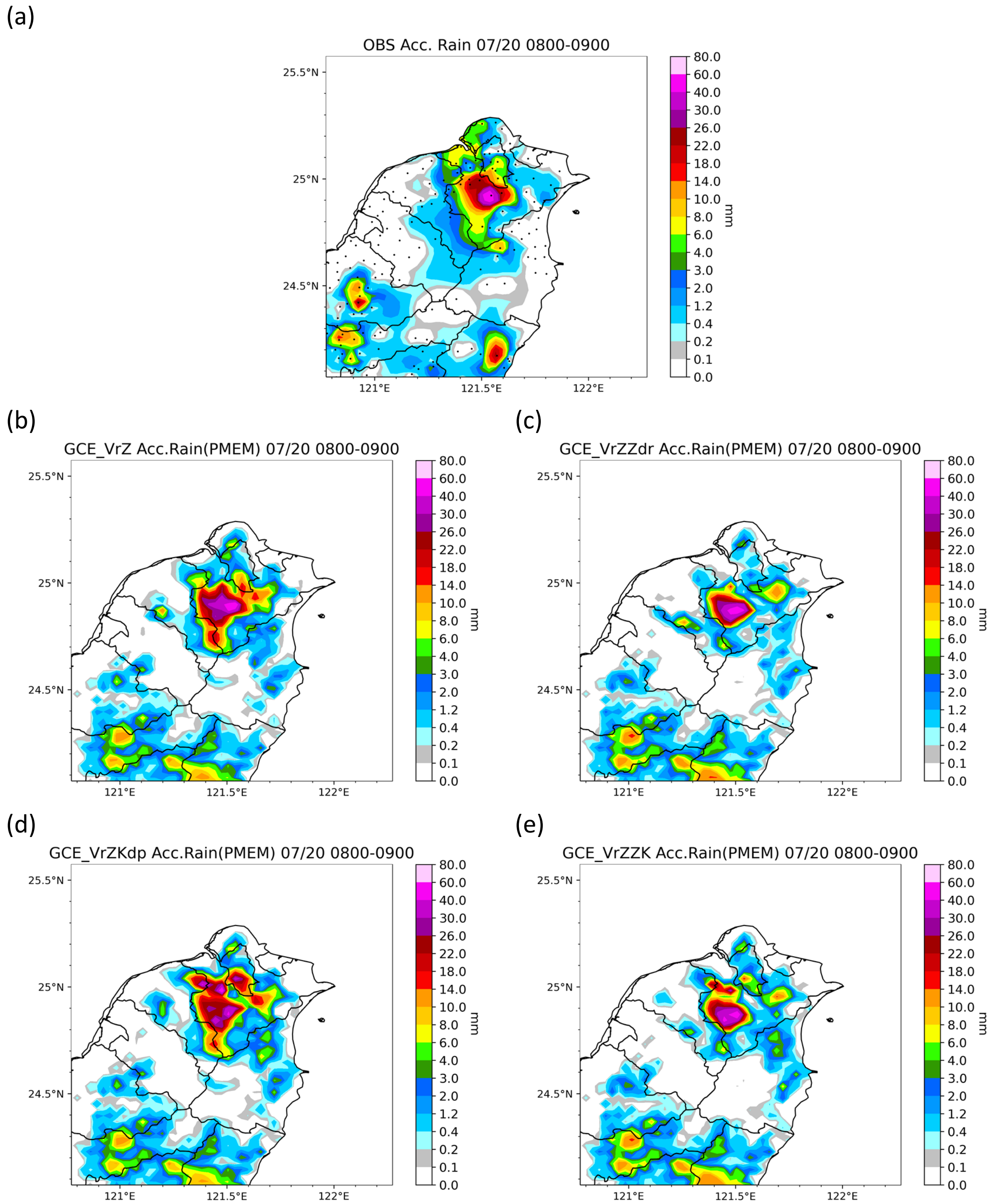

Figure 78 1-hour accumulated rainfall of observation and PMEM of the short-term ensemble QPF after data assimilation in the afternoon thunderstorm experiments with GCE scheme.

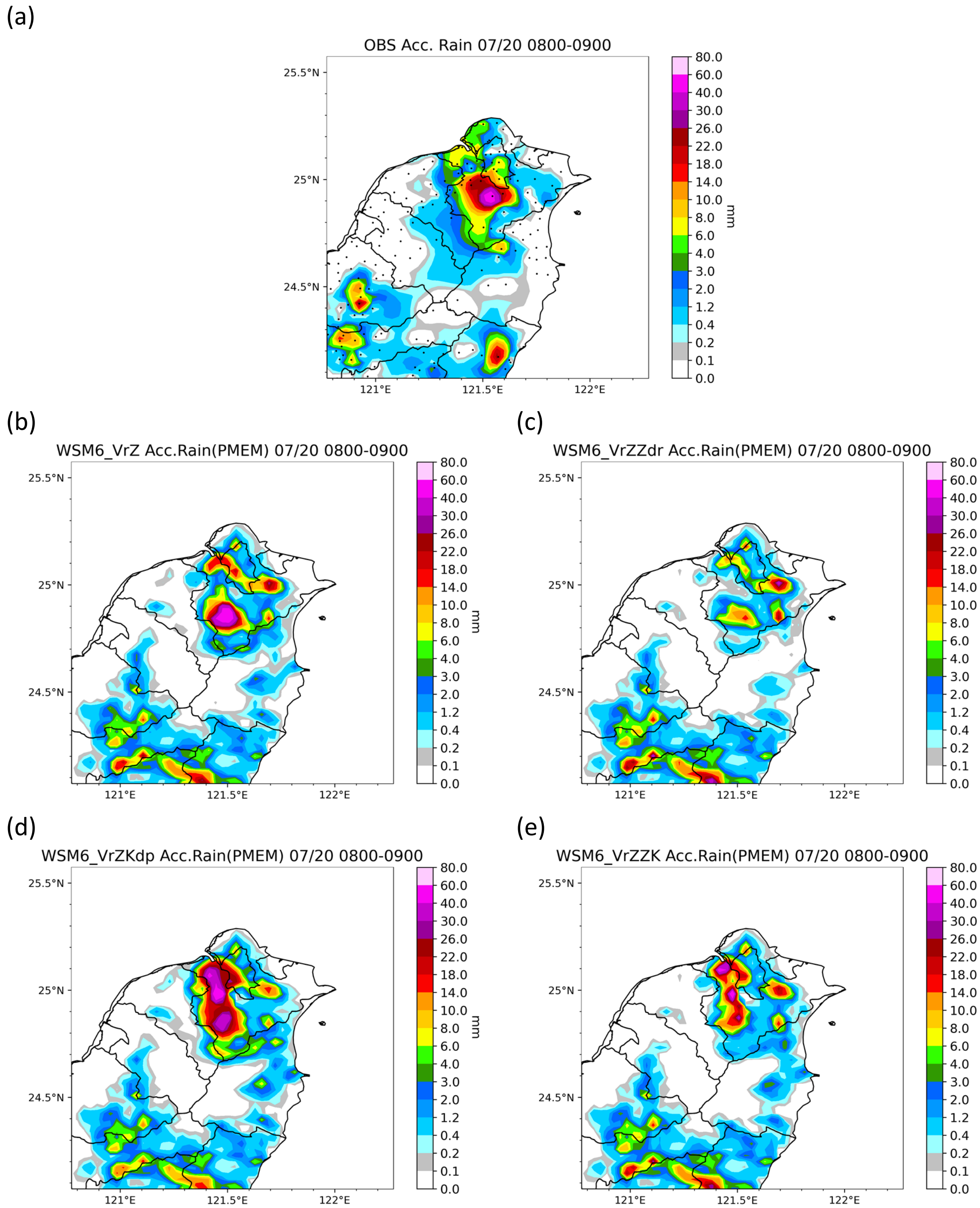

Figure 79 1-hour accumulated rainfall of observation and PMEM of the short-term ensemble QPF after data assimilation in the afternoon thunderstorm experiments with WSM6 scheme.

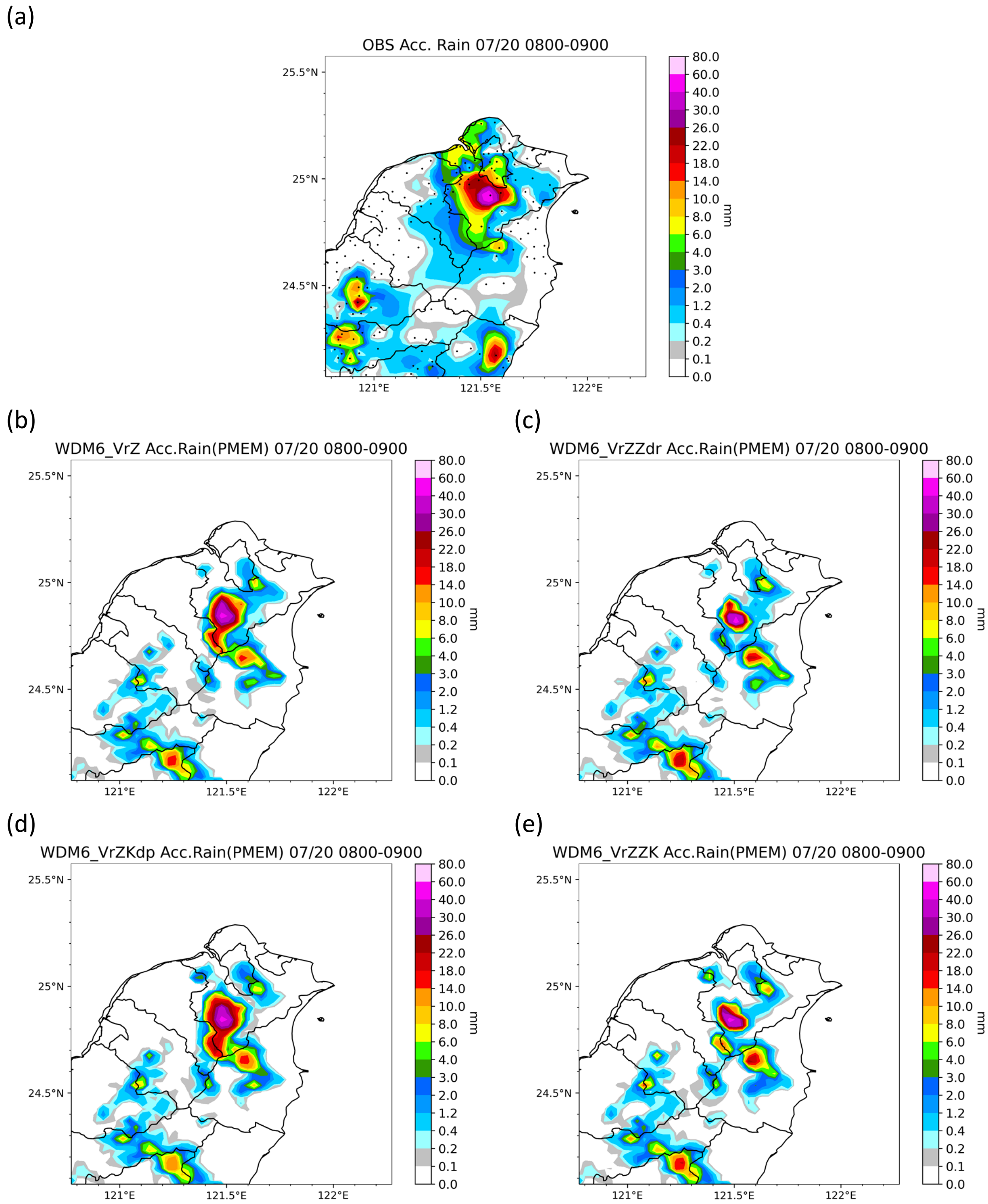

Figure 80 1-hour accumulated rainfall of observation and PMEM of the short-term ensemble QPF after data assimilation in the afternoon thunderstorm experiments with WDM6 scheme.

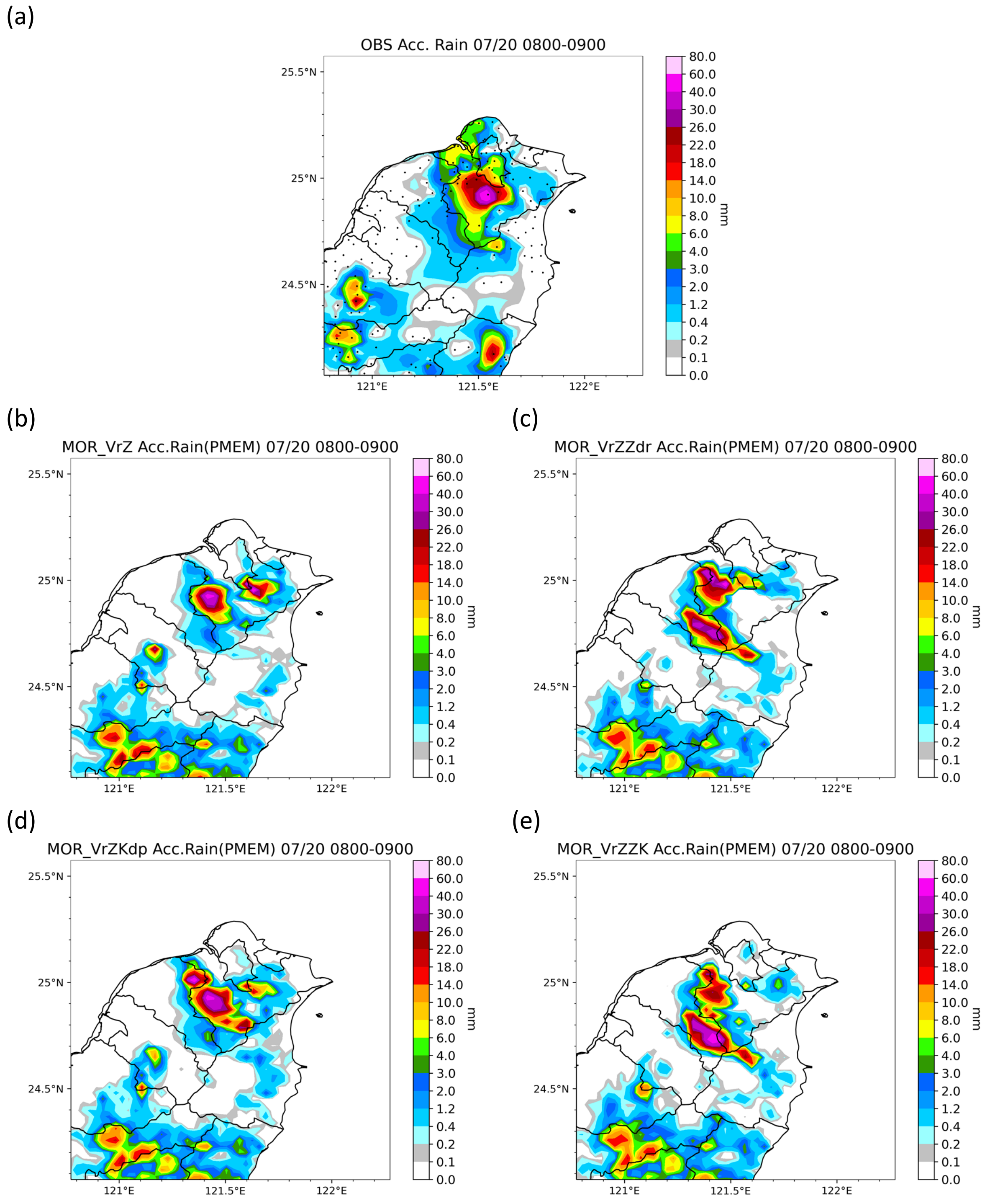

Figure 81 1-hour accumulated rainfall of observation and PMEM of the short-term ensemble QPF after data assimilation in the afternoon thunderstorm experiments with MOR scheme.

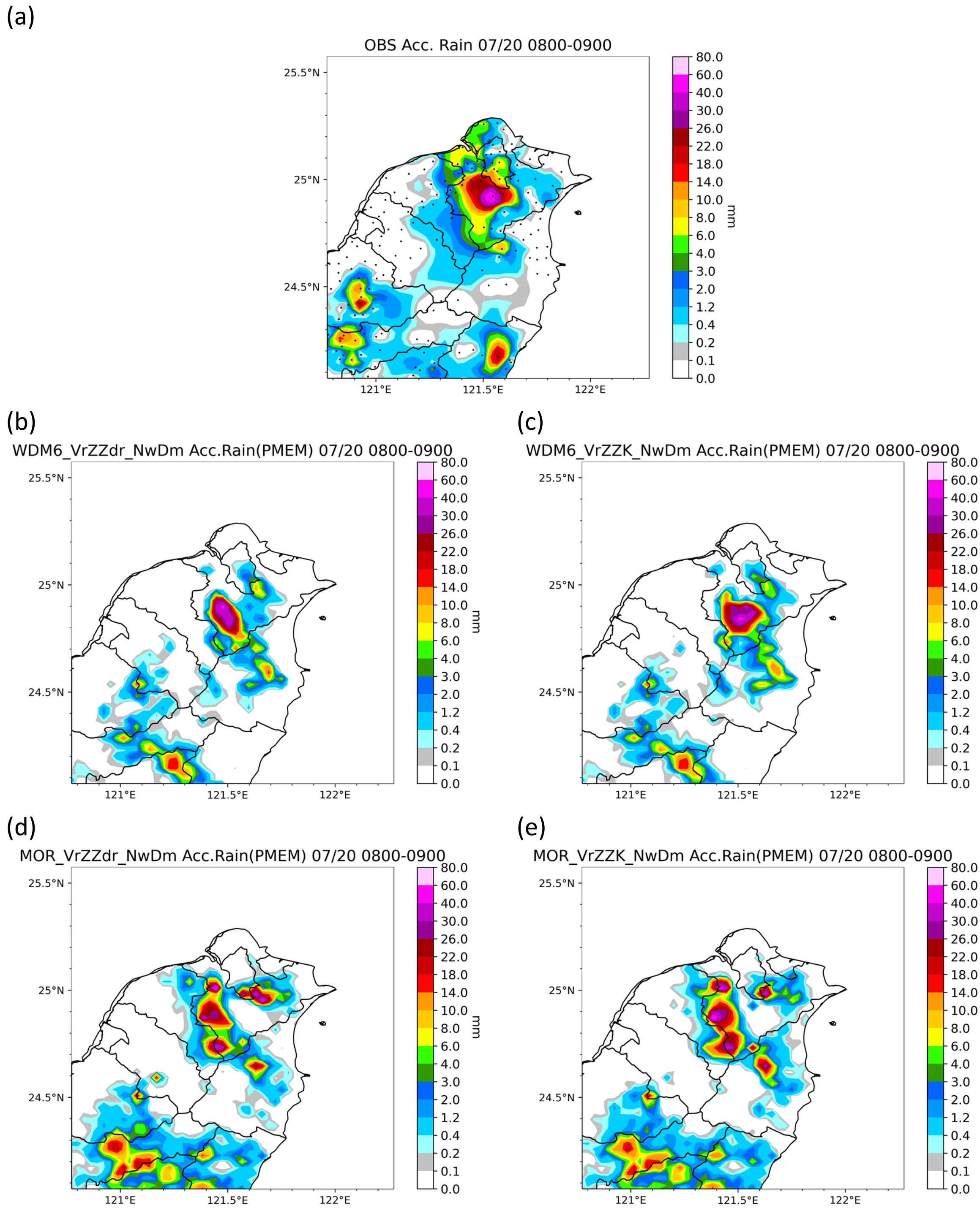

Figure 82 1-hour accumulated rainfall of observation and PMEM of the short-term ensemble QPF after data assimilation in the afternoon thunderstorm experiments with the new approach.

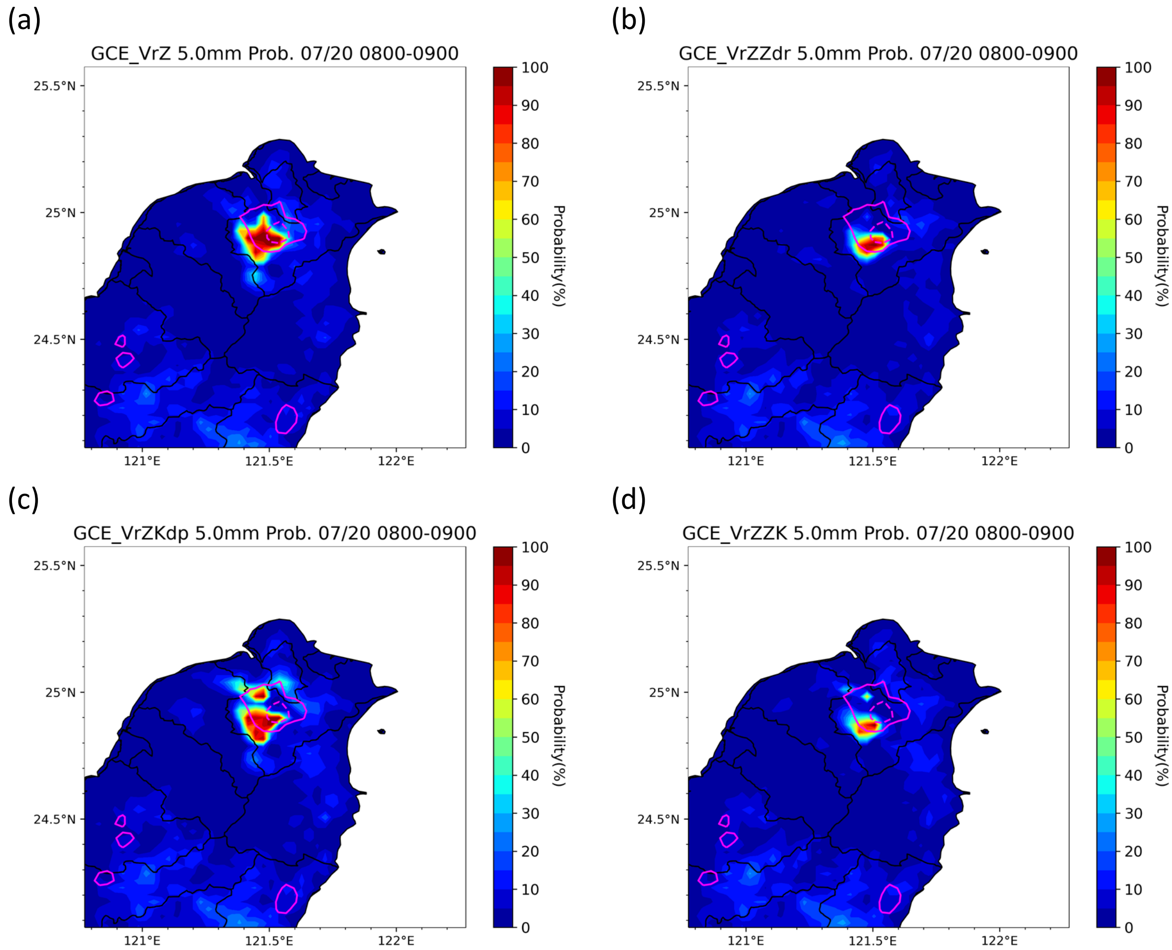

Figure 83 Probability of 1-hour accumulated rainfall exceeding 5 mm in the afternoon thunderstorm experiments with GCE scheme. The solid contour and the dashed contour represent 10-mm and 30-mm contours respectively.

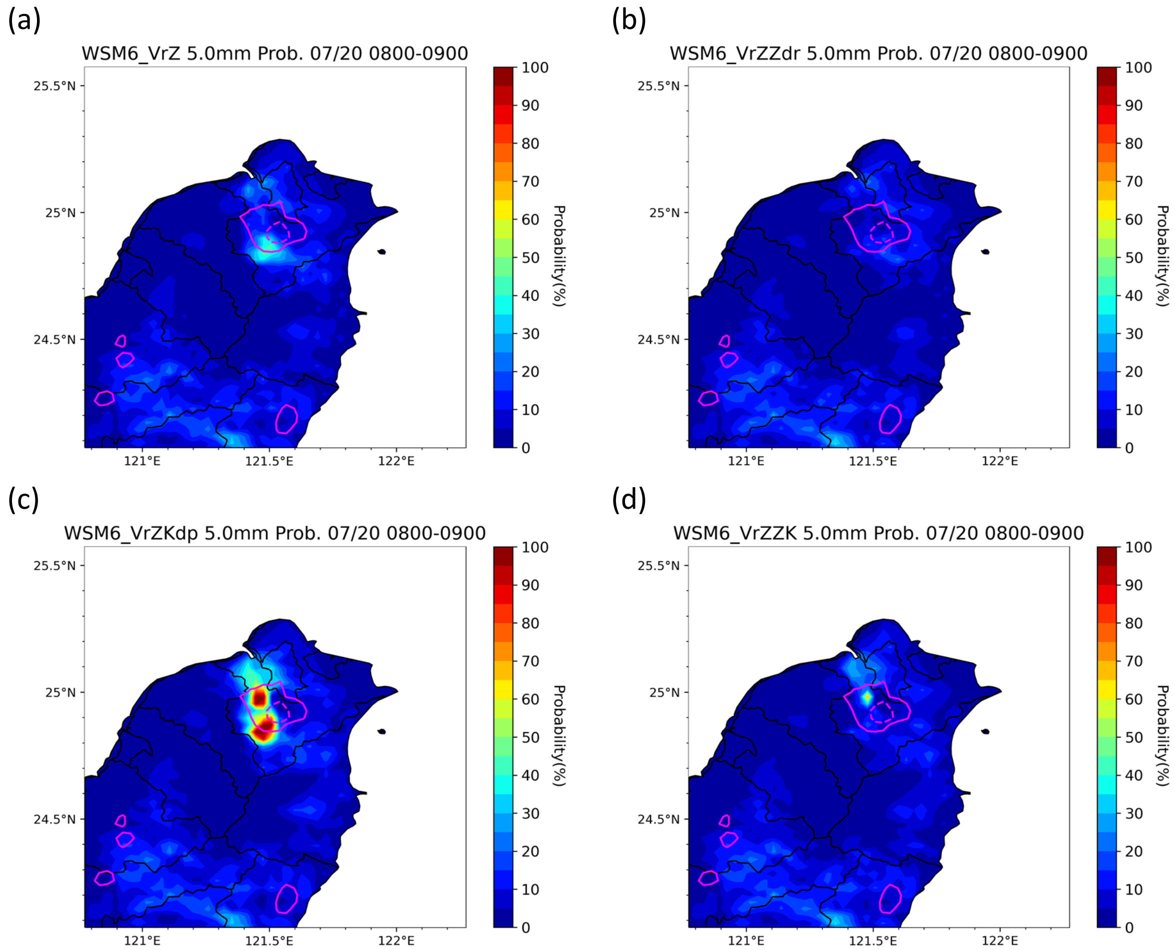

Figure 84 Probability of 1-hour accumulated rainfall exceeding 5 mm in the afternoon thunderstorm experiments with WSM6 scheme. The solid contour and the dashed contour represent 10-mm and 30-mm contours respectively.

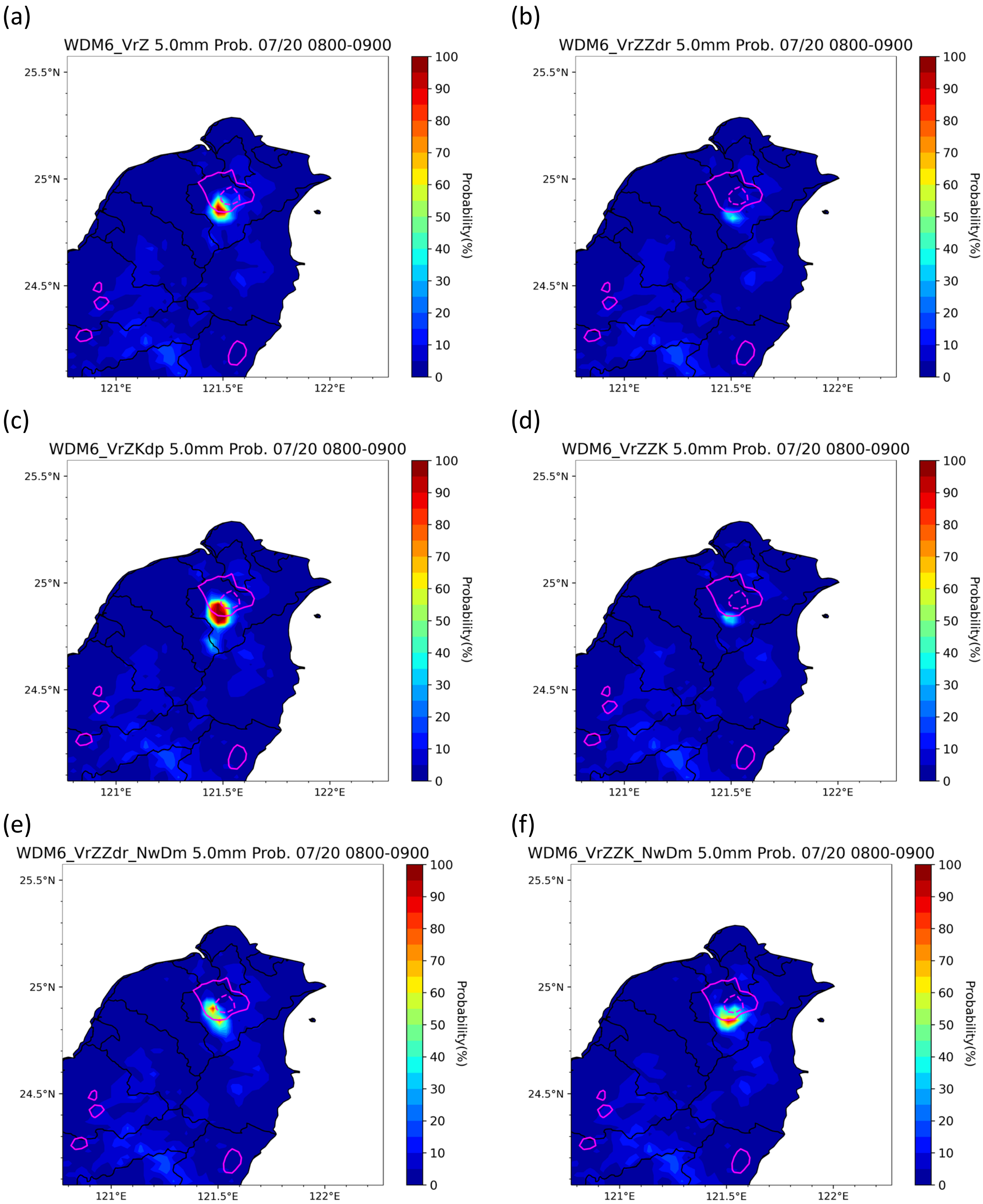

Figure 85 Probability of 1-hour accumulated rainfall exceeding 5 mm in the afternoon thunderstorm experiments with WDM6 scheme. The solid contour and the dashed contour represent 10-mm and 30-mm contours respectively.

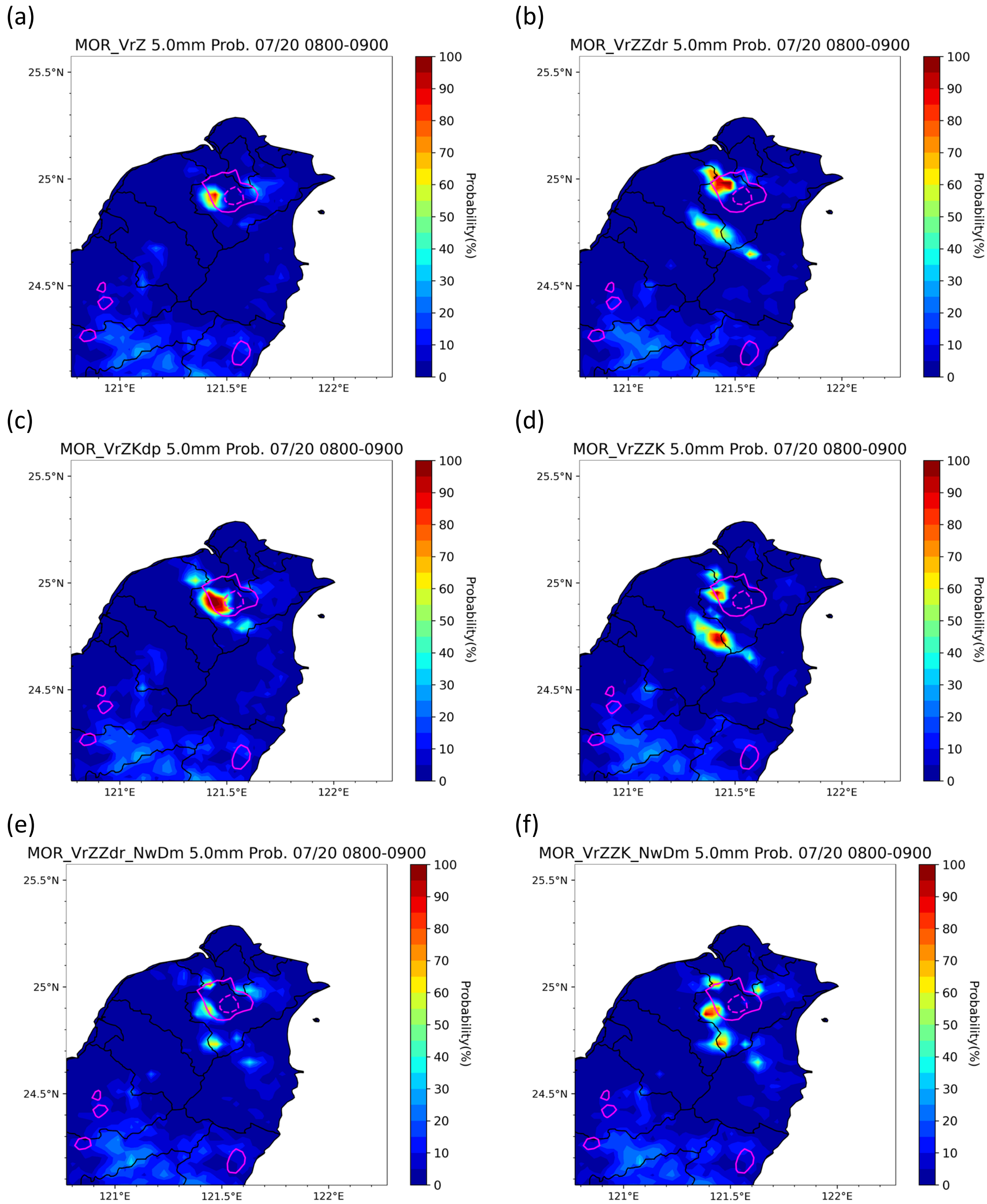

Figure 86 Probability of 1-hour accumulated rainfall exceeding 5 mm in the afternoon thunderstorm experiments with MOR scheme. The solid contour and the dashed contour represent 10-mm and 30-mm contours respectively.